warwick.ac.uk/lib-publications

Library Declaration and Deposit Agreement

1. **STUDENT DETAILS**

    Please complete the following:

    Full name: ...Guannan Li...

    University ID number: ....1063106..

2. **THESIS DEPOSIT**

    2.1   Under your registration at the University, you are required to deposit your thesis with the University in BOTH hard copy and in digital format. The digital copy should normally be saved as a single pdf file.

    2.2   The hard copy will be housed in the University Library. The digital copy will be deposited in the University's Institutional Repository (WRAP). Unless otherwise indicated (see 2.6 below), this will be made immediately openly accessible on the Internet and will be supplied to the British Library to be made available online via its Electronic Theses Online Service (EThOS) service.
    [At present, theses submitted for a Master's degree by Research (MA, MSc, LLM, MS or MMedSci) are not being deposited in WRAP and not being made available via EthOS. This may change in future.]

    2.3   In exceptional circumstances, the Chair of the Board of Graduate Studies may grant permission for an embargo to be placed on public access to the thesis **in excess of two years**. This must be applied for when submitting the thesis for examination (further information is available in the *Guide to Examinations for Higher Degrees by Research*.)

    2.4   If you are depositing a thesis for a Master's degree by Research, the options below only relate to the hard copy thesis.

    2.5   If your thesis contains material protected by third party copyright, you should consult with your department, and if appropriate, deposit an abridged hard and/or digital copy thesis.

    2.6   Please tick one of the following options for the availability of your thesis (guidance is available in the *Guide to Examinations for Higher Degrees by Research)***:**

☐	Both the hard and digital copy thesis can be made publicly available immediately
☐	The hard copy thesis can be made publicly available immediately and the digital copy thesis can be made publicly available after a period of two years (*should you subsequently wish to reduce the embargo period please inform the Library*)
☑	Both the hard and digital copy thesis can be made publicly available after a period of two years (*should you subsequently wish to reduce the embargo period please inform the Library*)
☐	Both the hard copy and digital copy thesis can be made publicly available after _____ (insert time period in excess of two years). **This option requires the prior approval of the Chair of the Board of Graduate Studies (see 2.3 above)**

    The University encourages users of the Library to utilise theses as much as possible, and unless indicated below users will be able to photocopy your thesis.

☐	I **do not** wish for my thesis to be photocopied

3. **GRANTING OF NON-EXCLUSIVE RIGHTS**

    Whether I deposit my Work personally or through an assistant or other agent, I agree to the following:

- Rights granted to the University of Warwick and the British Library and the user of the thesis through this agreement are non-exclusive. I retain all rights in the thesis in its present version or future versions. I agree that the institutional repository administrators and the British Library or their agents may, without changing content, digitise and migrate the thesis to any medium or format for the purpose of future preservation and accessibility.

4. DECLARATIONS

I DECLARE THAT:

- I am the author and owner of the copyright in the thesis and/or I have the authority of the authors and owners of the copyright in the thesis to make this agreement. Reproduction of any part of this thesis for teaching or in academic or other forms of publication is subject to the normal limitations on the use of copyrighted materials and to the proper and full acknowledgement of its source.

- The digital version of the thesis I am supplying is either the same version as the final, hard-bound copy submitted in completion of my degree once any minor corrections have been completed, or is an abridged version (see 2.5 above).

- I have exercised reasonable care to ensure that the thesis is original, and does not to the best of my knowledge break any UK law or other Intellectual Property Right, or contain any confidential material.

- I understand that, through the medium of the Internet, files will be available to automated agents, and may be searched and copied by, for example, text mining and plagiarism detection software.

- At such time that my thesis will be made publically available digitally (see 2.6 above), I grant the University of Warwick and the British Library a licence to make available on the Internet the thesis in digitised format through the Institutional Repository and through the British Library via the EThOS service.

- If my thesis does include any substantial subsidiary material owned by third-party copyright holders, I have sought and obtained permission to include it in any version of my thesis available in digital format and that this permission encompasses the rights that I have granted to the University of Warwick and to the British Library.

5. LEGAL INFRINGEMENTS

I understand that neither the University of Warwick nor the British Library have any obligation to take legal action on behalf of myself, or other rights holders, in the event of infringement of intellectual property rights, breach of contract or of any other right, in the thesis.

Please sign this agreement and ensure it is bound into the final hard bound copy of your thesis, which should be submitted to Student Reception, Senate House.

Student's signature: ....…… Date: ....07/06/2016..............................
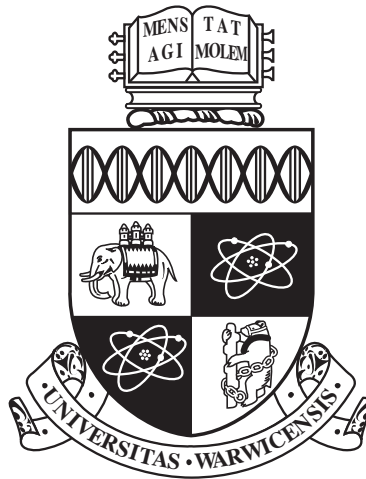
Locality Sensitive Modelling Approach for Object Detection, Tracking and Segmentation in Biomedical Images

by

Guannan Li

Thesis

Submitted to the University of Warwick

for the degree of

Doctor of Philosophy

Department of Computer Science

January 2016

THE UNIVERSITY OF

WARWICK

Contents

i

List of Tables

List of Figures

viii

Acknowledgments

It is my great honour to undertake this PhD which is absolutely an enlightened and enjoyable experience in my life. This wonderful journey can never be accomplished without enduring supports and trusts from all my family, supervisors, collaborators and colleagues.

To my parents I dedicate this thesis in token of unspeakable affection and gratitude. The story of my PhD all began by their unreservedly love and unshakable trust on me. I must heartily appreciate my parents providing enormous financial support for 11 years of my life and study in the United Kingdom, which culminated in the form of this PhD thesis.

I would like to sincerely thank my supervisor Dr Nasir Rajpoot for offering me this opportunity and financial support to participate in scientific research under his patient and careful supervision. He has always been an excellent and warm mentor who grants me firm confidence and research ability in academics over the past few years. I would like also to thank my co-supervisor Dr Victor Sanchez for his dedicated reviewing of my academic writing and inspirations to my research work during all these years.

I am very thankful for all collaborators in my research work, for their efforts, experimental materials and feedbacks. My special thanks to Dr Shahid Khan for his help and feedback in our collaboration.

To my academic advisors, Prof Chang-Tsun Li, Dr Sara Kalvala and Dr Yulia Timofeeva, I am very grateful for their time, involvement, discussions and feedbacks for the annual assessments during my PhD progress. I also appreciate all

Declarations

This thesis is submitted to the University of Warwick in support of my application for the degree of Doctor of Philosophy. I declare that, except where acknowledged, the material contained in the thesis is my own work, and has not been previously published for obtaining an academic degree.

Guannan Li

January 12th, 2016

A List of Publication

Journal Publications

1. Li, G., Sanchez, V., Raza, S. E., and Rajpoot, N. 2016, Novel cell orientation congruence descriptors for epithelium segmentation in endometrial histology images. IEEE Transactions on Medical Imaging (submitted)

2. Li, G., Sanchez, V., Patel, G., Quenby, S. and Rajpoot, N., 2015. Localisation of luminal epithelium edge in digital histopathology images of IHC stained slides of endometrial biopsies. Computerized Medical Imaging and Graphics, 42, pp.56-64.

3. Li, G., Sanchez, V., NAGARAJ, P., Khan, S. and Rajpoot, N., 2015. A novel multitarget tracking algorithm for Myosin VI protein molecules on actin filaments in TIRFM sequences. Journal of Microscopy, 260(3), pp.312-325.

Conferences

1. Li, G., Sanchez, V., Patel, G., Quenby, S. and Rajpoot, N., 2014. Localisation of luminal epithelium edge in digital histopathology images of IHC stained slides of endometrial biopsies. 12th European Congress on Digital Pathology (podium presentation).

2. Li, G. and Rajpoot, N., 2012. Automated Segmentation and tracking of dynamic focal adhesions in time-Lapse fluorescence microscopy. 19th International Conference. ICONIP 2012, Proceedings, Part I, pp.648-655.

Abstract

Biomedical imaging techniques play an important role in visualisation of e.g., biological structures, tissues, diseases and medical conditions in cellular level. The techniques bring us enormous image datasets for studying biological processes, clinical diagnosis and medical analysis. Thanks to recent advances in computer technology and hardware, automatic analysis of biomedical images becomes more feasible and popular. Although computer scientists have made a great effort in developing advanced imaging processing algorithms, many problems regarding object analysis still remain unsolved due to the diversity of biomedical imaging.

In this thesis, we focus on developing object analysis solutions for two entirely different biomedical image types: fluorescence microscopy sequences and endometrial histology images. In fluorescence microscopy, our task is to track massive fluorescent spots with similar appearances and complicated motion pattern in noisy environments over hundreds of frames. In endometrial histology, we are challenged by detecting different types of cells with similar appearance and in terms of colour and morphology. The proposed solutions utilise several novel locality sensitive models which can extract spatial or/and temporal relational features of the objects, i.e., local neighbouring objects exhibiting certain structures or patterns, for overcoming the difficulties of object analysis in fluorescence microscopy and endometrial histology.

Abbreviations

GFP Green Fluorescent Protein

ATP Adenosine triphosphate

TIRFM Total Internal Reflection Fluoresces Microscopy

TIFF Tagged Image File Format

SNR signal-to-noise ratio

IMM Interactive Multiple Model

LAP Linear Assignment Problem

CAT Computer-Aided Tracking

DoG Difference of Gaussian

EM Expectation Maximization

TP True Positive

FP False Positive

FN False Negative

OSPA Optimal Sub-Pattern Assignment

MSE Mean Squared Error

MSD Mean Square Displacement

NN	Nearest-Neighbour
UNK	Uterine Natural Killer
H&DAB	Haematoxylin & Diaminobenzidine
LIPSyM	Local Isotropic Phase Symmetry Measure
UHCW	University Hospitals Coventry and Warwickshire
HPFs	High Power Fields
COrCo	Cell Orientation Congruence
MR-COrCo	Multi-Ring Cell Orientation Congruence
LBCOrCo	Local Binary Cell Orientation Congruence
MR-LBCOrCo	Multi-Ring Local Binary Cell Orientation Congruence
CNNs	Convolutional Neural Networks

Chapter 1

Introduction

Biomedical imaging offers a new approach to study and understand biological processes, as well as to measure and diagnose medical illnesses and conditions, by visually revealing internal behaviours, structures and properties of biological substances, organs and tissues. However, biomedical imaging can produce extensive datasets in which one single image also contain enormous information, e.g., monitoring the interaction of massive sub-cellular structures from long image sequences, and analysing abnormalities of enormous cells and tissue regions from thousands of digital pathology images. Therefore, manual processing and analysing of biomedical images is normally infeasible, as that would result in laboriousness, unrepeatability and inefficiency. Moreover, bias and inaccuracy are often caused by subjective assessment in manual work. Today the computer-aided techniques start playing a more and more important role in the large-scale processing and analysis of biomedical images.

In general, biomedical image has a wide diversity of types due to different experiment purposes, biopsies, imaging equipments, or even imaging parameters, which leads to the impossibility of developing generic solution for processing and analysing all types of biomedical images. Nonetheless, some of the common tasks in processing biomedical images usually involve object analysis, i.e., detection, segmen-

tation or tracking of certain objects, e.g., protein spots, cells or glands, depending on the nature of images. Biomedical image processing is not trivial due to the complexities of the objects and image quality, in most cases, conventional image processing methods, e.g., Otsu thresholding, watershed segmentation, regional maxima, and mathematical morphology, are often incorporated with more advanced techniques, e.g., statistical inference, computer vision, pattern recognition, and machine learning.

For instance, a protein spot is first detected by local maxima (a spot is treated as a set of connected neighbouring pixels which exhibits the maxima intensity in a local region) in fluorescence microscopy image sequence, and it is then tracked across the frames in two steps: (1) predicting its position by statistical inference method on the next frame, and (2) updating its new position by associating it to a corresponding spot which has the shortest distance to its predicted position on the next frame. However, it is challenge to accurately associate spots between adjacent frames based on comparing spot features such as position, shape or intensities, because the spots are normally textureless and all in circular shape, and also such spot features are highly inconsistent even over a short sequence of frames due to imaging equality.

Another example of the application area is when the clinical diagnosis of a medical condition is made on counting stromal cells in a tissue region. It is difficult to distinguish between stromal cell and epithelial cells because they have very similar features in terms of texture and stain colour between them, and also the features such as size and morphological shape are highly inconsistent between the same type of cells. However, one can observe that stromal cells are distant to glands and normally exhibits an inconsistent orientation pattern in a local neighbourhood. In contrast, epithelial cells are packed along the lumen edge and are arranged in parallel. The example of stromal and epithelial will be shown in the later chapters. Therefore, the classification of epithelial cells can be achieved by examining

2

cell orientation consistency in local neighbourhood. It is obvious that modelling temporal and spatial relationships between the objects in local neighbourhood can offers more crucial advantages, comparing with exclusively employing their inherent features (e.g., shape, texture and colour) for object analysis. We express such relational features by numerically (or statically) computing the similarities or differences between the objects (e.g., fluorescent spots or cells) in a temporal or/and spatial local neighbourhood, such attempt is so called as locality sensitive modelling approach.

In this thesis, we propose several image analysis algorithms by utilising the fact that local neighbouring objects exhibiting certain structures or patterns, to obtain their relational features computed by locality sensitive modelling approach, for overcoming several difficulties of object analysis in two different projects. The first one regards to track the movement of a motor protein in fluorescence images for understating their roles in intracellular processes. The second one aims at developing a computer-aided system which can automatically counts cells in digital endometrial biopsy images for assisting diagnosis of recurrent miscarriages due to the over-presence of natural killer cells.

1.1 Object Analysis in Fluorescence Bioimages: Myosin VI Protein Movement on Actin Filaments

Green Fluorescent Protein (GFP) [2] [3] was first isolated from the jellyfish *Aequorea victoria* in the early 1960s. It can emit bright green fluorescence when exposed to light in the blue to ultraviolet range, which causes it to be used as genetically encoded probes. Jellyfish-derived GFP and its homologs extracted from diverse marine animals have since been widely engineered into many mutants with enhanced characteristics and availability in entire visible spectrum over the past few decades. The discovery of GFPs and their usages [4] [5] [6] in the latest microscopy technologies

have resulted in many possibilities for direct visualising of cellular structures and a large number of intracellular activities such as protein interaction and traffick in living cells, which provide scientists substantial biological information regarding to the physical properties of fluorescent proteins, i.e., extinction coefficients, quantum yields and photobleaching rates, for answering many biological questions in sub-cellular level.

Myosins consist of a family of Adenosine triphosphate (ATP) dependent motor proteins in eukaryotes, that convert chemical energy in the form of ATP to mechanical energy to generate force and movement for Actin-based motility. They are well known for their involvements in muscle contraction [7] [8] and role in a wide range of cell motility processes [9]. Myosin VI protein is a processive motor [10] that attaches to the surface of a suitable substrate, called Actin filament, and uses it as a rail to carry out the movement. This particular protein shows a very interesting phenomenon that it travels towards the minus end of an Actin filament, in an opposite direction as compared to other proteins in the Myosin family [11]. Investigating the movements of Myosin VI proteins on Actin filaments may assist in answering many questions regarding their functions and motor properties in a variety of intracellular processes such as vesicular membrane traffic, cell migration and mitosis [12]. Nonetheless, manually tracking and recording the movements of thousands of fluorescent protein spots over several hundreds of image frames is not a feasible option, as it suffers from unrepeatability, inefficiency, and inaccuracy due to subjective assessment. Therefore, a computer-aided multi-target tracking system is eagerly requested by cell biologists for analysing the spatio-temporal movement of Myosin VI proteins.

A conventional tracking framework for fluorescent spots is comprised of several steps. First, the image sequences are usually very noisy due to background fluorescence and electronic noise of microscopy. Since the image quality has an significant impact on spot detection accuracy, a preprocessing step that involves

4

reduction/removal of background noise and enhancement of the visual appearances of fluorescent spots, is necessary for improving the signal-to-noise ratio (SNR) of images, which can be accomplished by many denoising techniques [13]. Second, fluorescent spots are detected from each image frame for the later tracking step, the detection is usually based on the assumption of that visual appearance of fluorescent spot exhibits as a regional maxima in a small local image region in terms of intensity or a response of an imaging system to a point source that described by diffraction-limited point spread function (PSF) [14]. The last step is to track fluorescent spots across all image frames. The spot tracking is essentially a data association process that iteratively associates target in one frame with their correspondences appeared in an adjacent (previous or next) frame, which eventually establishes the target trajectories over a fragment of consecutive frames. Data association methods are generally categorised into local and global association. The strategy of local data association is to individually associate an established target track up to one frame with a most probable target among all potential targets within the local neighbour-hood (also called acceptance gate) around the location of current track in successive frames. Nearest Neighbour filtering [15], Multiple Hypothesis Tracker [16] [17] [18] and Joint Probabilistic Data Association filter [19] [20] [21] [22] are well known local data association based tracking methods. On the contrary, global data association, e.g., [23] and Linear Assignment Problem based methods [24] [25] [26] [27] simultaneously associate all the targets in one frame with their correspondences in an adjacent frame, by finding a globally minimum matching cost (e.g., Euclidean distance between two spots).

Spot tracks generated by data association suffer from inaccuracy due to noisy background and spot measurement/detection errors. Bayesian filtering based methods, e.g., Kalman filter [28], Extended Kalman filter [29], Unscented Kalman filter [30] and Particle filter [31], are often employed as estimators which recursively predict spot states (e.g., location, velocity or acceleration) based on the previous spot

states and the new spot measurements to smooth and improve spot tracks produced by data association methods. Kalman filter is only appropriate when the targets have linear motion models. Non-linear Bayesian filters such as Extended Kalman filter, Unscented Kalman filter and Particle filter are designated to handle the non-linearity of some spot motions (e.g., Brownian motion). Extended Kalman filter attempts to linearise the non-linear motion model but suffers from divergence caused by poor linearisation. Unscented Kalman filter and Particle filter use a set of Monte Carlo sampled points/particles (potential spot states) to represent a posterior probability distribution of the spot states. However, they are computationally intensive in dense and clutter environments such as hundreds of fluorescent proteins. Interactive Multiple Model (IMM) filtering [32], on the other hand, provides a computationally effective alternative for approximating non-linear spot motions by running multiple Kalman filters in parallel, where each Kalman filter features a distinct motion model respectively.

1.2 Object Analysis in Histology Images: Automatic Analysis of Endometrial Biopsy Images for the Diagnosis of Recurrent Miscarriages

Digital pathology offers several advantages over the age-old tissue slide analysis under the microscope by converting tissue slides into high-resolution microscopic image of the whole slide. One of these advantages is the seamless transfer and manipulation of digitised images via computer algorithms [33]. Indeed, histology image analysis has been tipped to hold the key to providing the much needed added value to digital pathology [34].

Uterine Natural Killer (UNK) cells are immune cells found in the human female uterus lining. In general, these cells make up no more than 5% of all cells in the womb lining. Recently, the authors of [35] showed that there are abnormally high

numbers of UNK cells in the uterus of women who suffer from recurrent miscarriages, a condition that affects one in every 100 women of reproductive age in the UK. High UNK cell density in the lining of the womb was associated with glucocorticoid deficiency [36] and a small randomised controlled trial suggested that women with high numbers of UNK cells are more likely to have a live birth if given glucocorticoids in lieu of placebo [37]. This means that UNK testing has clinical significance as it could direct clinicians towards the effective treatment. A diagnose protocol for the recurrent miscarriages due to the over-presence of UNK cells devised in [35] calculates the ratio of UNK cells to stromal cells in digital images of endometrial tissue slides.

Manual counting of thousands of cells from a large digital endometrial histology image dataset on a regular basis is cost ineffective, potentially inaccurate due to subjective assessment, and involves the hassle of manually removing epithelium from tissue regions. The automatic cell counting system involves several image processing steps, i.e., detecting all types of cells, segmenting brown stain regions and epithelium for cell classification, and classifying stromal, epithelial and UK cells, which is continuously performed on the HPF images from the same whole slide image until a number (5,000 at minimum in our experiments) of stromal cells are cumulatively counted. Next, the ratio of UNK cells to stromal cells is calculated and converted into a percentage for the diagnosis.

UNK cells are those cells covered by brown stain regions, which are illustrated in Figures 1.1(a) and (b), brown stain regions can be used for classifying UNK cells. Counting stromal and UNK cells is the primary task here and the analysis of cell morphology in endometrial biopsies (i.e., colour texture, morphological shape, or mitosis) is beyond the scope of the diagnose protocol, therefore segmentation of stromal and UNK cells is not necessary to accomplish the cell counting. Nonetheless, it is compulsory to segment brown stain region for classify UNK cells from the counts.

It is worth noting that separately detecting stromal and epithelial cells is

difficult due to their exhibiting similar stain colour and texture in a variety of morphological shapes, as shown in Figures 1.1(a) and (b). However, epithelial cells are packed at the boundaries of tissue regions and lumen, therefore this prior knowledge can help us to locate potential epithelial cells from the detected cells. More importantly, it is observed that epithelial cells in local neighbourhood have distinct distribution/arrangement and orientation congruency along some particular directions, compared with that of local neighbouring stromal cells. This observation gives us a clue for distinguishing between epithelial and stromal cells, although these two types of cells are exhibiting the same intrinsic features.

1.3 Aims of the Thesis

The objects in microscopy sequences and endometrial histology images often exhibit inconsistent features compared with the other objects of the same type or similar features to the objects of other types. Existing object analysis algorithms in biomedical image have weaknesses and unsatisfactory performance for analysing these objects, because these methods are limited in modelling intrinsic characteristics of the objects. In this thesis, we aim to expand the capabilities of object analysis in both TIRFM sequences of Myosin VI proteins and Endometrial Histology Images, by a locality sensitive modelling approach derived from the concept of that the prominent features of an object may embody in a temporal or spatial correlation between it and others in a local neighbourhood.

1.3.1 Detection and Tracking of Myosin VI Protein Spots in TIRFM Sequences

Existing spot tracking algorithms are proprietary for the specific types of fluorescent spots and microscopy sequences. Consequently, they are not adept in detecting and tracking Myosin VI spots in TIRFM sequences due to the particular visual appear-
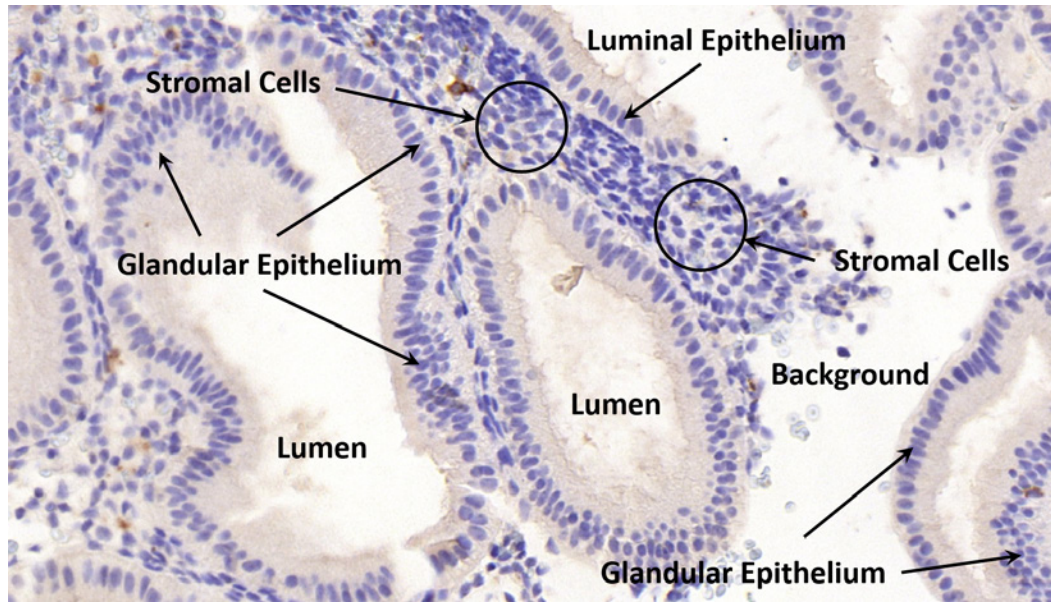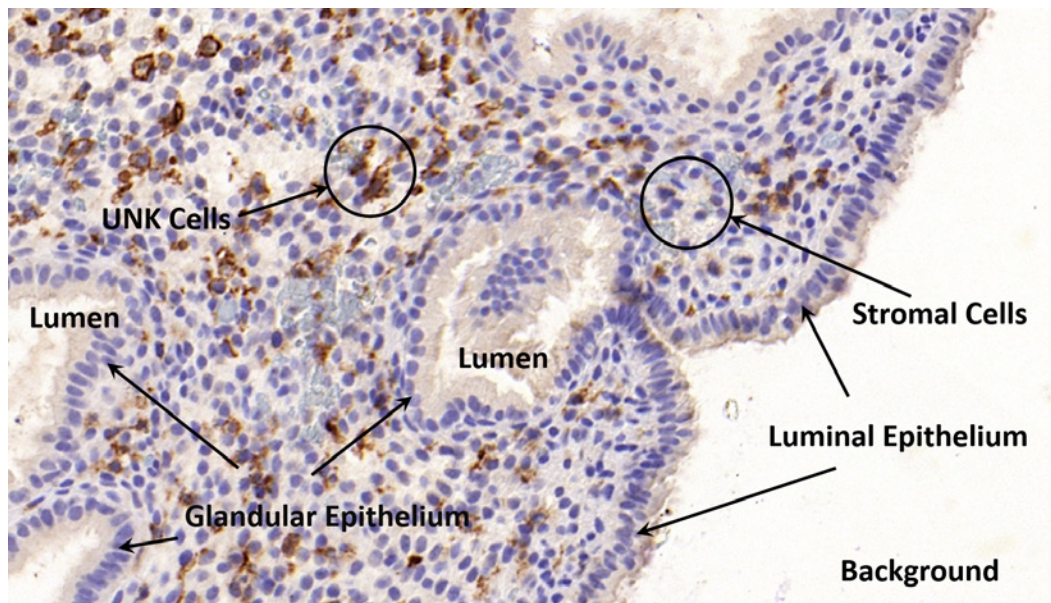
Figure 1.1: (a) and (b) are two example images captured for identified regions in the HPFs of whole slide images at 40× magnification.

ances and non-linear motions of the spots and noisy backgrounds such as fluorescent artefacts and subcellular objects. Moreover, these algorithms are computational expensive and inaccurate when they are faced with intensive number of spots with frequent overlapping, disappearing, reappearing, and abrupt changes of directions and velocities. Our aim is to develop a low computational cost multi-target tracking framework to cope with the complex characteristics of Myosin VI spots and overcomes the difficulties in their detection and tracking in TIRFM sequence.

1.3.2 Cell Detecion and Epithelium Segmentation in Endometrial Histology Images

The computer-aided diagnostic system for recurrent miscarriages due to over-presence of UNK cells is developed in two stages. The first stage aims to detect cells, classify between stromal and UNK cells, and localise luminal epithelium in order to excluded epithelial cells. It is important to note that the image data in the first stage was captured near the boundary of tissue regions and gland are not included according to the diagnosis protocol of the first stage. Hence, the scope in this stage is to remove only the cells which are located within a range of $200\mu m$ to luminal epithelium from the cell counts.

To the best of our knowledge, there is no existing method proposed for segmenting both luminal and glandular epithelium in endometrial histology image. Alternatively, the epithelium can be indirectly obtained by extracting it from segmented glandular structures. Existing gland segmentation methods are mainly based on the assumption that a glandular structure is in the form of lumen surrounded by a layer of epithelial cells. And they tend to detect, segment or classify lumen and epithelial cells by employing their locations, colour and texture. In endometrial histology, there are insignificant distinctive features, in terms of colour, texture and morphology, between epithelial and stromal cells, and also between lumen and background regions. Moreover, epithelium may consist of more than one

layers of epithelial cells, and stromal cells are also packed at the boundaries of glands and tissue regions in some cases. Consequently, these methods fail to segment epithelium correctly. In the second stage, the ultimate goal is to develop a universal solution for segmenting both luminal and glandular epithelium in order to excluded epithelial cells..

1.4 Main Contributions

The novelty of our framework for tracking Myosin VI proteins in TIRFM is manifold and listed as follows:

- First, it uses a Bayesian estimation filter with two motion models to accurately approximate the non-linear movements of Myosin VI proteins.

- Second, it integrates a global data association into the Bayesian estimation filtering process for solving measurement-to-target and estimation-to-target assignment problems.

- Third, it overcomes the limitation of bijective mapping of global data association by incorporating a locality sensitive model with imaginary spots in the spot association process.

Several novel methods are contributed for detecting and classify different types of the cells, and also for segmenting both luminal and glandular epithelium in endometrial histology images:

- A cell detection method based on local phase symmetry is enhanced by a novel locality sensitive model for improving cell dtetcion accuracy, and a novel adaptive background removal method is proposed to segment brown stain regions (when stain UNK cell using DAB) which are used identify UNK cells.

- We identify individual tissue region by using a clustering algorithm on the detected cell and propose a novel approach to identify the cells packed at the

boundaries of tissue regions as epithelial cells. A curve fitting method is then used on the identified epithelial cells to mark luminal epithelium.

- We propose a generic solution for segmenting both luminal and glandular epithelium. It is observed that epithelial cells are arranged in a locally and neatly oriented manner therefore neighbouring epithelial cells exhibit certain patterns of orientation congruence. Based on the observation, we propose a variety of novel cell orientation congruence descriptors for epithelium segmentation. The common idea of the proposed descriptors is to describe cell orientation congruence within a local cell neighbourhood using locality sensitive modelling approach.

1.5 Thesis Layout

This thesis is divided into 6 chapters. An introduction of biomedical imaging was given in Chapter 1, followed by a brief discussion of challenges and solutions for computerised objects analysis in biomedical imaging. The following chapters 2, 3, 4 and 5 present the solutions based on locality sensitive modelling. Each chapter also briefly reviews the related work and evaluates the proposed solution against the state-of-the-art methods.

Chapter 2 presents the pre-processing methods for removing background noise and enhancing spot appearance to improve spot detection accuracy, and also a method for detecting Myosin protein spots. Next, a multi-target spot tracking framework for is presented in Chapter 3.

Chapter 4 presents a complete cell detection solution for the endometrial histology images containing only luminal epithelium. The solution consists of a cell detection method, a DAB stain segmentation method for classifying UNK cells, and a luminal epithelium localisation methods for excluding irrelevant cells from the cell counts. In Chapter 5, we propose a variety of novel cell orientation congruence

descriptors to classify epithelial cells, which can be integrated with superpixel to attain a generic approach for segmenting both luminal and glandular epithelium.

Chapter 6 concludes the thesis, summarises contributions, advantages and limitations of the work, and discusses several future directions for extending the proposed methods.

Chapter 2

Detection of Myosin VI Protein Spots in Fluorescence Microscopy Sequences

The major steps for tracking spot in fluorescence microscopy sequences has been introduced in Chapter 1, which involves 3 main stages: pre-processing, spot detection, and spot tracking. Figure 2.1 shows a workflow of the proposed multi-target tracking framework for Myosin VI protein spots in fluorescence sequence and the intermediate results of each stage. In this chapter, we focus on presenting the pre-processing and spot detection stages, the spot tracking stage will be introduced in Chapter 3.

The reminder of this chapter is organised as follows. Section 2.1 introduces all details necessary to recreate the experiments of detecting and tracking Myosin VI protein spot in fluorescence microscopy sequences. In Section 2.2, we briefly discuss several popular algorithms for detecting fluorescence spots. A pre-processing method for fluorescence microscopy sequences is introduced in Section 2.3 and an algorithm for detecting Myosin VI spots is presented in Section 2.4. We also present a method
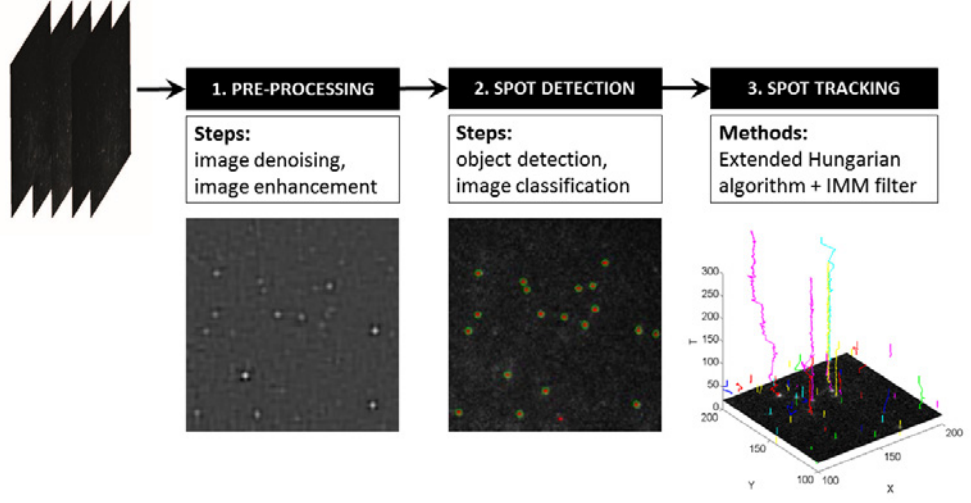
Figure 2.1: The block diagram of the proposed multi-target tracking framework for Myosin VI spots in TIRFM sequence.

of generating synthetic fluorescence sequences for evaluating the proposed detection and tracking algorithms in Section 2.5. In Section 2.6, we evaluate the proposed detection algorithm on both real and synthetic fluorescence microscopy sequences. The work is summarized in Section 2.7.

2.1 Methodology

To study in-vitro properties of Myosin VI proteins, our collaborators artificially introduce plasmid into transfected mammalian cells to produce the engineered Myosin VI protein with a fluorescent tag. Once the proteins start being produced by the cells, our collaborators harvest the cell to extract and purify the proteins which are used to do the in-vitro motility stepping assays to analyse the properties of a single molecule [38] [39]. Myosin VI proteins on Rhodamine-Phalloidin stabilised Actin filaments are dyed by enhanced GFP [40] and their spatial-temporal movements are captured using Total Internal Reflection Fluorescence Microscopy (TIRFM) [41] [42] into in-vitro digital image sequences. TIRFM technique is equipped with the abili-

15

ties of limiting Myosin VI protein excitation in a narrow spectrum region and eliminating background fluorescence. These particular advantages significantly improve signal-to-noise ratios and the spatial resolution of fluorescent proteins to enhance their visual presences in in-vitro image sequences, thereby easing object analysis in fluorescence bioimage such as detection and tracking of Myosin VI proteins to a certain extent [42].

The fluorescence microscopy assay for Myosin VI proteins were performed using an Axioskop 40 Microscope (Zeiss, Germany) shown in Figure 2.2(a), fluorescence microscope with a PlanNeofluar 100×1.45 numerical aperture objective fitted with a custom laser excitation system consisting of a frequency doubled neodymium: that entered the fluorescence light path using a custom-built adaptor. Fluorescence emitted from the rhodamine-phalloidin-labeled actin filaments or the eGFP labelled Myosin VI complexes was collected by the same objective lens. Filter cubes, mounted in the microscopes epifluorescence filter wheel, separated the eGFP fluorescence (Excite 488nm Laser, dichroic: Di02-R488; Emission filter: FF02-520/28, Semrock, Rochester, NY, USA) from the rhodamine fluorescence (yttrium aluminum garnet laser ($\lambda = 532$nm, 20 milliwatts), dichroic: Di02-R561; Emission filter: FF01-609/54 Semrock), the fluorescence was imaged onto a charge coupled device camera. More details on microscopy workstation can be found in [43]. The issues of static errors due to ambient vibrations was dealt with in [44]. They analysed static eGFP spots which were immobilized to a glass coverslip and showed that mobile single fluorophores could be detected reliably.

Furthermore, the setup used in our experiments is similar to the one used in [44] where a shutter-less camera was used to acquire the images. Image sequences of video were captured using a frame grabber card and recorded onto a computer hard disc in Tagged Image File Format (TIFF). The time interval between two adjacent frames of the TIRFM sequences is 0.048s. The resolution of a frame is 53.12μm$\times49.28\mu$m (332×308 pixels, 6.25 pixel/μm). Imaging process of Myosin VI

proteins using two-channel TIRFM is shown in Figure 2.2(b). Myosin VI proteins and Actin Filaments are imaged in the Green and Red channel respectively. A sample frame from a two-channel TIRFM sequence is shown in Figure 2.3(a). The Green and Red channels separated from the sample frame are shown in Figures 2.3(b) and (c), respectively. In addition, Figure 2.3(d) shows a sample frame from an one-channel TIRFM sequence of Myosin VI proteins.

2.2 Related Work

It is a great challenge of obtaining accurate and complete detection of subcellular structures in fluorescence microscopy images [45]. The quality of fluorescence microscopy image is typically poor due to many limitations in the image acquisition process. It is especially the case for imaging living cell, where the images normally have a very low SNR, this is because that the illumination is reduced to the minimum in order to prevent photo-damage and photo-bleaching [46] [47]. In addition, although optical microscopy technique has been greatly improved over the last decade [48], the resolution of the best microscope available today is only approximately 100 nanometers, which is still comparatively coarse to the sizes of subcellular structures (generally only several nanometers in diameter). This causes that a subcellular structure labelled with GFPs exhibits as a bright spot which has diffraction-limited appearance and only occupy a few pixels in the images. Moreover, the appearances of subcellular structures are similar to that of e.g., fluorescent artefacts, other irrelevant background structures, or even the background noise due to electronics. Therefore it is very difficult even for expert biologists to precisely recognise subcellular structures in fluorescence microscopy images.

Spot detection methods are generally divided into two groups: unsupervised and supervised. Unsupervised methods implicitly or explicitly model the appearances of spots and images. The parameters of the appearance model must be

(a)
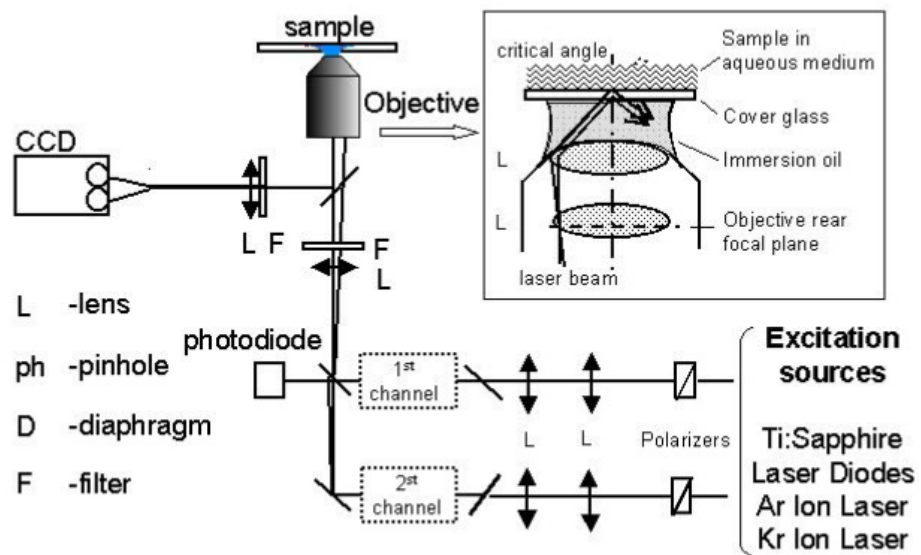
(b)

Figure 2.2: (a) A Zeiss Axioskop 40 Microscope; (b) Imaging process of Myosin VI proteins using two-channel TIRFM.
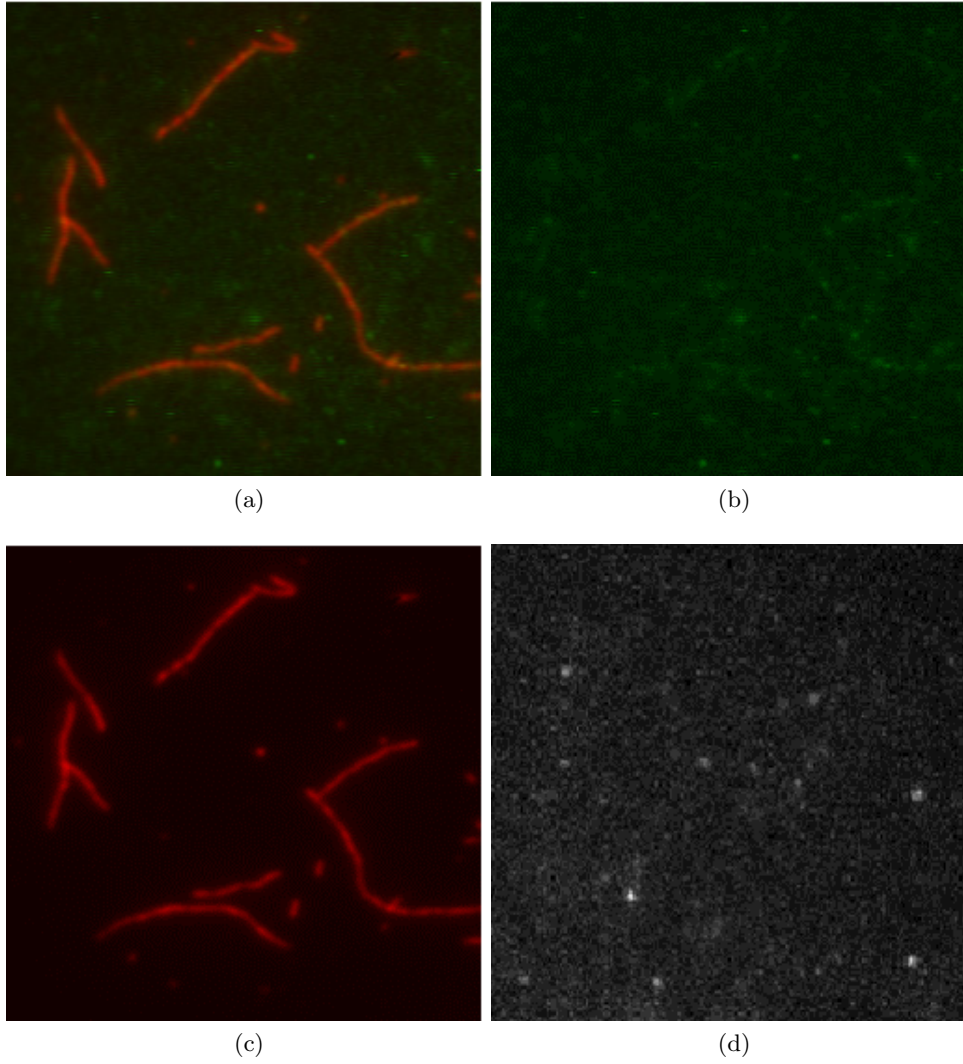
Figure 2.3: (a) is one sample frame from a two-channel TIRFM sequence of Myosin VI proteins, (b) and (c) are the Green and Red channels of (a) respectively, and (d) is a sample frame from a single-channel TIRFM sequence of Myosin VI proteins.

tuned either manually or semi-automatically to proper values based on the assumption/observation of specific images in order to achieve the best performance. Thus, the performance of unsupervised methods depends on the nature of specific images. Most of unsupervised methods can be employed in both pre-processing (e.g., image denoise and spot enhancement) and detecting spot, e.g., wavelet-based multi-scale detectors [49] [50] [51], local background subtraction [52], linear filtering [53] [54] [55], and morphological filtering [56] [57] [58] [59]. The proposed spot detection method is a mixture of several methods listed above.

Supervised methods [60] attempt to "learn" the appearances of spots and irrelevant objects from small image patches containing their intensity profiles and use a classifier, e.g., Adaboost [61] [62] to distinguish between spots and background objects based on "the learned appearances". Supervised methods are more powerful than unsupervised methods when sufficient and accurate "learning materials" are provided [63]. Unfortunately, supervised methods are not suitable in our case since limited number of image dataset were provided to the experiments. A comprehensive comparison between a number of state-of-the-art unsupervised and supervised methods is presented in [63].

2.3   Pre-processing

The pre-processing stage is aimed at facilitating the later spot detection stage by improving the quality (SNR) of image frames via denoising the noisy background and enhancing the visual appearances of spots in TIRFM sequence. We first denoise the TIRFM sequences by using the translational invariant 3D wavelet transform proposed in [64] on the entire sequence. This wavelet based approach is effective in removing the noisy background and aberrant "spot-like" noise while significantly reducing the Gibbs phenomenon that is commonly observed when using wavelet shrinkage for image sequence denoising. Next, we use the Kalman filter [28] and the

Difference of Gaussian (DoG) filter on a frame-by-frame basis in order to enhance the visibility of any potential spot. Here, the Kalman filter adjusts the pixel intensities of frame t based on the pixel intensities of frame $t - 1$, where t denotes the frame index in *time*. The DoG filter is utilised to sharpen spot appearances, as well as remove undesirable artefacts and noises. The intermediate result of each step of the pre-precessing stage performed on real TIRFM frame is shown in Figure 2.4.

2.4 Spot Detection

The spot detection stage consists of two steps: 1) object detection and 2) spot classification.

2.4.1 Object Detection

In the first step, we apply the H-dome transform [65] on each frame. This particular image transformation can detect all regional maxima (bright objects) that resemble "dome-like" structures, e.g., the diffraction-limited spots due to the GFP bound to the Myosin VI protein molecules in our cases.

2.4.2 Spot Classification

In the second step, we propose a spot detection method inspired by the work introduced in [63] to distinguish between potential diffraction-limited spots and other "dome-like" structures. We first normalise the H-dome transformed image I_H into a 2D probability distribution map M_p as follow,

$$M_p(x, y) = \frac{I_H(x, y)}{max(I_H)} \tag{2.1}$$

where $I_H(x, y)$ and $M_p(x, y)$ denote the intensity and probability values at pixel (x, y) of I_H and M_p, respectively, and $max(I_H)$ is the maximum intensity value of I_H.

21

(a)   (b)

(c)
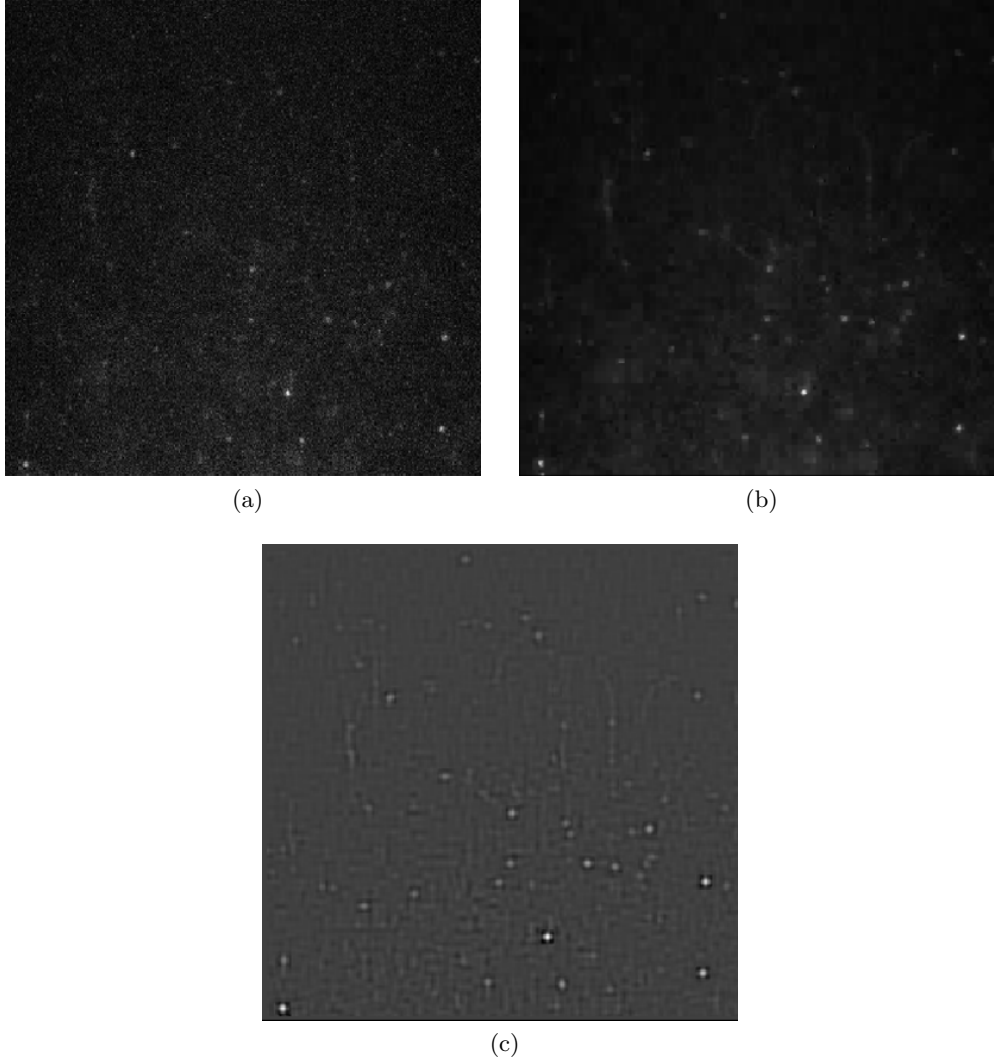
Figure 2.4: The intermediate result of each step in the pre-precessing stage performed on real TIRFM frame. (a) Original frame. (b) Denoised frame after translational invariant 3D wavelet transform and Kalman filtering. (c) DoG filtered frame.

Second, we draw a large number of sample points from the I_H using the probability map M_p. Since the probability values of "dome-like" structures are much higher than that of the background, sample point clusters are usually found in those pixel regions depicting "dome-like" structures. The sample point are clustered using the Mean-shift algorithm [66].

Finally, we fit a 2D Gaussian model to each detected cluster R_{dome}, using an Expectation Maximization (EM) algorithm. The EM algorithm finds the maximum likelihood estimates of the parameters of the fitted 2D Gaussian model, i.e., mean position μ_{dome}, covariance matrix Σ_{dome}, and standard deviations σ_x and σ_y in the x and y directions. We observe that a "dome-like" structure depicts a diffraction-limited spot as long as the estimated 2D Gaussian model for the corresponding cluster satisfies the following criteria: 1) μ is found close to the centroid of R_{dome}; 2) $\sigma_x \leq 1$ and $\sigma_y \leq 1$; 3) the off-diagonal values in Σ_{dome} are close to zero; and 4) $min(\sigma_x^2, \sigma_y^2)/max(\sigma_x^2, \sigma_y^2) \geq 0.6$, in other words, R_{dome} should resemble a more circular shape rather than an elliptical shape. In addition, the size of R_{dome} should be within a threshold according to the magnification used to acquire the TIRFM sequences. For our TIRFM dataset, this size should be no larger than 5×5 pixel. Figure 2.5 shows the intermediate result of each step in the spot detection stage on real TIRFM frame.

The diffraction-limited spots detected using the proposed detection algorithm may still contain those noisy spots caused by, e.g., electronic or auto-fluorescence noise. The true diffraction-limited spots usually retain their intensity level over time until they photo-bleach in a single step fashion or dissociate. In contrast, the noisy spots due to electronic noise usually persist for up to 2-3 frames only, while the intensity values of the noisy spots due to cellular auto-fluorescence noise, which comprise multiple dim fluorophores in most of the cases, decay exponentially with time. Therefore, we can also remove some noisy spots based on the above prior within the tracking stage in a straightforward manner.

(a)   (b)

(c)
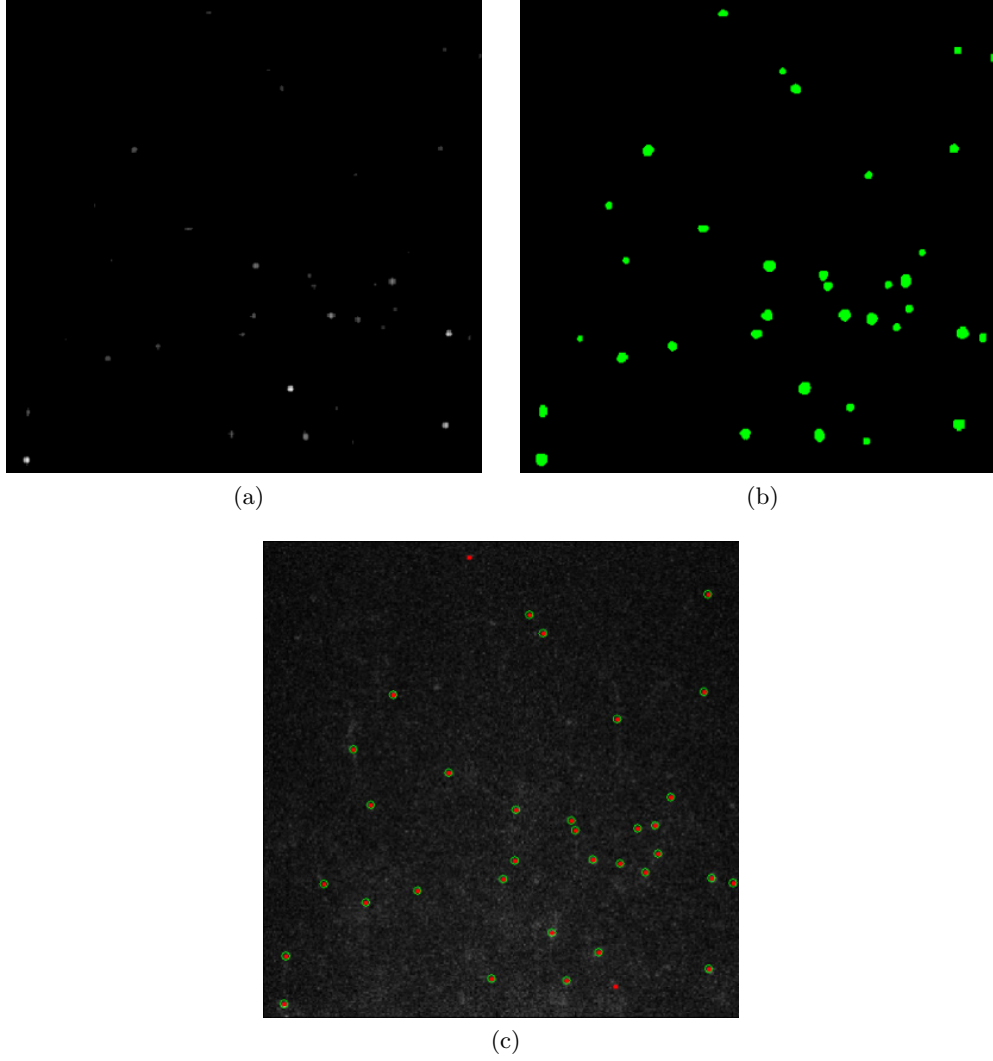
Figure 2.5: The intermediate result of each step in the pre-precessing stage on real TIRFM frame. (a) H-dome transformed frame. (b) Samples drawn from dome-like structures are depicted in green. (c) Final detection results: all "dome-like" structures are depicted in red and only true spots are circled in green.

2.5 Generation of Synthetic TIRFM Sequences

We generate one-channel (gray-scale) synthetic TIRFM sequences of Myosin VI spots moving along Actin filaments in 3 steps: 1) modelling synthetic Myosin VI spots, 2) generating synthetic Actin filaments, and 3) adding artificial noises to the background.

2.5.1 Modelling of Synthetic Spots

We assume that the visual appearances of Myosin VI spots exhibit as 2D Gaussian distribution. The intensity value $S(x, y)$ of the synthetic spot at pixel (x, y) is computed as,

$$S(x,y) = f \cdot e^{-(X'+Y')} \tag{2.2}$$

where

$$X' = \frac{(x - x_o)\cos\theta_s - (y - y_o)\sin\theta_s}{\sigma_x'^2},$$

$$Y' = \frac{(x - x_o)\sin\theta_s + (y - y_o)\cos\theta_s}{\sigma_y'^2}$$

where x_o and y_o denote a randomly generated centroid position of the synthetic spot, and σ_x' and σ_y' control the spread in the x and y directions, respectively, f is the intensity factor which adjusts the brightness of the synthetic spot, and θ_s controls the orientation of the synthetic spot.

2.5.2 Modelling of Actin Filaments

Actin filaments, in general, resemble curvilinear structures [67], whose shapes are hard to approximate. To this end, we model synthetic Actin filaments as a collection of curve segments and approximate each segment using the cubic Bezier curve [68]. The synthetic Actin filaments are also used as motion trajectories which control the animation of synthetic spots over the sequences.

A n orders Bezier curve is a curve that goes from a start point P_0 to an end

point Pn and its shape is controlled by a set of control points P_1 through P_{n-1}. The position at t time step of a cubic (3 orders) Bezier curve $B^3(t)$ is define as,

$$B^3(t) = (1-t)^3 P_0 + 3(1-t)^2 t P_1 + 3(1-t)t^2 P_2 + t^3 P_3,$$
$$0 \leq t \leq 1$$

$$(2.3)$$

The length of each generated cubic Bezier curve is very short (only a very few pixels). One synthetic Actin filament is approximated by connecting a set of m cubic Bezier curves. The end point of the first curve must be same as the start point of the second curve and so on. In addition, the start point of the first curve must not be same as the end point of the last curve since we assume that real Actin filament is never closed.

2.5.3   Addition of Artificial Nosie

We add 3 types of artificial noise into the synthetic TIRFM frames: 1) autofluorescence noise, i.e., the synthetic spots with exponentially decayed brightness over time, 2) fluorescent artefacts, i.e., the synthetic spots with oversized or very elongated shapes, and 3) electronic noise in the background, i.e., Poisson noise. Figure 2.6 show two examples of synthetic TIRFM frames with different backgrounds.

2.6   Evaluation of the Proposed Spot Detection Algorithm

We use Precision and Recall values to quantify the accuracy of our spot detection algorithm and the values are defined as follows,

$$Precision = \frac{TP}{TP + FP}$$
$$Recall = \frac{TP}{TP + FN}$$

$$(2.4)$$
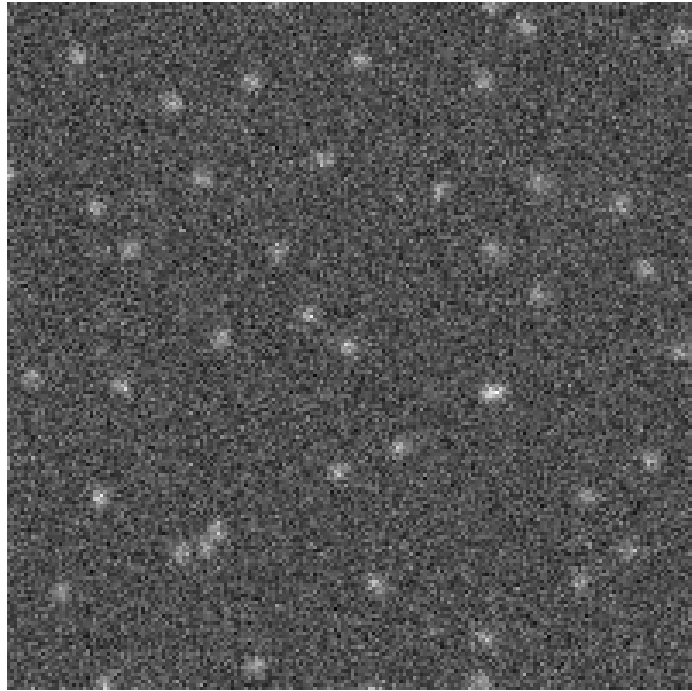
(a)
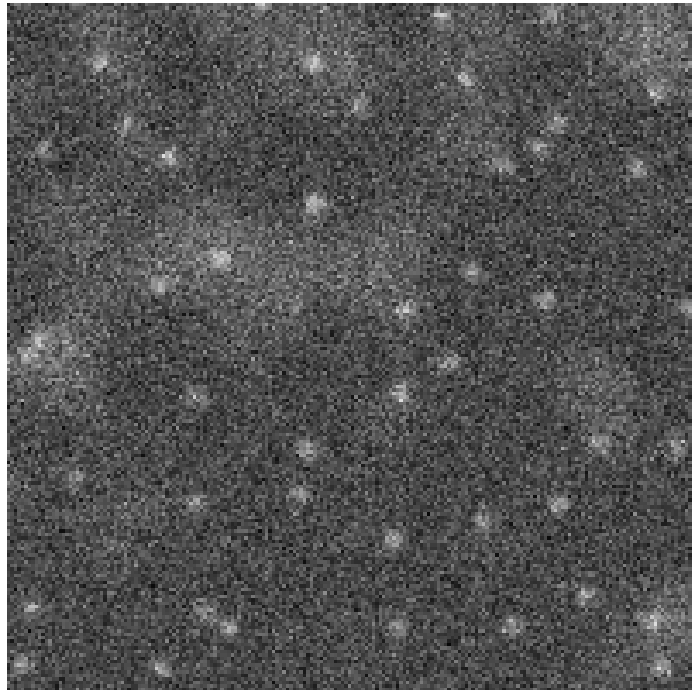
(b)

Figure 2.6: (a) A synthetic frame with type A background. (b) A synthetic frame with type B background. Both synthetic frames depict spots of different sizes.

where a True Positive (TP) is a detected spot that can be found in the ground truth (i.e., manually detected spots), a False Positive (FP) is a detected spot that cannot be found in the ground truth, and a False Negative (FN) is a spot that is not detected by the algorithm but that can be found in the ground truth.

2.6.1 Evaluation on Synthetic TIRFM Images

We generate synthetic TIRFM images with a resolution of 320×320 pixel with one of two types of backgrounds: type A has an uniformly distributed image snrintensity level, while type B contains large cluttered objects that often appear in real TIRFM frames and usually represent large subcellular structures.

In our real TIRFM sequences, spots are usually of different sizes with round or elongated shapes. For the synthetic data, with both type A and B backgrounds, we model round and elongated spots with two sizes; small and large. These elongated spots are generated using different standard deviation values in the x and y directions, within the range $[0.8-1.2]$ for small spots, and within the range $[1.4-2.2]$ for large spots. Round spots are generated by setting the standard deviation to 1.0 in the x and y directions for small spots, and to 1.8 for large spots. Both Figure 2.6 (a) and (b) show different sizes and roundness of the synthetic spots. We generate over 250 randomly-positioned spots for each synthetic frame. Figure 2.6 (a) and (b) shows two synthetic frames with type A and B backgrounds, respectively.

In this work, the synthetic data is distorted by one of three levels of Poisson noise; low, medium or high. Poisson noise is generated by rescaling the intensity values of the frames to different ranges, and the intensity value of each pixel in the rescaled frame is interpreted as the mean of a Poisson distribution that is used to generate a new random intensity value for the corresponding pixel. After rescaling, the frames are rescaled back to the original range of intensities. Low-level Poisson noise (SNR≈49dB) is generated by rescaling the pixel intensities to the range $[1, 60]$, medium-level noise (SNR≈42dB) is generated using the range $[1, 30]$ and high-level

noise (SNR≈33dB) is generated using the range [1, 15].

Table 2.1 reports the accuracy of our spot detection algorithm on synthetic TIRFM frames distorted by three levels of Poisson noise. These results show that the proposed algorithm can detect the majority of large spots in the frames distorted by high-level noise. In the frames distorted by low-level noise, our algorithm reports very few FPs and FNs. We also observe that the proposed algorithm performs slightly better when detecting round spots than when detecting the elongated spots. The proposed algorithm, however, fails to distinguish small spots in those frames distorted by high-level noise. In these cases, a large number of FNs are reported and more than half of the detected spots are FPs, which are produced by the noise. In the frames with type B background, more FNs and FPs are reported due to the cluttered background.

2.6.2 Evaluation on Real TIRFM Images

Our test data set comprises each three frames of five different real TIRFM sequences acquired using a single channel, for a total of fifteen frames, and each frame has a resolution of 320×320 pixel. The ground truth was manually labelled by one of our collaborator and re-validated by two collogues. The experimental results are reported in Table 2.2. It can be observed that the proposed algorithm also attains high precision and recall values on TIRFM Images. The proposed algorithm is implemented in Matlab on a workstation with Intel i5 processor and 8GB RAM, we also report its average processing time on one single frame in Table 2.2.

2.7 Summary

In this chapter, we discussed the difficulties of spot detection in fluorescence microscopy and introduce several related classic methods. We also presented a novel algorithm for detecting Myosin VI spot in TIRFM frames and a novel method for

Table 2.1: Results of the proposed spot detection algorithm on synthetic TIRFM frames distorted with three different levels of Poisson noise.

Background	Round spots			Elongated spots		
	Size	Precision	Recall	Size	Precision	Recall
Low-level noise						
A	Small	0.923	0.997	Small	0.917	0.991
	Large	1.000	1.000	Large	0.997	1.000
B	Small	0.918	0.989	Small	0.921	0.986
	Large	0.996	1.000	Large	0.992	1.000
Medium-level noise						
A	Small	0.837	0.963	Small	0.822	0.945
	Large	0.952	0.967	Large	0.945	0.956
B	Small	0.843	0.959	Small	0.834	0.941
	Large	0.953	0.961	Large	0.935	0.947
High-level noise						
A	Small	0.405	0.928	Small	0.380	0.921
	Large	0.861	0.938	Large	0.854	0.943
B	Small	0.394	0.926	Small	0.386	0.923
	Large	0.846	0.932	Large	0.817	0.939

Table 2.2: Results and runtime of the proposed spot detection algorithm on 5 different real TIRFM sequences of 100 frames.

Sequences	Spots/frame	Runtime(sec/frame)	Precision	Recall
1	55.2	1.67	0.891	0.896
2	67.4	1.87	0.873	0.865
3	89.7	1.92	0.865	0.871
4	98.1	2.14	0.837	0.853
5	123.9	2.48	0.824	0.824
Average	86.9	2.02	0.858	0.862

generating synthetic one-channel TIRFM sequences with animated synthetic fluorescent spots. We evaluated the proposed spot detection algorithm on both real and synthetic one-channel TIRFM frames. The experimental results show that the proposed spot detection algorithm is cable of obtaining accurate measure of Myosin VI spot, which is crucial to the following spot tracking stage.

Chapter 3

Tracking of Myosin VI Protein Spots on Actin Filaments

In this chapter, we introduce an accurate and efficient multi-target spot tracking framework which can be employed to better study the biophysics of Myosin VI protein molecules (spots) in TIRFM sequences. The framework employs the IMM filtering with an extended Hungarian algorithm based data association method. The IMM filtering uses two Kalman filters with distinct motion models to accurately approximate the non-linear dynamics of Myosin VI spots in noisy and dense TIRFM sequences. The data association method is used to deal with measurement-to-target and estimation-to-target assignments problems. Specifically, we use the Hungarian algorithm due to its low computational complexity compared to other data association methods, e.g., MHT and JDPA, when dealing with noisy and dense data. In order to overcome the limitation of bijective mapping in LAP-based methods, which requires equal number of targets in two adjacent frames, we introduce a locality sensitive model with a number of imaginary spots to equalize the spot numbers of two adjacent frames. This work focuses on developing and evaluating an efficient spot tracking framework for Myosin VI spots in TIRFM sequences and therefore, a detailed study of the dynamics of Myosin VI proteins is beyond the scope of this work.

The proposed framework is evaluated on both real and synthetic TIRFM sequences of Myosin VI spots, and the experimental result shows that the framework is fully capable of tracking various molecular motors with properly tuned parameters and motion models.

The remainder of this chapter is organized as follows. Section 3.1 introduces several popular methods for tracking particles/spots in florescence sequences. Two synergistic components of the proposed framework are described in Sections 3.2 and 3.3, respectively, which are an extended Hungarian algorithm and an IMM filter with two distinct motion models, and the framework workflow comprised of these two components is explained in 3.4. Section 3.5 proposes a post-processing step to eliminate error tracks. Section 3.6 presents validation of the proposed framework against three publicly available tracking methods on both synthetic and real TIRFM sequence. Section 3.7 summaries the work presented in this chapter.

3.1 Related Work

Several data association approaches that can be employed to deal with multi-target tracking problems have already been introduced in Chapter 1, e.g., LAP, MHT, and JDPA. These approaches estimate a target's track over a number of frames by matching a candidate target to a track based on the candidate target's similarity to matched targets in the previous frames. Specifically, LAP based methods apply a bijective mapping between two sets of targets in two adjacent frames. The mapping is made by minimizing a sum of costs (dissimilarities) of all possible target pairs arranged in a cost matrix. LAP has been successfully used in feature point tracking methods for analysis of particle trajectories as recorded by video imaging in cell biology [6]. MHT [69] [24] and JDPA [70] [71] based methods estimate how likely it is to match each discovered track to a specific target. MHT performs this estimation over the entire frame sequence, while JDPA separately constructs all pos-

sible assignments between pairs of adjacent frames. Although JDPA is much less computationally expensive than MHT, it does not take into account the target's motion pattern over time, thus it performs poorly in dense situations where targets constantly overlap, disappear, and change directions and speeds.

Bayesian estimation based target tracking methods are Kalman filtering and its extensions, Particle filtering, and IMM filtering. Kalman filtering uses a series of noisy measurements observed over time to estimate the state of a target, e.g., direction, position, and speed. In [72], Kalman filtering is applied with the Mean-shift algorithm to track cell nuclei in Time-Lapse Microscopy. Kalman filtering, however, assumes a single motion pattern for each target, so it performs poorly with non-linear dynamics, such as those of protein molecules. Particle filtering uses Monte Carlo simulations of sample data from targets' states and measurement updates to accurately approximate their behaviours, even in the case of non-linear dynamics. In [53], [55] and [73], advanced Particle filters are proposed for tracking multiple targets in fluorescence microscopy sequences. Particle filtering, however, has a much higher computational cost than that of Kalman filtering. IMM filtering, on the other hand, provides a computationally effective alternative to Particle filtering by associating multiple Kalman filters to one target, where each Kalman filter features a distinct motion model. The posterior state of the target is then a mixture of the different posterior states estimated by each Kalman filter. In [74] and [50], the authors proposed an IMM filter-based method employing several models corresponding to different movement types of moving fluorescent spots. Tracks are constructed thereafter by using a local data association to associate the track with one of the measurements, which has the maximum likelihood estimated by its IMM filter, within the validation gate. One obvious limitation is that data association (track construction) cannot proceed once no measurement is found in the validation gate, in other words, the track is terminated even if the spot is temporally missing due to the incapabilities of spot detection methods or imaging techniques.

Bayesian estimation based approaches, in general, can significantly improve the tracking accuracy but cannot be employed independently [55]. In a mature Bayesian estimation based tracking framework, both the prediction stage in Bayesian estimation and the track construction stage require data association process to deal the measurement-to-target and estimation-to-target assignments, especially in multiple-target tracking. The measurement-to-target assignment problem refers to the coupling of a target in the current frame with its corresponding measurement in the next frame, while the estimation-to-target assignment problem refers to the association of the estimation of a target in the current frame with a candidate target in the next frame [75]. Therefore, Bayesian estimation are often integrated with data association, e.g., MHT [69] [24] and JDPA [76] [55] [71].

3.2   Extended Hungarian Algorithm

An IMM filtering based multi-target tracking process generally faces two assignment problems: 1) assigning spots in a frame with their measurements spots in one of successive frames, and 2) associating pairs of spots in two adjacent frames. The Hungarian algorithm can help to solve these two assignment problems. However, the Hungarian algorithm requires equal number of spots in two adjacent frames, which is normally not the case in TIRFM sequences where spots tend to appear and disappear constantly. To overcome this issue, we extend the Hungarian algorithm by using a locality sensitive model to equalise the number of spots in two adjacent frames. Specifically, the model adaptively adds two types of imaginary spots to the frames: virtual and dummy spots. These imaginary spots also help to resolve discontinuity problems of spot trajectories, which are commonly encountered when spots constantly disappear and reappear along the sequence or when they overlap with other spots. A dummy spot is generated in frame t if a true spot in frame $t-1$ cannot be associated to a measurement (true spot) in frame t within a distance

δ from its position, where δ denotes the maximum distance that a spot can move between adjacent frames. Dummy spots are used in subsequent frames, if needed, to continue a track. The virtual spot, on the other hand, is generated in frame $t - 1$ if a true spot in frame t cannot be associated with any true spot within δ in frame $t - 1$. These concepts are illustrated in Figure 3.1. For example, Tracks A and B in Figure 3.1 represent the case of a true spot splitting into two true spots. Both of the two resulting spots in frame t can be matched to the splitting true spot in frame $t - 1$ within δ. Since only one of them can be associated with the splitting true spot, the other one must be associated with a virtual spot and so, a virtual spot is generated in frame $t - 1$. Tracks E and F, on other hand, represent an example of two spots merging. In this case, the two true spots in frame $t - 1$ merge in frame t. Although both of them can be matched to the merged true spot in frame $t + 1$ within δ, only one of them can be associated with this merged spot. The other true spot must, therefore, be associated with a dummy spot and so, a dummy spot is generated in frame t and is used in frame $t + 1$ to continue track F.

After integrating the locality model with imaginary into the Hungarian algorithm as described above, the cost matrix M_{cost} of two adjacent frames that have unequal number of spots can be constructed. The cost matrix comprises columns that represent the spots in frame $t - 1$ and rows that represent the spots in frame t. Each element in M_{cost} represents the cost coefficient (dissimilarity) between a spot in frame $t - 1$ and a spot in frame t. The cost coefficient between imaginary spots is predefined. Specifically, the cost coefficient between a dummy spot and a virtual spot is set to ∞, which guarantees that assignment between them cannot happen under any circumstances. The cost coefficient between a dummy/virtual spot and a true spot is set to be 0, since it is not possible to determine which true spot must be associated with a dummy/virtual spot at the stage of constructing cost matrix M_{cost}. For a pair of true spots, e.g., spots i and j, 3 types of their features are used to calculate the cost coefficient $cost_{ij}$: the average intensity, I_i and I_j; the area, Ai
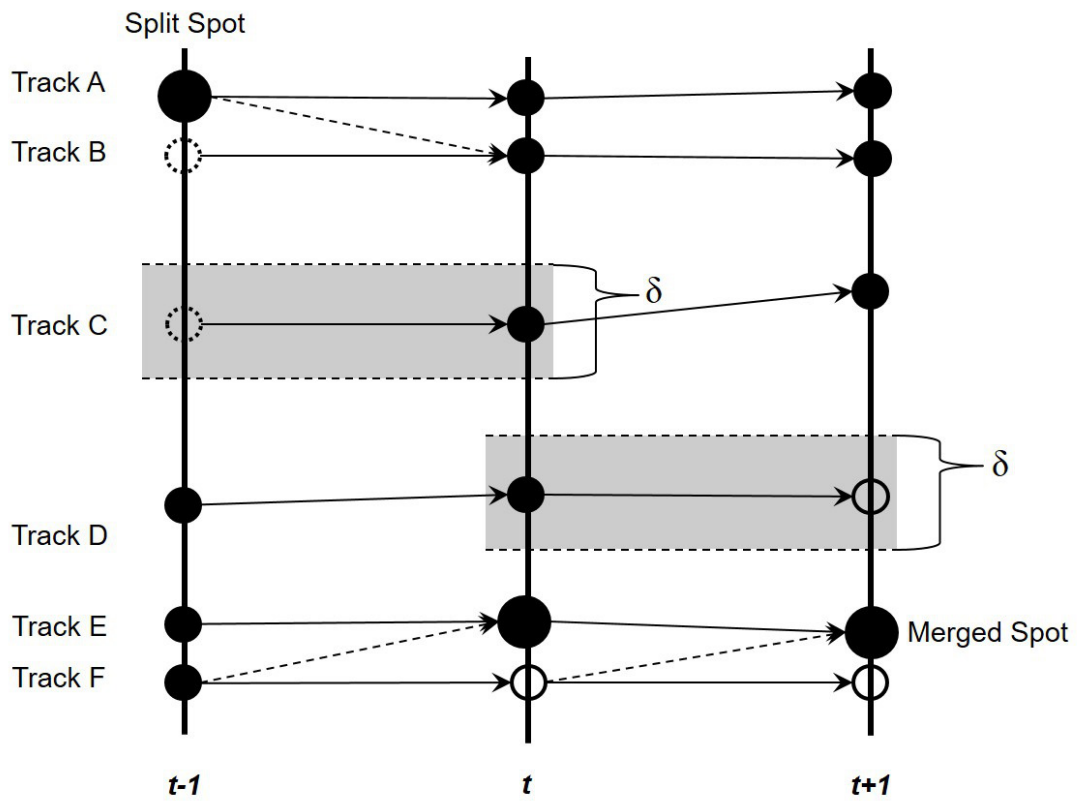
Figure 3.1: An example of the locality sensitive model with imaginary spots. Black solid circles denote true spots, clear circles in a dotted line denote virtual spots, and clear circles in a solid line denote dummy spots.

and Aj; and the centroid, Ci and Cj. The cost coefficient $cost_{ij}$ is calculated as follows,

$$cost_{i,j} = e^{\mathcal{I}} + e^{\mathcal{A}} + e^{\mathcal{C}}$$

$$\mathcal{I} = -\left(\frac{\alpha}{||Ii - Ij||}\right), \quad \mathcal{A} = -\left(\frac{\beta}{||Ai - Aj||}\right), \quad \mathcal{C} = -\left(\frac{\gamma}{||Ci - Cj||}\right) \tag{3.1}$$

where α, β and γ are the parameters that adjust the weight of each feature. Their values can be derived from the weights given to intensity, position and size in the manual spot tracking.

Using the cost matrix M_{cost} as defined above, we can compute a bijective mapping between spots in M_{cost} by finding, among all possible mappings, those pairs of spots that result in the minimum total cost.

3.3   IMM Filter with Two Motion Models

The IMM filter used in the proposed tracking framework uses two motion models for each Kalman filter [28]; M_1: nearly constant velocity with a small acceleration [77] and M_2: Gauss-Markov mobility [78]. These two motion models are selected due to their capability to approximate the non-linear dynamics of Myosin VI spots. We assume that the movement of a Myosin spot on Actin filament is a composite of unbound, freely diffusing and weakly bound states, that is diffusive motion trapped by affinity for a fixed structure (Actin filament). This sort of caged spot moves with a constant velocity along on their rails but can sometimes also exhibit a random motion just like a spot with pure diffusive motion within a very short time period. The state evolution equation of the nearly constant velocity model is defined as

38

follow,

$$S_t = M \cdot S_{t-1} + q_t$$

$$M = \begin{pmatrix} 1 & \Delta T & 0 & 0 \\ 0 & 1 & 0 & 0 \\ 0 & 0 & 1 & \Delta T \\ 0 & 0 & 0 & 1 \end{pmatrix} \tag{3.2}$$

$$\Sigma = \begin{pmatrix} \frac{\Delta T^3}{3} & \frac{\Delta T^2}{2} & 0 & 0 \\ \frac{\Delta T^2}{2} & \Delta T & 0 & 0 \\ 0 & 0 & \frac{T^3}{3} & \frac{\Delta T^2}{2} \\ 0 & 0 & \frac{\Delta T^2}{2} & \Delta T \end{pmatrix}$$

where $S_t = [x_t, y_t, \dot{x}_t, \dot{y}_t]^T$ is the state (coordinate and velocity) vector at time step t; x_t and y_t are the coordinates; $\dot{x}_t$ and $\dot{y}_t$ are the velocities in x and y directions, respectively; M is the state transition matrix; Σ is the covariance matrix of noise q_t at time step t, and ΔT is the time interval between two adjacent frames.

The Gauss-Markov mobility model provides different levels of randomness to the direction and speed of Myosin VI spot. This model compensates for the lack of direction and speed changes in the first model. In addition, it avoids sudden direction and speed changes by updating the current direction and speed state based on previous states. The updating equation of the Gauss-Markov mobility model is defined as follow,

$$s_t = \alpha s_{t-1} + (1 - \alpha)\bar{s} + \sqrt{1 - \alpha^2} s_{x_{t-1}}$$
$$\theta_t = \alpha \theta_{t-1} + (1 - \alpha)\bar{\theta} + \sqrt{1 - \alpha^2} \theta_{x_{t-1}} \tag{3.3}$$

where s_t and θ_t are the speed and the direction of a spot at time t, $\bar{s}$ and $\bar{\theta}$ are the constant mean speed and mean direction respectively, and $s_{x_{t-1}}$ and $\theta_{x_{t-1}}$ are random variables that take real values within the range $(0, 1)$.

39

The level of randomness is controlled by α, where $0 \leq \alpha \leq 1$; $\alpha = 0$ generates totally random values which exhibit Brownian motion, whereas $\alpha = 1$ results in linear motion. The position state vector (x_t, y_t) of a spot is updated as follows,

$$x_t = x_{t-1} + s_{t-1} \cos \theta_{t-1}$$
$$y_t = y_{t-1} + s_{t-1} \sin \theta_{t-1}$$

(3.4)

For each of the two motion models, a model transition matrix is used to represent the probabilities of switching from itself to the other. In this work, we use a quasi-Bayesian algorithm which uses an on-line minimum Mean Squared Error (MSE) estimation to adaptively tune the elements in the model transition matrix [79] [80].

3.4 Workflow of the Proposed Multi-target Spot Tracking Framework

This section details workflow of the proposed tracking framework, which is depicted in Figure 3.2. In step 1, the tracking algorithm processes a pair of adjacent frames: frames $t - 1$ and frame t. First, imaginary spots are added into the two frames and the cost matrix M_{cost} is constructed. Next, the extended Hungarian algorithm computes the bijective mapping between spots in M_{cost} to assign a measurement in frame $t - 1$ to each spot in frame t. In step 2, the states (i.e., position and speed), the state covariance, and the measurement of each spot in frame $t - 1$ are used to predict their new states and state covariances in frame t using the proposed IMM filter. In step 3, the tracking algorithm associates all types of spots in the two adjacent frames to establish, continue or terminate track segments. First, the predicted states of spot are used to update the corresponding states in frame $t - 1$. Previously added imaginary spots are then removed and new imaginary spots are added based on the updated spots. Next, the tracking algorithm constructs a new

cost matrix M_{cost} between the updated spots in frame $t-1$ and the spots in frame t. The extended Hungarian algorithm is used again to associate the updated spots in frame $t-1$ with the spots in frame t, which continues the established track segments. Finally, tracks are updated and the tracking algorithm process the next pair of adjacent frames; frame t and frame $t+1$. As part of the track updating procedure in this step, it is important to note the following two observations: 1) track segments with more than one true spot are terminated if they are continually associated with more than five dummy spots. That is, in this work, the framework stops tracking a spot if it disappears for five consecutive frames. This number of consecutive frames is selected as the cut-off based on practical observation in the manual tracking. We observe that the majority (around 87%) of tracks are not continued if the corresponding spot disappears for five consecutive frames. 2) In order to remove noisy spots due to electronic noise, a terminated track segment is permanently eliminated if no more than three true spots are associated with this track segment. Also, a track segment with only one true spot is terminated if it is continually associated with three dummy spots (recall that noisy spots due to electronic noise usually persist for up to 2-3 frames).

3.5   Elimination of Error Tracks

In order to remove due error tracks (mostly caused by auto-Fluorescence noise being detected as spots), an exponential function and a constant function are fitted to the intensity values of the spots in those track segments associated with more than 10 true spots. The exponential function $f_{exp(i)}$ and the constant function $f_{con(i)}$ are defined as follow:

$$f_{exp}(i) = N_0 e^{-\lambda i}, 0 \le i \le N_{spot} - 1$$
$$f_{con}(i) = at + b, 0 \le i \le N_{spot} - 1$$

$$(3.5)$$

Step 1: Measurement Association

Process of a pair of adjacent frames: the current frame $t-1$ and the next frame t

Addition of imaginary spots and construction of cost matrix M_{cost}

Hungarian algorithm: bijective mapping using cost matrix M_{cost}

Association between spots in the current frame $t-1$ and measurements in the next frame t

Step 2: IMM Filtering

Computation of predicted states and state covariances of spots in the current frame $t-1$ using their associated measurement, states and state covariance in the next frame t

Kalman filtering using Motion Model 1

Kalman filtering using Motion Model 2

Predicted state and state covariances

Predicted state and state covariances

Likelihood of measurement of each filter in the next frame t

Probability of each model in the next frame t

Combined states and state covariances in the next frame t

Step 3: Spot Association

Update of states of spots in the current frame $t-1$

Removal of previously added imaginary spots. Addition of new imaginary spots and construction of cost matrix M_{cost}

Hungarian algorithm: bijective mapping using cost matrix M_{cost}

Association between spots in the current frame $t-1$ and spots in the next frame t

Update the tracks and process the next pair of adjacent frames: the current frame t and the next frame $t+1$

Figure 3.2: Workflow of the proposed multi-target spot tracking framework for Myosin VI spots in TIRFM sequence.

where i is the spot index, N_{spot} is the total number of spots associated with the track segment, and N_0, λ, a, b are the parameters estimated using least squared fitting.

As the intensity of a noisy spot due to cellular auto-fluorescence noise decays exponentially with time, if the MSE of the fitted exponential curve is less than the MSE of the fitted constant curve, the track segment is more likely to be a noise and is permanently eliminated. For those track segments with less than ten true spots, if the intensity of the last associated spot is lower than half of the intensity of the first associated spot, the track segment is also considered as a noise and it is also permanently eliminated.

3.6 Evaluation of the Proposed Spot Tracking Framework

The complete tracking framework is implemented in Matlab and evaluated on both synthetic and real TIRFM sequences. For this evaluation, our test data set comprises two synthetic sequences and three real TIRFM sequences, with 500 frames each. One of the real TIRFM sequences is acquired using two colour channels, while the rest are acquired using single channel.

In the synthetic sequences, each frame has a resolution of 320×320 pixels and is distorted by medium-level Poisson noise. We add three types of synthetic spots: 1) diffraction-limited spots due to bound GFP-Myosin molecules, which slightly change size and intensity (almost constantly), randomly disappear a few times for less than 4 frames throughout the sequence, and move along Actin filaments generated using the Bezier curve approach; 2) noisy spots due to electronic noise, which do not persist for more than 3 frames and randomly disappear 1-2 times for less than 2 frames throughout the sequence; and 3) noisy spots due to cellular auto-fluorescence noise, which randomly move and disappear a few times for less than 4 frames throughout

the sequence, and whose intensity values decay exponentially with time, according to 3.5 with $\lambda = 0.75$ and N_0 (initial intensity value) in the range [150,220].

The real two-channel TIRFM sequence (see Figure 2.3 in Chapter 2) depicts Actin filaments in the red channel and Myosin VI proteins in the green channel. For this particular two-channel sequence, we are only interested in tracking the detected spots on the Actin filament, since Myosin VI proteins are known to attach on, and move along Actin filaments. To this end, we use the red channel to segment the Actin filaments first. We then remove all detected spots in the green channel that are not located within the spatial extent of the segmented Actin filaments. The framework can then exclusively tracks the detected spots on the Actin filaments. For the real one-channel TIRFM sequences, all detected spots are tracked since no prior information about the position and shape of Actin filaments is available.

We compare the proposed spot tracking framework, with the Hungarian algorithm based tracking method (without using IMM filtering and a locality sensitive model), and with three publicly available multi-target spot tracking methods; namely, ParticleTracker (MOSAIC) - an ImageJ plugin that employs a feature point tracking algorithm [81]; GMimPro - a C++ software that employs an Automatic Single Particle Tracking (ASPT) algorithm [44], and u-track 2.0 - a Matlab package that is based on a LAP method and Bayesian filtering with two motion models [24].

The Optimal Sub-Pattern Assignment (OSPA) error metric is used to quantitatively evaluate the performance of all evaluated tracking methods (Ristic et al., 2011). The OSPA error metric integrates information about tracking accuracy and number of missed and false tracks into a single value. This error metric is computed between two sets of tracks, one of which is the ground truth and the other one is estimated by the tracking method. Specifically, the OSPA error metric computes the cardinality error and the location error. The cardinality error is a measure of penalty assigned to missed or false tracks, e.g., a gap within a track, incorrect spot assignments in a track, a beforehand suspended track or a track jointed by two

tracks. A smaller cardinality error represents less missed or false tracks. On the other hand, the location error is a measure of penalty assigned to position differences between two tracks at each time step. A small location error value means that the average of Euclidean distances between two tracks at each time step is short. In our case, the OSPA error is the summation of the cardinality and location errors; an OPSA error value of zero indicates an exactly precise tracking while a higher OSPA error value corresponds to a worse performance of the spot tracking. Table 3.1 shows the OSPA errors produced by the different tracking methods on the test synthetic and real TIRFM sequences. Figure 3.3 shows the 3D plot of the tracks produced by the proposed framework and u-track (which is the one with the lowest OSPA error values among the three publicly available methods) for 300 frames of a real one-channel TIRFM sequence. It ican be observed that the proposed spot tracking framework produce more consistent and smooth trajectories of spot than u-track.

Cardinality errors in Table 3.1 show that imaginary spots employed by the extended Hungarian algorithm significantly enhance the tracking performance (i.e., they reduce the cardinality error) by filling gaps in tracks, e.g., spots disappearing or overlapping. Note that the OSPA errors of the proposed framework are smaller than that of the Hungarian algorithm with no IMM filtering, especially in dense sequences. This proves that modelling the complex dynamics of Myosin VI proteins by using the motion models of the proposed framework improves the tracking accuracy.

Overall, OSPA error values in Table 3.1 show that the performance of the proposed spot tracking framework is comparable to that of other publicly available methods. For the two-channel real TIRFM sequence, the proposed spot tracking framework and other publicly available methods show good accuracy for tracking those spots on the Actin filaments since the majority of noisy spots are usually not located on the Actin filaments. However, for the real one-channel sequences, the OSPA error values of Mosiac and GMimPro are worse than those of the proposed

(a)

(b)
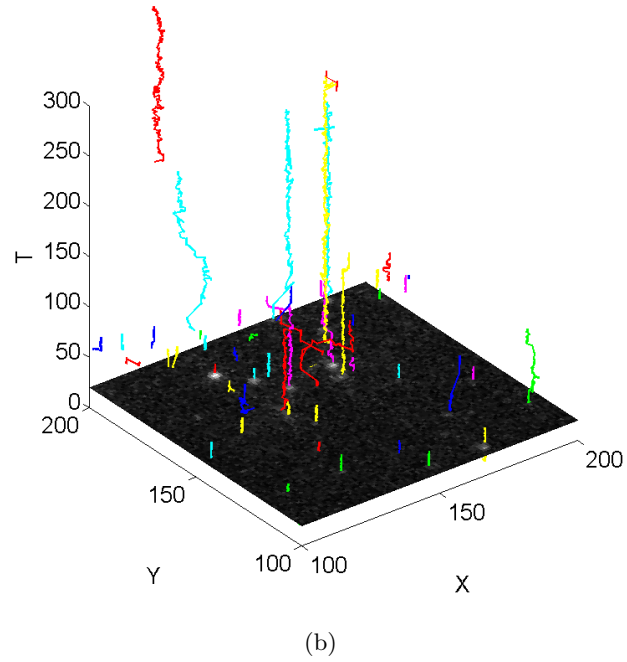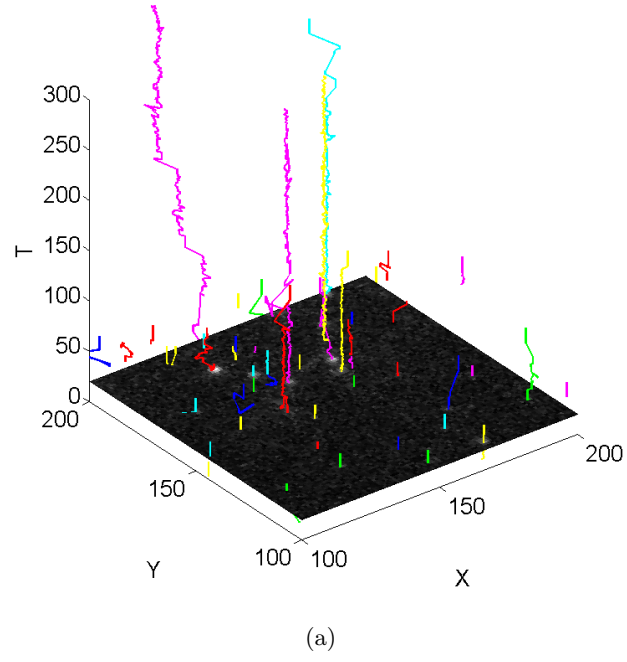
Figure 3.3: 3D plot of the tracks produced by (a) the proposed spot tracking frame-work and (b) u-track for 300 frames of a real one-channel TIRFM sequence. Results show a region of the frames from [1-100] in both the x and y directions. Each individual track is depicted in a different colour.

Table 3.1: OSPA errors for the proposed spot tracking framework and other methods on synthetic and real TIRFM sequences. The two best results are shown in bold font.

Errors	Hungarian	Proposed	Mosaic [81]	GMimPro [44]	u-track [24]
Real two-channel TIRFM sequence (31.2 spots per frame)					
Cardinality	1.81	0.94	1.11	1.03	1.26
Location	2.31	1.10	1.32	2.14	1.23
OSPA	4.12	**2.04**	2.43	3.17	**2.59**
Real one-channel TIRFM sequence (53.3 spots per frame)					
Cardinality	4.37	1.21	3.13	3.12	2.76
Location	5.45	2.42	3.45	4.12	3.92
OSPA	9.82	**3.63**	6.58	7.24	**6.68**
Real one-channel TIRFM sequence (124.6 spots per frame)					
Cardinality	5.15	2.14	3.14	4.77	4.39
Location	7.23	3.57	5.72	4.58	4.23
OSPA	12.38	**5.71**	8.86	10.35	**8.62**
Synthetic one-channel sequence (73.6 spots per frame)					
Cardinality	5.27	4.12	5.45	6.81	5.24
Location	6.62	5.43	8.03	9.42	8.15
OSPA	12.89	**9.55**	13.48	16.33	**13.39**
Synthetic one-channel sequence (313.5 spots per frame)					
Cardinality	12.67	5.21	7.15	8.13	7.08
Location	16.31	7.33	10.72	10.43	9.31
OSPA	28.98	**12.54**	17.87	18.56	**16.39**

spot tracking framework. This is mainly due to two reasons. First, the proposed spot tracking framework is capable of removing noisy spots in the pre-processing stage and during the tracking stage, which significantly reduces the number of erroneous tracks. Less noisy spots usually results in less incorrect spot associations especially when dealing with spots merging/splitting. Second, although Mosaic uses a LAP-based method that is similar to the extended Hungarian algorithm, it does not benefit from modelling the motion patterns of spots. GMimPro uses a Nearest-Neighbour (NN) based method to perform tracking. In general, NN based methods attain a high accuracy for single-target tracking. Their performance is, however, poor when dealing with multiple targets that constantly overlap. Therefore, both Mosiac and GMimPro result in lower localisation accuracies and more incorrect spot associations, which leads to higher location errors than those of the proposed spot tracking framework.

Note that OSPA errors of Mosaic and GMimPro are high in extremely dense TIRFM sequences, e.g., the last synthetic sequence in Table 3.1, which has more than 300 spots per frame. These large errors are mainly the result of the large number of false positive detections produced by these two methods; and the fact that LAP (Mosaic) and NN (GMimPro) based methods are very likely to produce a large number of erroneous tracks without the support of Bayesian estimation filtering, especially when dealing with overlapping targets in dense data.

It is important to mention that u-track is also a LAP based method with Bayesian estimation filtering, but it uses two different motion models from ours: a Brownian and a direct motion model. However, the results show that the location error values attained by u-track are higher than those attained by the proposed spot tracking framework, particularly for extremely dense data. In addition, our extended Hungarian algorithm produces less false tracks than the LAP method employed by u-track, therefore the proposed spot tracking framework yields much less cardinality errors. In conclusion, the motion models and the data association

method developed in the proposed spot tracking framework has an advantage of more accurately approximating the biophysics of Myosin VI protein particles.

Mean Square Displacement (MSD) is generally used to analyse the biophysics of particles for determining their motion mode over a period of time. MSD can be employed as a powerful tool to quantify tracking methods e.g. it is used in [82] to quantify the tracking results. We used the MSD algorithm in [83] to quantify accuracies of the proposed spot tracking framework and three other publicly available methods against the ground truth, which computes the weighted average over all MSD curves of particle trajectories, weights are taken to be the number of averaged delay (time interval) in individual curves. MSD experimental sequence is a set of 250 consecutive frames (approximately $12s$, a time interval of $0.048s$) selected from a real TIRFM sequence, in which $1,073$ tracks are manually marked in total as the ground truth. Figures 3.4 to 3.8 show the weighted averaged MSD curves of the manually marked tracks and a montage of tracks generated by the proposed spot tracking framework and 3 other methods on the MSD experimental sequence, respectively.

The MSD curve of purely diffusive motion i.e., Brownian motion, normally appears as a straight line started from the origin with a positive slope along the x-axis. The weighted standard deviations are also gradually increased over time. The average MSD curve of ground truth is almost a rapidly ascending straight line before 0.8s, as well as the weighted standard deviations, which exactly shows that the motion of Myosin spot is diffusive at a very short time scale. The curve saturates and progresses smoothly as a straight line again until at around 6.5s, then it fleetly goes down and forms a spike again at around 11s, which tells that the motion becomes hindered by some mechanism after 6.5s. An extremely high peak of the weighted standard deviations is found at around 6.5s but drops significantly until 7.5s, which shows that all spots turn to have small displacements during 6.5-7.5s. We also observe both the average MSD curve and its weighted standard deviation
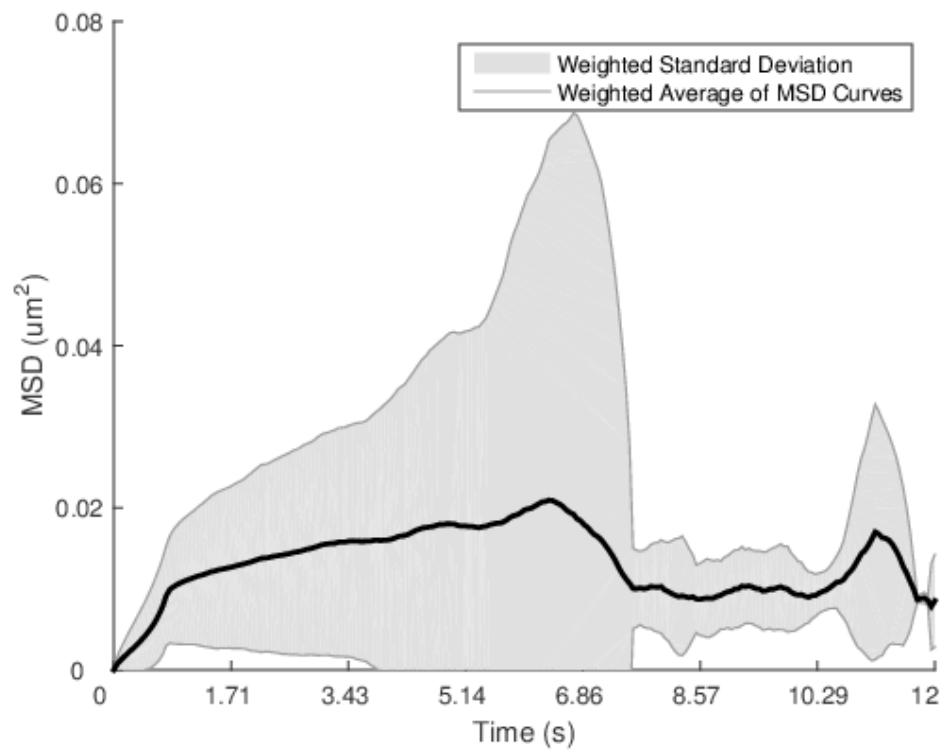
Figure 3.4: Weighted Average Mean Square Displacement (MSD) curves of the manually marked tracks (Ground Truth).
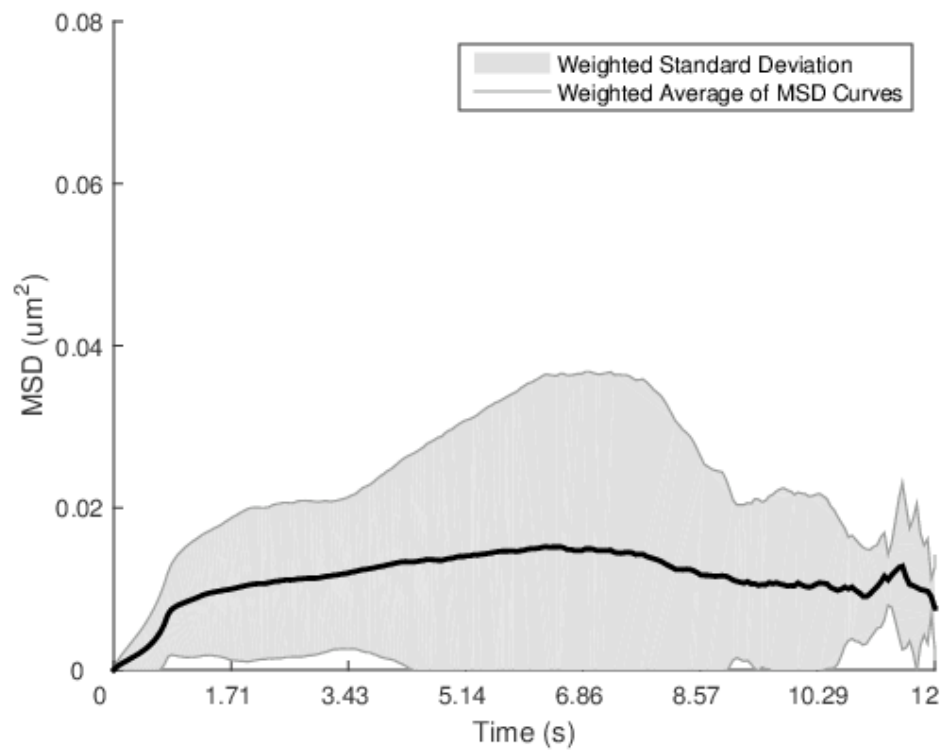
Figure 3.5: Weighted Average Mean Square Displacement (MSD) curves of a montage of tracks generated by the proposed spot tracking framework.
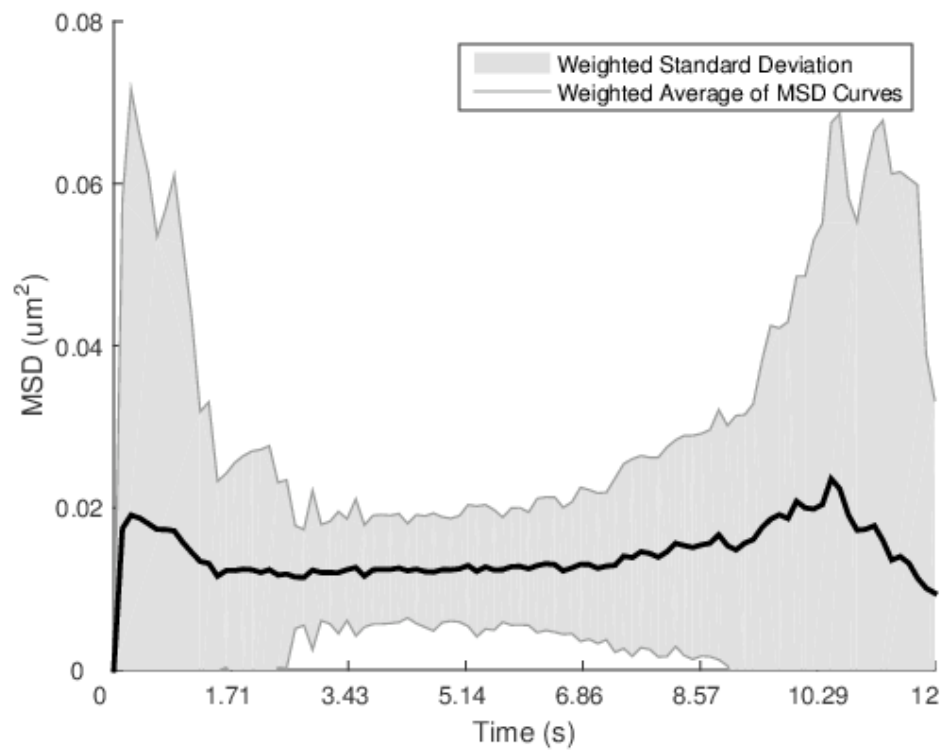
Figure 3.6: Weighted Average Mean Square Displacement (MSD) curves of a montage of tracks generated by Mosaic.
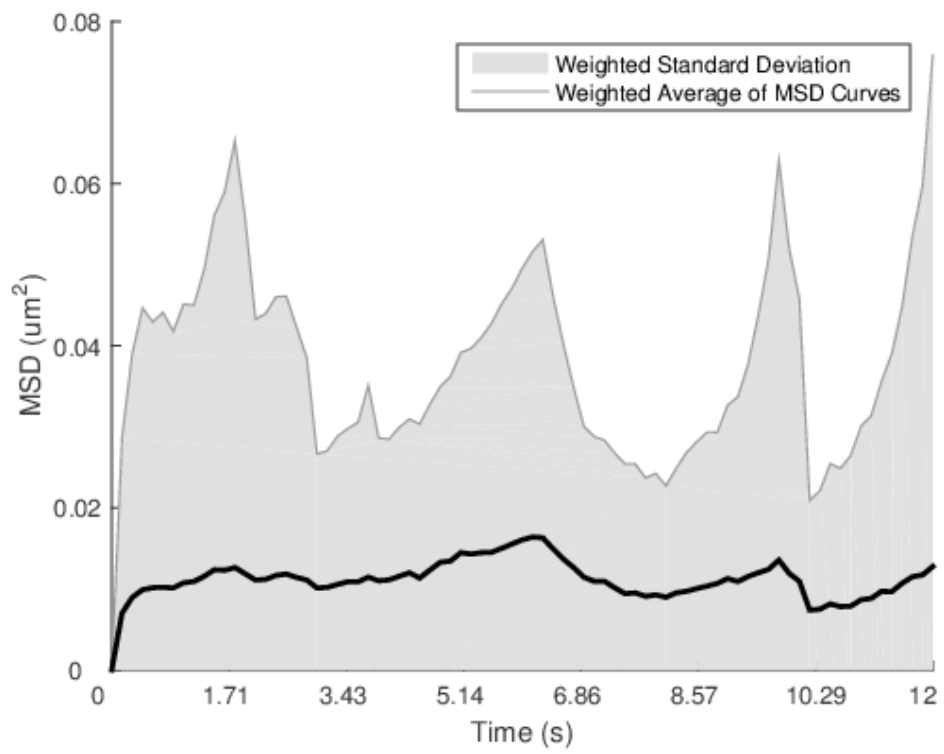
Figure 3.7: Weighted Average Mean Square Displacement (MSD) curves of a montage of tracks generated by GMimPro.
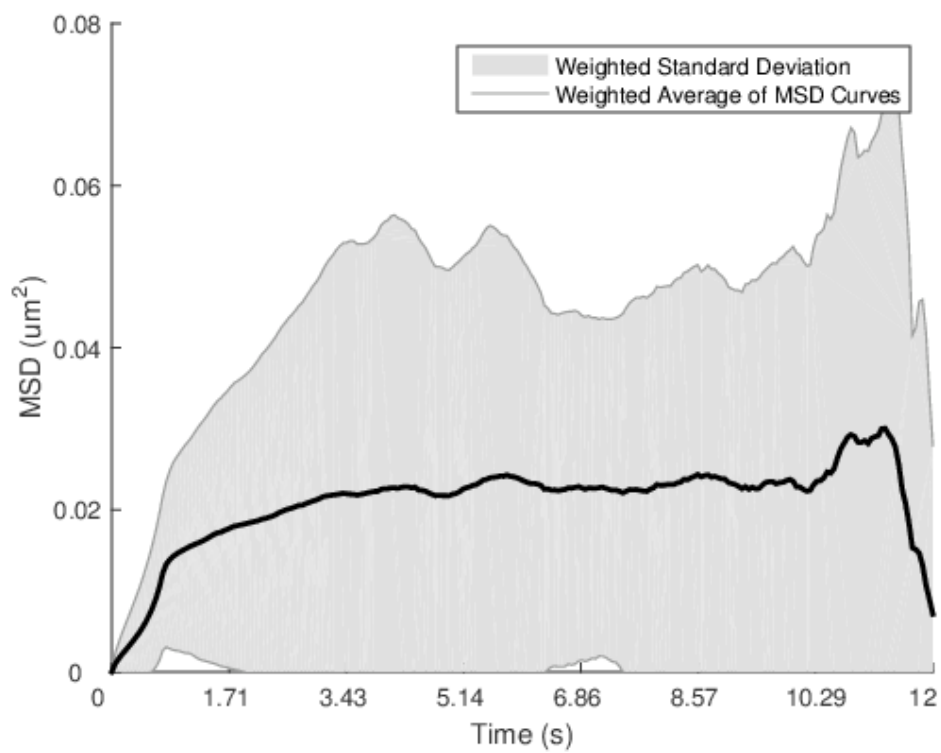
Figure 3.8: Weighted Average Mean Square Displacement (MSD) curves of a montage of tracks generated by u-track.

region have a small peak at around 11s.

Mosaic generated 974 tracks and quite few of them are short and discontinuous. The averaged MSD curve of these tracks saturates just within 0.4s for the first time, which is much faster than Ground Truth. Then, similar to Ground Truth, the curve keep increasing smoothly but has lower values, and also saturates for the second time at around 6s. But the third peak of the curve is found at around 9.5s which is a bit earlier than the Ground Truth. It is also obvious that the weighted standard deviation region of the curve has totally different shape. It has four peaks and the lowest one is at around 6.5s, at where Ground Truth has the highest one amongst the two peaks. GMimPro produced over 1,011 tracks which is very close to the Ground Truth. However, the average MSD curve GMimPro has a totally different shape. The curve saturates even faster the curve of Mosaic. Also, the first peak reaches near $0.02\mu m^2$ which is twice higher than $0.009\mu m^2$ of the Ground Truth. Notice that no peak is found at around 6s and the weighted standard deviation region are very narrower from 1.7s to 6.8s but becomes thicker afterwards, which is in an opposite way compared to the Ground truth. The average MSD curves of Mosaic and GMimPro show that they cannot accurately depict the true motion patterns of Myosin VI spots.

On the other hand, the proposed spot tracking framework and u-track both show more promising MSD curves, perhaps due to the Bayesian filtering with appropriate motion models. The number of tracks produced by u-track is 1,245, which is a bit higher than the Ground Truth. The MSD curve of u-track appears quite similar to that of Ground Truth before 6.5s, but shows higher MSD and weighted standard deviation values all the time. After 6.5s, the MSD curve of u-truck does not fall down as the Ground Truth. Also, the peak at around 11s is much higher than that of Ground Truth. More importantly, the MSD curve of u-track drops dramatically at 11s to a low value at 12s. Furthermore, the weighted standard deviation region of the MSD curve of u-track is wider, and shows no peak but a valley at around 6s.

It is also obvious that the weighted standard deviation region of u-track is a much wider than that of Ground Truth after around 7.7s.

The number of tracks generated by the proposed spot tracking framework is slightly higher than that of Ground Truth, i.e., 1127 tracks. Overall, the MSD curve and its weighted standard deviation region of the proposed spot tracking framework resembles those of Ground Truth, expect the curve falls slowly after 6.5s without making an obvious peak. In addition, the proposed spot tracking framework has slightly lower MSD and weighted standard deviation values than that of Ground Truth. In the MSD curve of the proposed spot tracking framework, the weighted standard deviation region becomes much wider after 3.4s and it also form a peak at around 6.5s, which is similar to but not as abrupt as that of Ground Truth. Besides, the proposed spot tracking framework also shows a wider weighted standard deviation region from 7.7s up to 10.5s, but the region is more close to that of Ground Truth than that of u-track.

To conclude, the proposed spot tracking framework shows the most similar approximation of the averaged MSD curve of Ground Truth. In other words, the framework can more accurately reveal the motion patterns of Myosin VI proteins on Actin filaments. It is noticeable that all weighted average MSD curves can reduce within a short period of time, and commonly show valleys and peaks, which are most likely caused by stuck and noisy spots. Figure 3.9 shows that the individual MSD curve of manually marked tracks of five different spots, i.e., stuck spots or noisy spots caused by static noise/camera electronics.

3.7 Summary

In this chapter, we proposed a novel spot tracking framework for Myosin VI proteins on Actin filaments in TIRFM sequences. Two motion models are incorporated in the IMM filtering, which enables the filter to accurately approximate the non-linear
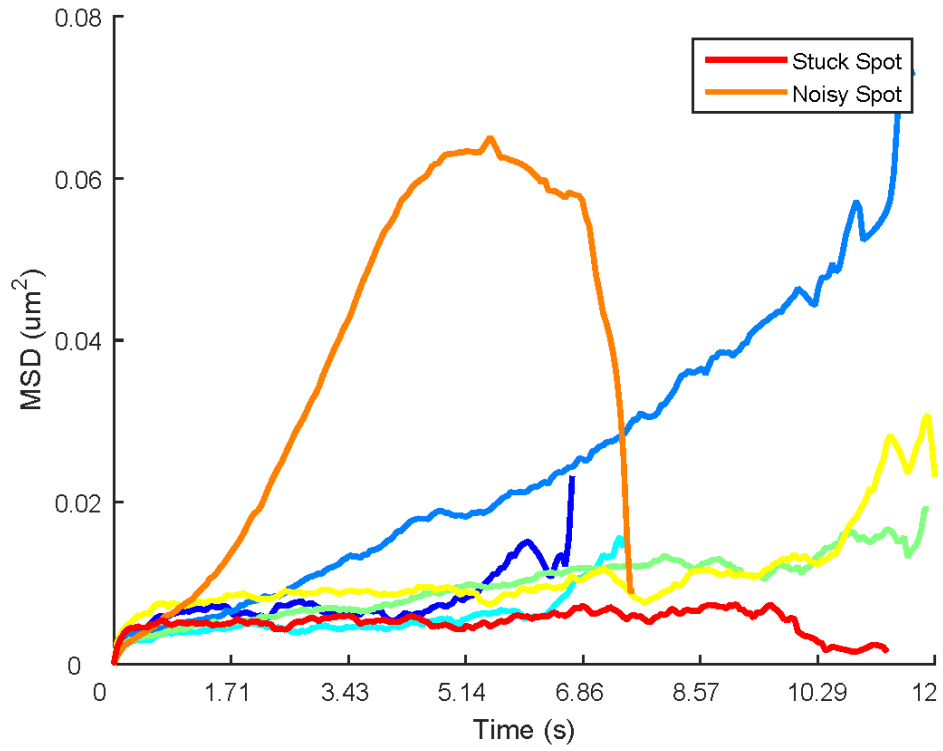
Figure 3.9: Individual MSD curves of the tracks of five different spots, red curve presents the MSD of a stuck spots track, orange curve presents the MSD of a noisy spots track due to static noise or the camera electronics, the rest curves present the MSD of Myosin spots.

motion of Myosin VI spots. The conventional Hungarian algorithm, which is limited in bijective mapping problem, is reinforced by a locality sensitive model with two types of imaginary spots, can now successively deal with the measurement-to-target and estimation-to-target assignment problems in the IMM filtering. The improved Hungarian algorithm can be used for Bayesian estimation based tracking as a much less computational expensive alternative to replace MHT and JPDA. The experimental results show that the proposed spot tracking framework can offer several significant advantages compared with the three well-known publicly accessible spot tracking methods for TIRFM sequence of Myosin VI; and the accuracy of our framework, in terms of both OPSA error metric and MSD, is higher than that of the other methods.

Chapter 4

Cell Detection and Luminal Epithelium Localisation in Endometrial Histology Images

Cell detection is the very first step in order to calculate the ratio of UNK cells to stromal cells in endometrial histology images. In the first stage of developing the automatic recurrent miscarriages diagnostic system, we were requested by our collaborator such that the diagnostic process is compounded by the fact that cell counting must be performed within image regions near the edges of luminal epithelium, but the cells located within $200\mu m$ to the edges should not be counted. Therefore, localising the edges of luminal epithelium plays an important role in obtaining meaningful image regions and removing irrelevance cells from the detection for accurate cell counting.

In this chapter, we present a complete solution for detecting stromal and UNK cells and also for localising the edge of luminal epithelium. We improve a local phase symmetry based method for detecting stromal cells, and propose an adaptive background removal method for segmenting brown stain regions (which are used

for identifying UNK cells). We also propose a novel method for localising luminal epithelium, it fits a B-Spline curve on the epithelial cells (which are identified using an alpha shapes method) to mark the edges of luminal epithelium. We evaluate the proposed detection and localisation methods against a state-of-the-art commercial software. The experimental results show that the proposed methods attain higher accuracy and less computational expensive than the commercial software, which is fully capable of providing precise cell counts, and therefore can be deployed in a mid-range computer on a daily basis.

This chapters is organized as follows. Section 2.1 introduce the details of generating endometrial histology image datasets. Section 4.2 discusses several conventional cell detection methods fo different biomedical images. Sections 4.3 present the methods for detecting stromal and UNK cells, respectively. and 4.4 present a method for localising luminal epithelium edges. Section 4.5 evaluates the proposed solution. Section 4.5 summaries the achievements in this chapter.

4.1 Methodology

Endometrial biopsies for UNK testing were collected in a clinic at University Hospitals Coventry and Warwickshire (UHCW) NHS Trust from patients suffering from recurrent pregnancy loss or recurrent IVF treatment failure. Written informed consent was obtained prior to tissue collection. The biopsies were taken in the mid-luteal phase and obtained using an Endocell Disposable Endometrial Cell Sampler (Wallach, USA) as shown in Figure 4.1 (a)). The tissue was fixed in 10 formalin and embedded in paraffin wax. Sections (3μm) were labelled with anti-CD56 monoclonal antibody as per standard protocols in the pathology laboratory at the hospital. The biopsy slides were stained with Haematoxylin (for cell nuclei) and Diaminobenzidine (DAB) (for UNK cell nuclei labelled with anti-CD56). Cell nulcei were stained purple/blue with Haematoxylin and UNK cells were also covered by

brown stain regions when using DAB staining. The whole slide images of stained tissue sections were scanned using Mirax Midi (Zeiss, Germany, shown in Figure 4.1 (b)) at 0.25μm/pixel and were assessed using Panoramic Viewer [84] to identify regions for analysis. Images were captured for identified regions in the high power fields (HPFs) of the whole slide images at $40\times$ magnification and saved in the JPEG format. Figure 4.1 (c) shows a local region of a whole slide image viewed in Panoramic Viewer at $5\times$ magnification. The number of cells in each HPF image was counted manually using the cell-counter function in ImageJ and cross-validated by two experts (pathologists from UHCW). This was used to calculate the ratio of UNK cells to stromal cells and converted into a percentage for the diagnosis of recurrent miscarriage due to over-presence of UNK cells.

4.2   Related Work

A variety of methods have been proposed to address cell detection problems in histology images. The detection are usually obtained from segmented cell. One class of the conventional and relatively simpler cell segmentation methods are based on intensity analysis: e.g., thresholding [85] and clustering [86] [87].These methods are only feasible when a high intensity contrast between the cells and background is presented. However, these methods often fail at segmentation overlapping cells, this is because that their intensity levels at the overlapped regions are highly similar. The other types of segmentation methods involves, e.g., watershed transform [88] [89] [90] and morphological filtering [91] [65] [92] [93], they usually provide implicit detection result and are more often used as a pre-processing step in the pipeline.

Another popular cell detection solution is based on active contours, which iteratively expand the contour base on sort of energy functions from seed points, until reaching the cell boundaries to accomplish the segmentation. Several active contour models have been proposed in [94] [95] [96] [86] [87] to cope with different

(a)

(b)

(c)

Figure 4.1: (a) Process of taking biopsies using a Endocell; (b) Mirax Midi (Zeiss, Germany) whole slide scanner; (c) A local region of a whole slide image viewed in Panoramic Viewer at 5× magnification

scenarios. The accuracy of active contour based method is heavily depended on the seed points and energy functions, which often cause over-segmentation and under-segmentation on overlapping cells or those cells with unique positions, colours or shapes compared. In addition, actor contours are computationally expensive so that their performance can be dramatically slow on the images containing thousands of cells.

Above methods can be categorized as unsupervised learning, which are tailored by utilising some subjective assumptions or prior knowledges regarding the image contents, e.g., the cells appear in blob shapes or they have distinct stain colour compared with to other background objects. Another more complicated and advanced methods are based on supervised learning. These methods are often employed to classify different types of cells or tissues [97], but it can also be applied for cell detection. Supervised learning based methods learn the features of cells in a training stage which requires inputs of cells as negative samples and of background as positive samples and classify images region as either cells or background based on the learned features by using classifiers e.g., SVM [98] [97] and Random Forests [99] [100]. Therefore, sufficient samples, feature description and correctly chosen classifier are crucial for these methods.

4.3 Counting of Stromal and UNK Cells

We first separate the input image into two underlying stain channels, Haematoxylin and DAB (CD56), using a colour deconvolution method proposed in [101]. The Haematoxylin channel is used to detect stromal cells and the DAB channel is used to segment brown stain regions for identifying UNK cells. The workflow of stromal and UNK cell detection is shown in Figure 4.2.
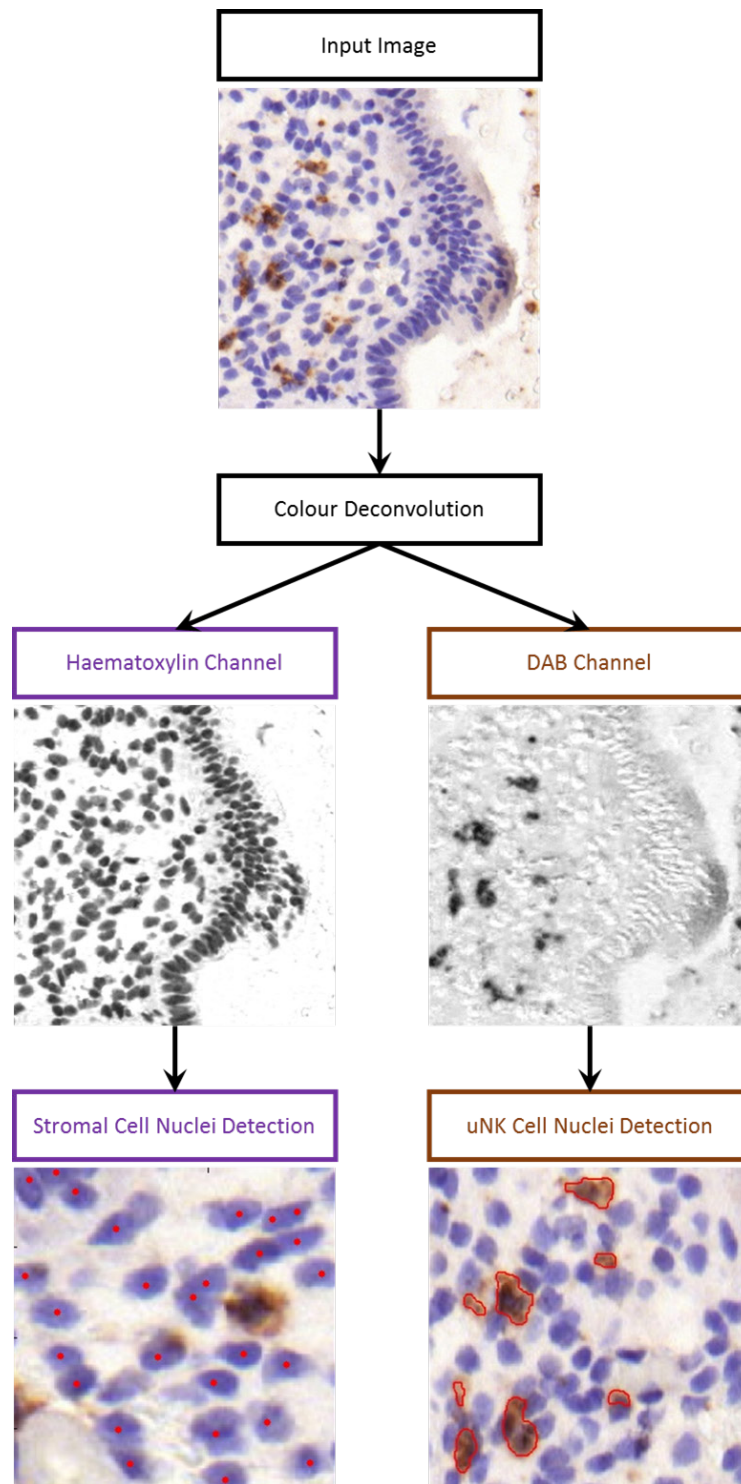
Figure 4.2: Workflow for detecting stromal cells and segmenting UNK cell nucleus (DAB stained brown) regions. Red dots indicate stromal cells and red circles mark the UNK cell nucleus regions.

4.3.1 Detection of Stromal Cell Nuclei

Stromal cell nuclei are detected using an improved version of the Local Isotropic Phase Symmetry Measure (LIPSyM) method [102]. The symmetry measure based on phase information was first introduced in [103], [104] and [105] have attempted to quantify symmetry based on the work presented in [103]. LIPSyM utilises the symmetry measure proposed in [103] to highlight points of interest (centers of cell nuclei in our case), which is based on the assumption that cell nuclei exhibit isotropic local symmetry, i.e., in all directions; and therefore, which are considered as elliptical blobs where the pixels near to the blob centre represent peaks of local isotropic phase symmetry.

The first step in LIPSyM is to discrete-time Fourier transform [106] the Haematoxylin channel image, followed by convolving the transformed image with a Gabor filter [107] at scale s and orientation o. The Gabor filters have a Gaussian transfer function when viewed on the logarithmic frequency scale, which is used to model simple cells in the visual cortex of mammalian brains [108] [109] [110]. The discrete-time Fourier transformed image I_H^f is then filtered by a bank of log-Gabor filters as,

$$V_{s,o} = I_H^f \star G_{s,o} \tag{4.1}$$

where $V_{s,o}$ denotes the convolution output of I_H^f and the log-Gabor $G_{s,o}$ at a scale s and an orientation o.

The median local response A_s of the log-Gabor filter $G_{s,o}$ in terms of amplitude all orientations at a scale s, is defined as,

$$A_s(x,y) = Median_{\{o=1,2,...,n_o\}}(|V_{s,o}(x,y)|) \tag{4.2}$$

where n_o denotes the total number of orientations, (x,y) denote the 2D coordinates of a pixel in $V_{s,o}$.

The median local response E_s of the log-Gabor filter $G_{s,o}$ in terms of energy for all orientations at a scale s, is defined as,

$$E_s(x,y) = Median_{\{o=1,2,\ldots,n_o\}}(|Real\{V_{s,o}(x,y)\}| - |Img\{V_{s,o}(x,y)\}|) \qquad (4.3)$$

where $Real\{\cdot\}$ and $Img\{\cdot\}$ denote the real and imaginary components of the log-Gabor filter response at pixel (x,y), respectively.

At a point showing high symmetry, the absolute value of real component of log-Gabor filter response will be large and the absolute value of imaginary component of log-Gabor filter response will be small. It is natural to quantify the symmetry measurement by subtracting the absolute value of imaginary component of log-Gabor filter response from the absolute value of imaginary component of log-Gabor filter response. This corresponds to the local response of log-Gabor filter in term of energy. To form the symmetry measurement over all scales, the sum of the median local response of log-Gabor filter in terms of energy for all orientations at each scale is normalised by the sum of the median local response of log-Gabor filter for all orientation in terms of amplitude at each scale. Thus, the local isotropic phase symmetry $\eta(x,y)$ at the pixel position (x,y) can be computed as,

$$\eta_{x,y} = \frac{\Sigma_{s=1}^{n_s} E_s(x,y)}{\Sigma_{s=1}^{n_s} A_s(x,y)} \qquad (4.4)$$

where n_s denotes the total number of scales. The peak $\eta x, y$ in a small local regions denote the center of a cell nucleus which are found using the h-maxima transform [111].

4.3.2 Resolving Redundant Detections of Stromal Cells

In practice, LIPSyM often finds multiple peaks for overlapping nuclei and for those with elongated shapes, resulting in redundant detections. LIPSyM attempts to construct the peaks s as a graph and using maximal cliques to partition the graph

66

into smaller subgraphs in order to merge redundant detections, the main problems are that graph clique on thousands of peaks are extremely computation intensive (it takes averagely 20 minutes on one image for our dataset), and adjacent peaks representing neighbouring nuclei are merged as one detection. The improved LIP-SyM solves the problems by using a probe (locality sensitive model) which searches for the boundaries between a nucleus and its neighbours in a boundary map, and merges them if there is no boundary can be detected. The boundary map B_{map} is a binary image that depict nucleus boundaries, which is segmented by using a series of intensity thresholding and edge enhancement techniques on the Haematoxylin channel I_H as follows:

1. An anisotropic diffusion filter [107] is applied on I_H to create image I_{ad}. This particular filter smoothens the interior of nuclei without significantly blurring their boundaries.

2. The gradient of I_{ad} is then computed to create a gradient image I_g.

3. Then I_g is filtered by the Difference of Gaussian (DoG) filters [112] [113] to enhance the nucleus edges as,

$$I_{dog} = I_g \star G_{(\sigma_1, w)} - I_g \star G_{(\sigma_2, w)} \tag{4.5}$$

where I_{dog} denote a DoG filtered image, the symbol $\star$ denotes the convolution operation, $G_{(\sigma_1, w)}$ and $G_{(\sigma_2, w)}$ are 2D Gaussian filters with standard deviation σ_1 and σ_2, respectively, which are calculated within a squared window of size $w = 7 \times 7$ pixel. The ratio of σ_1 and σ_2 is set to be $1 : 6$ [114].

4. Otsu thresholding [115] is applied on to obtain a binary image B.

5. Finally, small connected components, e.g., intensity peaks near the nucleus centres, are removed from B to obtain B_{map}.

It is important to note that the nucleus boundaries segmented by the above method are not always continuous or closed. Therefore, we use a probe to detect the nucleus boundary between two LIPSyM detections within an elliptical area, which is a type of locality sensitive modelling. It is designed to ensure that when there is no boundary can be segmented in some regions, but they does exists in fact, the boundary can be still correctly sensed. The model of the elliptical locality sensitive modelling is shown in Figure 4.3. The redundant LIPSyM detections is then merged as follows:

1. For a detection D_i that is not yet merged with any another detection, we find neighbouring detections in a predefined radius of 20 pixels, which roughly corresponds to the size of large and elongated nuclei.

2. Detection D_i is stored in a merging list and an elliptical probe between D_i and its jth neighbouring detection, D_i^j is constructed.

3. The probe searches for a boundary in B_map within the elliptical area. If no boundary is found, D_i^j is stored in the merging list and the algorithm proceeds to process D_i and D_i^{j+1}; if any boundary is found, the algorithm simply moves to process D_i and D_i^{j+1}.

4. All detections in the merging list are marked as merged and the centroid of their positions is calculated as the position of the new detection. The algorithm then proceeds to process D_{i+1}. A visual comparison of the original LIPSyM and the improved LIPSyM against the ground truth is shown in Figure 4.4. In fact, the automatic detection show more accurate results than manual marking of the experts.

4.3.3   Detection of UNK Cell Nuclei

Detection of UNK cell nuclei first requires segmenting those DAB stained brown regions which may contain a high density of UNK cell nuclei. We propose an adaptive
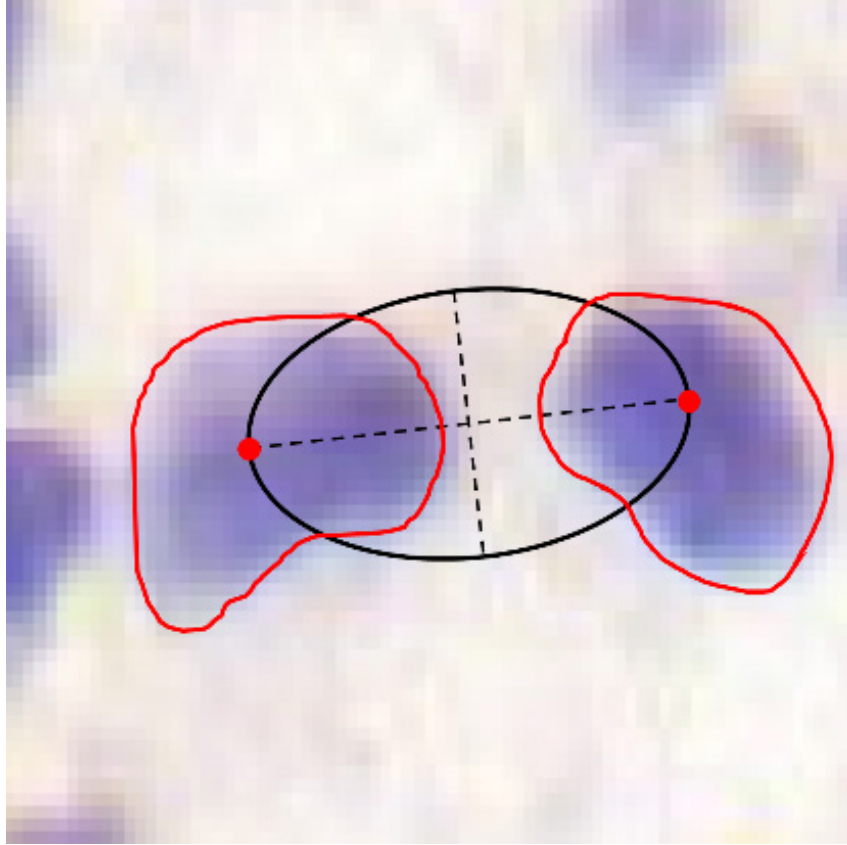
Figure 4.3: The model of the elliptical locality sensitive modelling. Red dots are LIPSyM detections, red solid lines denote the boundaries of nuclei, and the black ellipse marks the scope of the locality sensitive model, and two dashed straight lines are the minor and major axes of the probe, respectively.
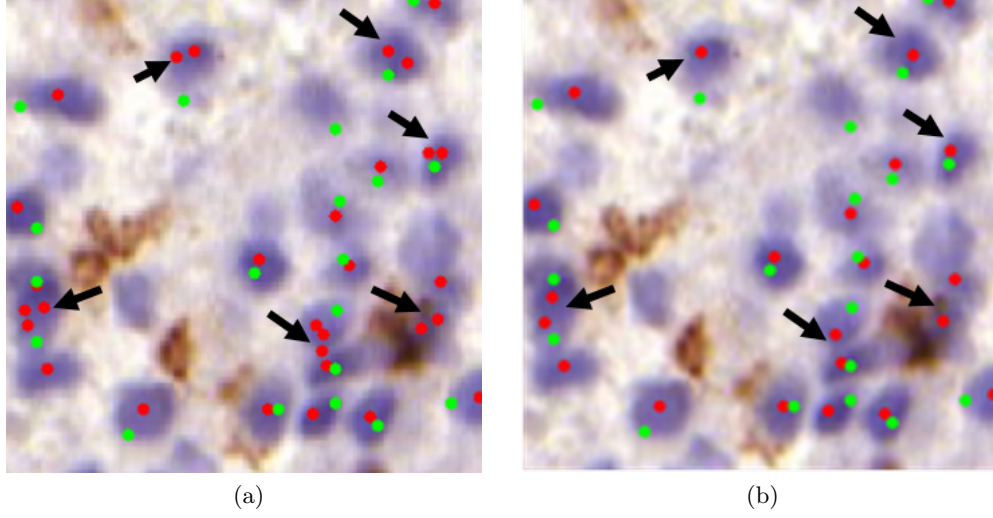
Figure 4.4: The detection results of (a) LIPSyM and (b) the improved LIPSyM. Green dots depict ground truth labelled by the experts for stromal cell nuclei, while red dots depict stromal cell nuclei detected by the algorithms. The differences between (a) and (b) are highlighted using black arrows.

background removal method to significantly ease the segmentation process. The proposed method uses the h-maxima transform on the DAB channel to suppress two types of high intensity regions, while keeping the lower intensity regions, which correspond to the UNK cell nucleus regions. The high intensity regions are the bright background and DAB stained brown regions, which are local minima lower than a height h. The output image of the h-maxima transform contains only the UNK cell nucleus regions over a very bright background. The h-maxima is transform performed as,

$$I_{hDAB} = R^{\delta}_{I_{DAB}}(I_{DAB} - h) \tag{4.6}$$

where $R^{\delta}_{I_{DAB}}(\cdot)$ denotes the morphological dilation operation using radius δ on the DAB channel I_{DAB}, h is the height parameter and I_{hDAB} denotes the resulting h-maxima transformed image. We calculate the value of parameter h as,

$$h = h_{I_{DAB}} - h_{UNK} \tag{4.7}$$

where h_{UNK} is the highest intensity of the UNK cell nucleus regions and $h_{I_{DAB}}$ is the highest intensity of I_{DAB}.

Although h_{UNK} may vary for different images, the proposed method can adaptively find h_{UNK}. It first computes the histogram of I_{DAB} and cluster the intensities into 3 bins (the bright background, the DAB stained background, and the UNK cell nucleus regions) using the k-mean ($k = 3$ in this case) clustering algorithm [116]. Next, h_{UNK} is setted to the upper bound of the lowest intensity bin which corresponds to the UNK cell nucleus regions. At last, The segmentation of UNK cell nucleus (DAB stained brown) regions is performed as follows:

1. Otsu thresholding is applied on I_{hDAB} to generate the binary image $B_{UNKpotential}$ that marks all potential UNK cell nucleus regions.

2. Morphological opening and closing operations [117] [118] are performed on $B_{UNKpotential}$ to remove small objects and merge broken cell nucleus regions, respectively. An 8-connectivity disk structuring element of size 5×5 pixel is used.

3. All regions of size smaller than the size of the smallest true UNK nucleus regions, i.e., 100 pixels in our case, are removed from the result of step 2 to obtain the final segmentation mask B_{UNK} for the UNK cell nuclei. The UNK cell nuclei detection result using the above method is shown in Figure 4.2.

For each detection, a locality sensitive model with the neighbourhood of 10×10 pixel is created around the detection. If any pixel within the locality sensitive model is a segmented as part of UNK cell nucleus regions, the detection is identified as an UNK cell nucleus.
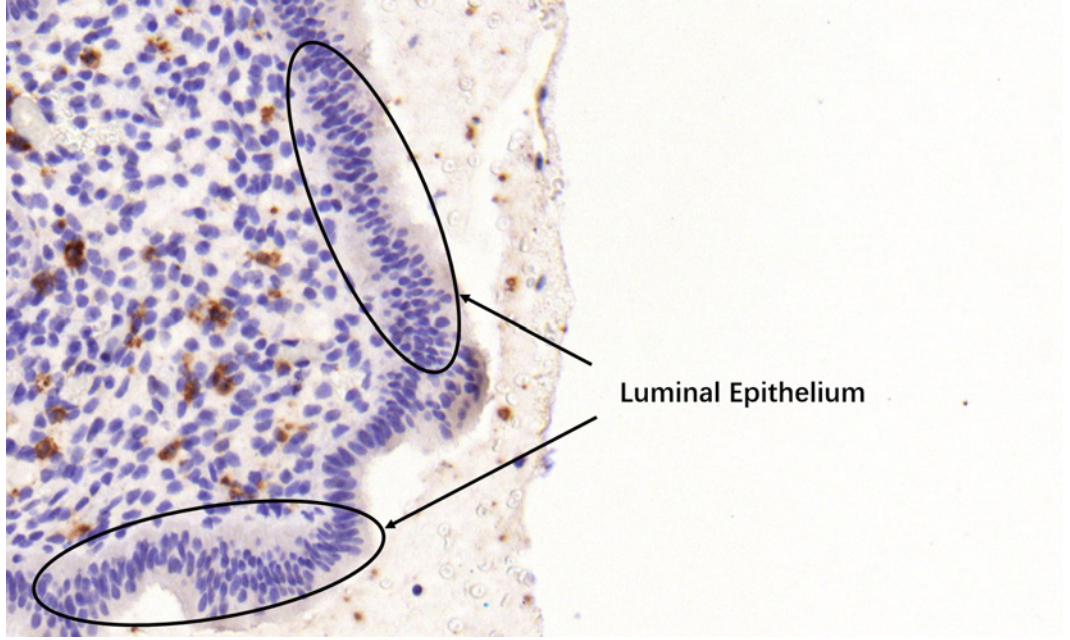
Figure 4.5: A sample image of luminal epithelium.

4.4 Localisation of the Luminal Epithelium Edge

Luminal epithelium edge is made up of layers of densely arranged epithelial cell nuclei, which forms the boundaries of tissue regions, an example of luminal epithelium is shown in Figure 4.5. Therefore, the epithelial cell nuclei can be used to localise the luminal epithelium edge. In this section, we propose a novel approach which is capable of identifying the LIPSyM detections corresponding to epithelial cell nuclei and utilising them to localise luminal epithelial edge. The proposed localisation method consists of three steps: 1) tissue region identification, 2) epithelial cell nuclei identification, and 3) luminal epithelium edge localisation.

4.4.1 Tissue Region Identification

We first identify the individual tissue regions where these edges are located. Then, the density-based spatial clustering of applications with noise (DBSCAN) algorithm [119] [56] is applied on a set of LIPSyM detections such that each resulting cluster represents a dense tissue region. Therefore, the proposed localisation method can

be performed separately on each tissue region to localise the corresponding luminal epithelium edge.

DBSCAN finds a number of clusters for a set of detections based on their density distribution; the number of clusters is automatically determined by the algorithm. DBSCAN starts from an arbitrary unprocessed detection D, it initialises a cluster from the detection D if a minimum number of its M neighbours within a search radius ϵ centred at the detection D can be retrieved. Otherwise, the detection D is labelled as an outlier. The algorithm expands the cluster by processing detections and adding their corresponding M-sized neighbourhoods until there is no more detections for which an M-sized neighbourhood can be found within the radius ϵ. Next, the algorithm moves to a new arbitrary unprocessed detection to repeat the above process to initialise either a new cluster or an outlier.

The accuracy of DBSCAN depends on two related parameters: the neighbourhood size M and the radius ϵ. We have found empirically that a value of M between 5 and 10 serves well for our application while a value of 50 for the radius ϵ corresponds to the average distance between two nuclei. In the experiment, we fix $M = 7$ and determine the radius ϵ as follows:

1. We define a Euclidean distance set $Dist$ as follow,

$$Dist = \{dist_1^{max}, dist_2^{max}, dist_i^{max}, ..., dist_N^{max}\} \tag{4.8}$$

   where $dist_i^{max}$ denotes the Euclidean distance between the ith detection D_i and the farthest neighbour of its M nearest neighbours, in terms of Euclidean distance, and N denotes the total number of detections in the set.

2. We divide the set $Dist$ into two clusters using the k-mean clustering algorithm and calculate the mean of each cluster. The minimum mean is used as the value of the radius ϵ.
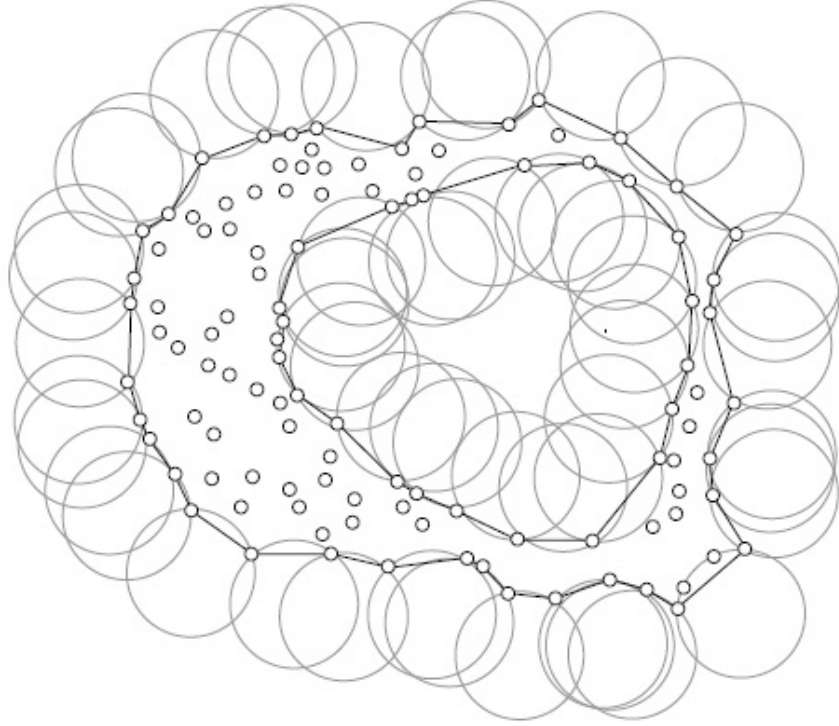
Figure 4.6: A 2D surface (the black edges between two points) constructed for a point cloud using the alpha shapes algorithm. Retrieved from [1].

4.4.2 Epithelial Cell Nuclei Identification

The luminal epithelium edge can be localised using the epithelial cell nuclei. We identify the epithelial cell nuclei from a cluster of improved LIPSyM detections. This cluster is treated as a point cloud in which each point represents an improved LIPSyM detection. The alpha shapes algorithm [120] is used to construct an outer 2D surface for this point cloud by connecting pairs of points that can be touched by the boundary of an empty disk with a radius α. Figure 4.6 shows a sample 2D surface constructed for a point cloud by the alpha shapes algorithm [1].

In general, the quality of the 2D surface constructed using the point cloud is very sensitive to the radius α. A large radius α results in a coarse surface since fewer number of points are connected, while a small radius often results in numerous incorrect surface fragments on the inside of the point cloud. An appropriate radius

α for a cluster of N LIPSyM detections is calculated as,

$$\alpha \geq \frac{\Sigma_{i=1}^{N}||D_i^{(x,y)} - D_{iNN}^{(x,y)}||}{2N} \qquad (4.9)$$

where $D_i^{(x,y)}$ denotes the 2D coordinates of the ith detection D_i in the cluster and $D_{iNN}^{(x,y)}$ denotes the 2D coordinates of the nearest neighbour of D_i in terms of Euclidean distance.

The points used for constructing the 2D surface from a point cloud using the alpha shapes comprise a set of boundary points. This set normally contains three types of LIPSyM detection, namely 1) epithelial cell nucleus, 2) stromal cell nucleus located very close to or on the image borders, and 3) stromal cell nucleus located far from the image borders. By removing $Type$-2 detections from the boundary point set, we can roughly consider the rest of the set as those detections corresponding to the epithelial cell nuclei. For those cases where the boundary point set also contains $Type$-3 detections, we use DBSCAN to remove them since they are normally located far from $Type$-1 detections in terms of Euclidean distance.

In some cases, the calculated radius α is large, which results in a portion of the detections corresponding to epithelial cell nuclei not being used for constructing the 2D surface. In these cases, we use a k-Nearest Neighbour (k-NN) search to retrieve some of the missing detections corresponding to epithelial cell nuclei, since the nearest neighbours of the obtained detections corresponding to epithelial cell nuclei are very likely to be the detections corresponding to epithelial cell nuclei either. In practice, we have empirically found that $k = 5$ is a suitable value for our application.

4.4.3 Luminal Epithelium Edge Localisation

Given a set of detections on epithelial cell nuclei, we can easily fit a curve on them to localise the luminal epithelium edge using a cubic B-Spline method. Since a single

Tissue Region Identification

LIPSyM detections belonging to a tissue region are depicted in green and the outliers are depicted in red.

Epithelial Cell Nuclei Identification

Construction of a 2D surface using alpha shapes

Identification of boundary points corresponding to epithelial cell nuclei

Retrieval of missing epithelial cell nuclei using k-NN search

Luminal Epithelium Edge Localisation

LIPSyM detections depicted in green, the boundary points in yellow, and the 2D surface in black.

Identified epithelial cell nuclei in magenta and the luminal epithelium edge is localised using the black curve.

Figure 4.7: Workflow of the proposed luminal epithelium localisation method and the intermediate results of each step.

cubic B-Spline curve describing the exact luminal epithelium is in general hard to localise, the detection set is broken into segments and a small cubic B-Spline curve is fitted separately on each segment using a third-degree polynomial with optimal coefficients [121], and all curves are finally connected together to from the localisation. The workflow of the proposed localisation method and the intermediate results of each step are shown in Figure 4.7. The final result of luminal epithelium edge localisation applied on a sample image is shown in Figure 4.8.

76
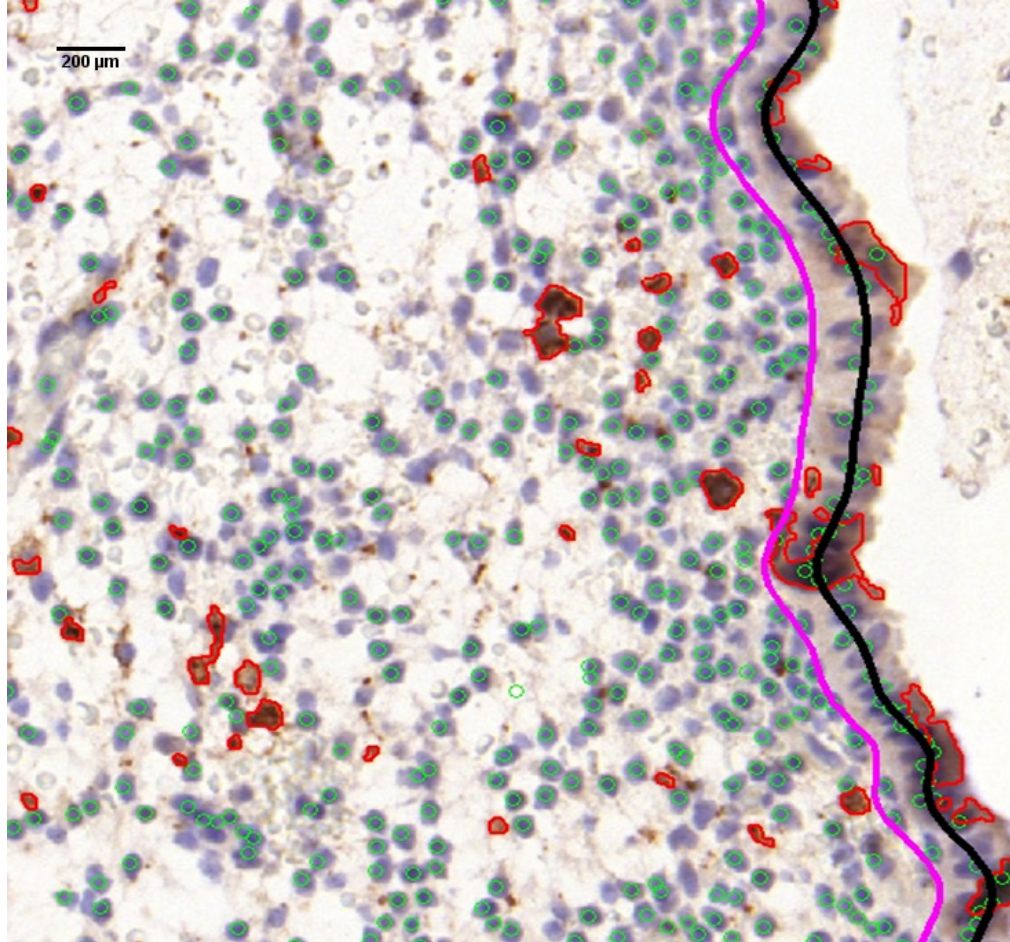
Figure 4.8: Final results of the stromal cell detection, UNK cell nucleus region segmentation, and luminal epithelium edge localisation on a sample image. Green circles indicate stromal cell nuclei; red areas are UNK cell nucleus regions; the black curve localises the luminal epithelium edge, and the magenta curve marks a distance (200μm) from the luminal epithelium edge, any cell nucleus located within this distance should not be counted.

4.5 Experimental Results

4.5.1 Evaluation of the Proposed Detection Methods

We evaluate the improved LIPSyM, the original LIPSyM, the proposed UNK cell nucleus detection method and a commercial software, VIS developed by Visiopharm [122], on 20 expert hand-marked images. VIS is a cloud application that can be used to segment various types of cell nucleus, glandular structure and epithelium in digital pathology images. The VIS system requires a training process using nucleus and background regions from the sample images. It was configured and trained by its owner company on 50 expert hand-marked images provided by our collaborators.

We quantify the detection accuracies of above methods and VIS in Precision and Recall values, and F_1 score which are calculated as follows,

$$
\begin{aligned}
Precision &= \frac{TP}{TP + FP} \\
Recall &= \frac{TP}{TP + FN} \\
F_1 &= 2 \cdot \frac{Precision \cdot Recall}{Precision + Recall}
\end{aligned}
\tag{4.10}
$$

where TP denotes a detection that can be matched to a hand-marked nucleus within a matching radius of 10 pixels (for stromal cell) and 30 pixels (for UNK cell); FP denotes a detections that cannot be matched to a hand-marked nucleus within the match radius; and FN denotes a cell nucleus which are not detected by the algorithm.Table 4.1 shows the averages of Precision and Recall values and F_1 score of the evaluated methods.

Figure 4.9 show the cell nucleus segmentation results of VIS on a local region of an input image. It is observed that most of the cell nuclei are segmented as connected regions. VIS claims that the number of cells is estimated based on dividing the total area (in pixel) of all segmented cell nucleus regions by an estimated average size (in pixel) of one individual cell nucleus. Consequently, VIS reports an estimated

Table 4.1: Quantitative comparison of the evaluated methods, which shows the averages of Precision and Recall values and F_1.

Methods	Precision	Recall	F1 Score
Improved LIPSyM (stromal cell nuclei)	0.86	0.83	0.84
Original LIPSyM (stromal cell nuclei)	0.79	0.83	0.81
VIS (stromal cell nuclei)	0.77	0.59	0.67
Proposed (UNK cell nuclei)	0.89	0.91	0.90
VIS (UNK cell nuclei)	0.65	0.93	0.77

cell counts rather than the exact cell population. In addition, the number of UNK cell can be hardly counted without knowing the exact number of the cells which are located within the DAB stained brown regions.

The original LIPSyM attains low Precision values due to a large number of redundant detections (FPs) produced in elongated stromal cell nuclei and overlapping nuclei (see Figure 4.10 (a)). As expected, the improved LIPSyM can significantly reduce the redundant detections (FPs) produced by the original LIPSyM using the elliptical probe (see Figure 4.10 (b)). In contrast, VIS often produces a number of incorrect detections (FPs) on non-stromal regions stained blue/purple, and therefore attaining low Precision values (see black circles in Figure 4.9 (b) and the ground truth in Figures 4.10 (a) and (b)). Moreover, VIS produces an unacceptable Recall value due to massive FNs in under-segmented areas. The under segmentation problem of VIS frequently happens in the dense nucleus clusters, i.e., multiple close or overlapped stromal cell nuclei are segmented as one single connected region (see Figure 4.9 (b)), which results in a number of stromal cell nuclei
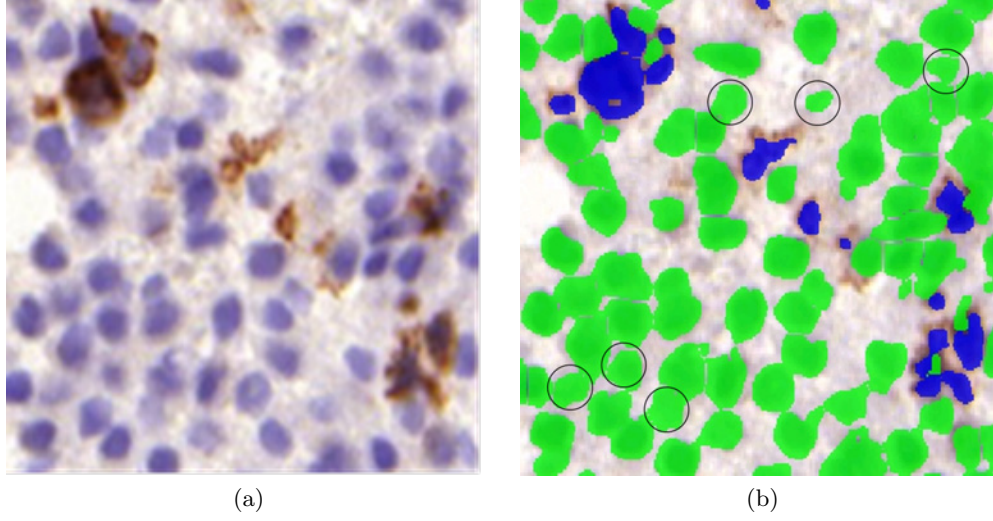
Figure 4.9: (a) A cropped local region of an input image and (b) the stromal cell nuclei and UNK cell nucleus regions segmented by VIS. In (b), stromal cell nuclei segmented by VIS are shown in green and we mark the incorrectly segmented stromal regions by VIS in black circles.

are miss segmented/detected.

The experimental result shows that both Precision and Recall values of our method are higher than VIS. The Recall value is, however, slightly lower due to a number of FNs caused by the under segmentation of UNK cell nucleus regions. Figure 4.11 (a) shows the Ground Truth of UNK cell nuclei and the segmentation result produced by the proposed method. On the other hand, VIS attains higher a Recall value, however, its Precision value is much lower than that of the proposed method due to the over segmentation of UNK cell nucleus regions and a number of incorrect segmentation on non-UNK cell nucleus regions stained brown (artefacts). Figure 4.11 (b) shows the segmentation results of VIS. The result produced by the proposed methods are validated by two expert pathologists from the UHCW hospital, and they have confirmed that the result is satisfactory to clinical practice.

(a)	(b)
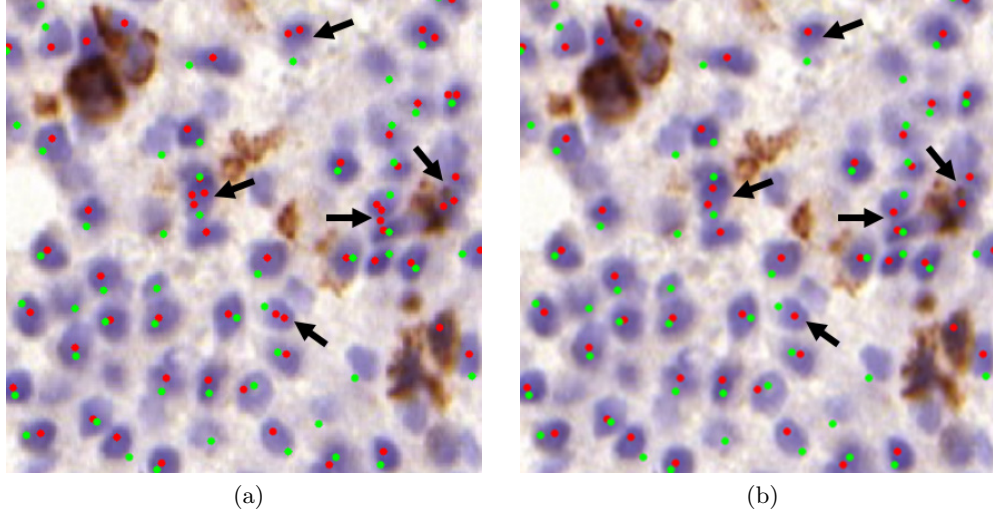
Figure 4.10: (a) Detection result of the original LIPSyM and (b) that of the improved LIPSyM for the same cropped region shown in 4.9. Red dots depict stromal cell nuclei detected by the algorithm and green dots depict manually marked stromal cell nuclei. The differences between (a) and (b) are highlighted using black arrows.

4.5.2 Evaluation of the Proposed Localisation Method

We use 10 hand-marked images in the evaluation of the proposed localisation method. We are unable to numerically quantify the localisation results produced by VIS, since it does not provide a functionality to output their results of luminal epithelium edge segmentation, however the results of the proposed method and VIS are visually comparable (see Figure 4.12).

We align the curve $\hat{C}$ approximated by the proposed localisation method and a hand-marked (Ground Truth) curve C_{GT} along the x axis (horizontally). To numerically quantify the accuracy of the proposed localisation method, Root Mean Square Error (RMSE) of the Euclidean distance in between the pixel locations of curves $\hat{C}$ and C_{GT} in the y axis (vertically) calculated as follows,

$$RSME = \sqrt{\frac{1}{N} \sum_{i=1}^{N} (\hat{y} - y)^2} \tag{4.11}$$
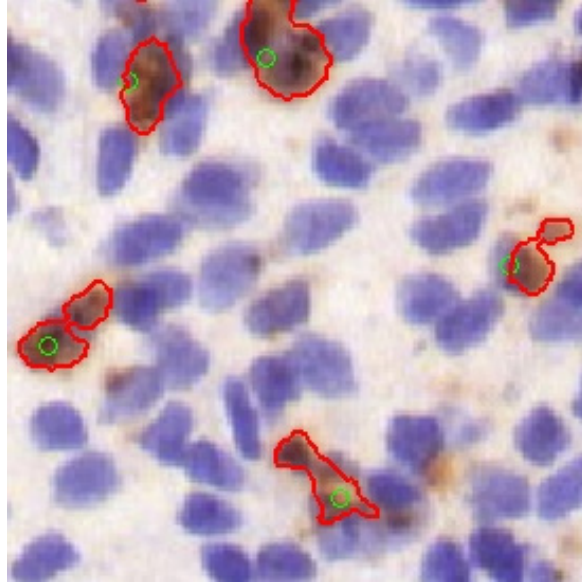
(a)
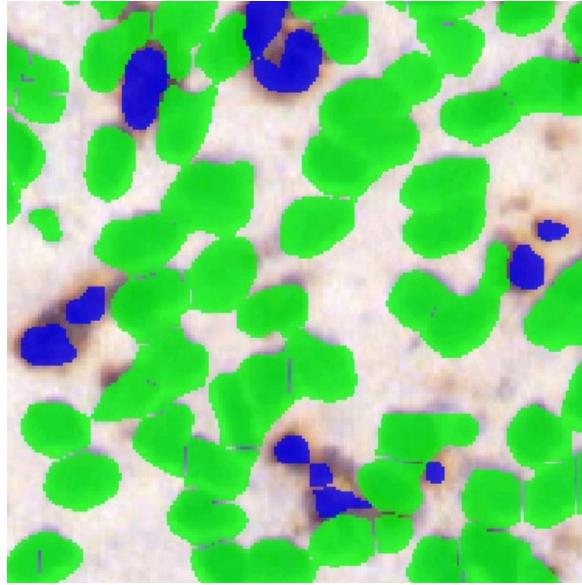
(b)

Figure 4.11: (a) Another cropped local region of the same input image showing in green Ground Truth of UNK cell nuclei, and in red the UNK cell nucleus regions detected by the proposed method. (b) The UNK cell nucleus regions (in blue) and the stromal cell nucleus regions (in green) segmented by VIS in the cropped local region of (a); note the over-segmentation of UNK cells.

where $\hat{y}_i$ is the y coordinate of the ith pixel of curve $\hat{C}$, y_i is the y coordinate of the ith pixel of curve C_{GT} and N is the total number of pixels in the curve C_{GT}.

For the proposed localisation method, the curve describing the location of the luminal epithelium edge is approximated using 20 smaller B-Spline curves. The average RMSE of curve $\hat{C}$ for the 10 ground truth images is 23.17 pixels (10.77μm) which can also be thought of as the average Euclidean distance between the pixel locations of curves $\hat{C}$ and C_{GT}. The visual results produced by the proposed localisation method and VIS on three sample images are shown from Figures 4.12 to 4.14.

VIS uses a segmentation based approach to mark luminal epithelium edges. Figure 4.12 shows an example of a good segmentation result produced by VIS, however, it fails to correctly segment luminal epithelium edges in a dense nuclei environment, e.g., in Figure 4.13 (b), where many nuclei in the interior area of the tissue region are being segmented as luminal epithelium edge. In contrast, the proposed localisation method still performs well in such cases (see Figure 4.13 (a)). Moreover, VIS sometimes is unable to segment a whole luminal epithelium edge, e.g., the left part of the luminal epithelium edge in Figure 4.14 (b), while the proposed localisation method is able to detect complete luminal epithelium edge (see Figure 4.14 (a).

It is also worth noting here that the proposed localisation method is much faster, in terms of running time, compared with VIS. The proposed localisation method (currently written in MATLAB) takes on average a few minutes (on an Intel i5 processer with 8G RAM) to process an image of the resolution of $1,000 \times 1,500$ pixels, while VIS takes at least 6 minutes even using cloud computing. The computational speed of the proposed localisation algorithms can be significantly improved by optimising the code in C/C++ and running on a high-end computer.
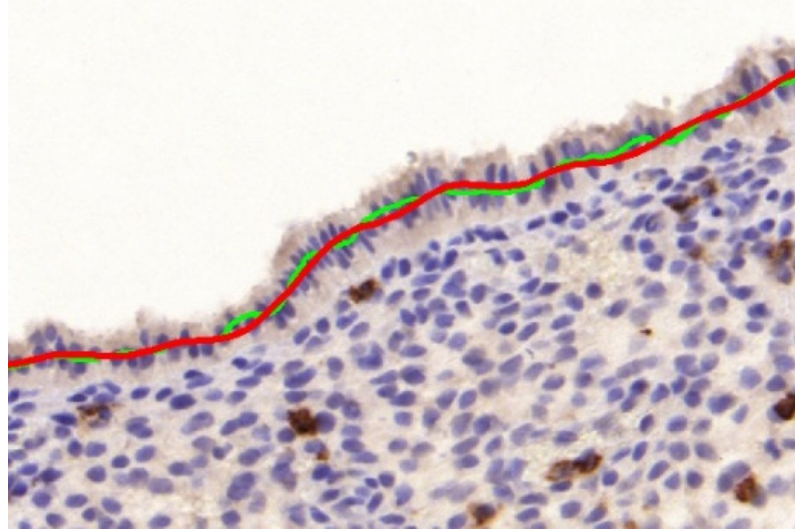
(a)
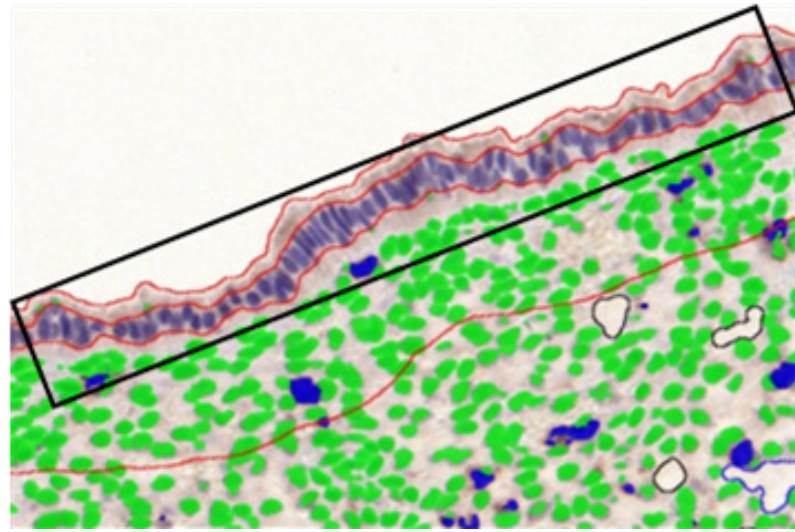
(b)

Figure 4.12: (a) shows the luminal epithelium localisation produced by the proposed method and (b) shows the luminal epithelium segmentation produced by VIS on same input images. In (a), Ground Truth of the luminal epithelium edges is depicted in green, and the luminal epithelium edge detected by the proposed method is depicted in red. In (b), the luminal epithelium segmentation produced by VIS is marked by a black bounding box.
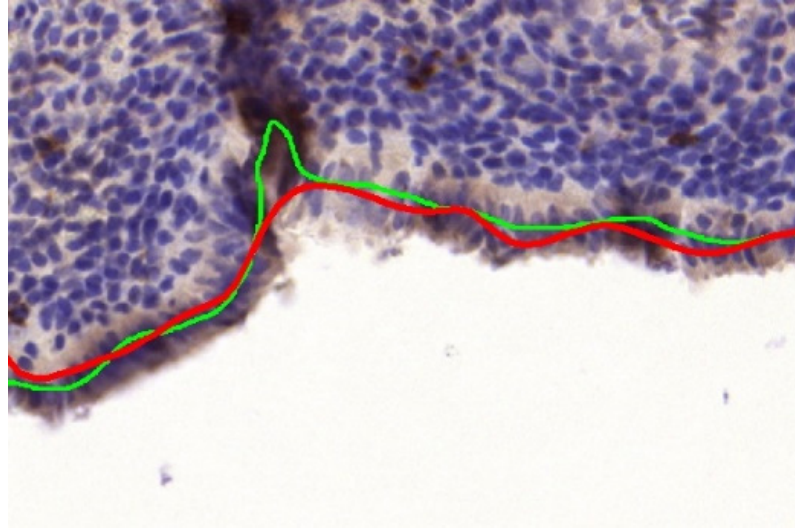
(a)
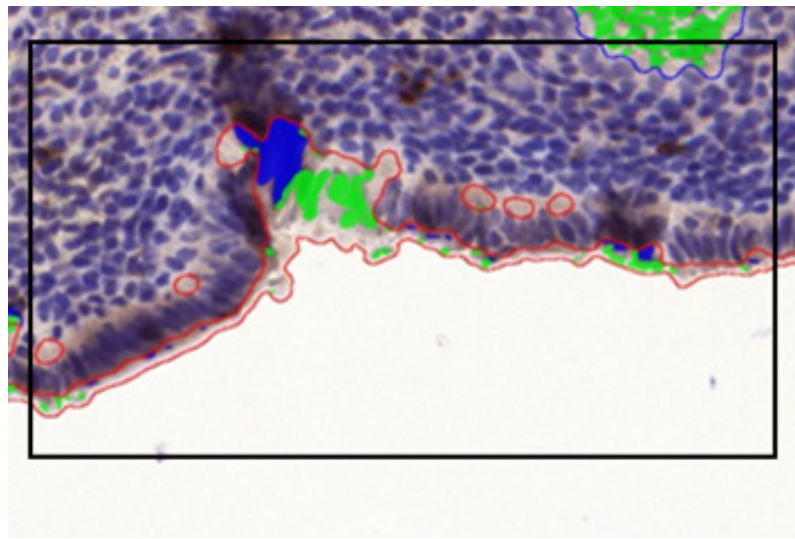
(b)

Figure 4.13: (a) shows the luminal epithelium localisation produced by the proposed method and (b) shows the luminal epithelium segmentation produced by VIS on same input images. In (a), Ground Truth of the luminal epithelium edges is depicted in green, and the luminal epithelium edge detected by the proposed method is depicted in red. In (b), the luminal epithelium segmentation produced by VIS is marked by a black bounding box.
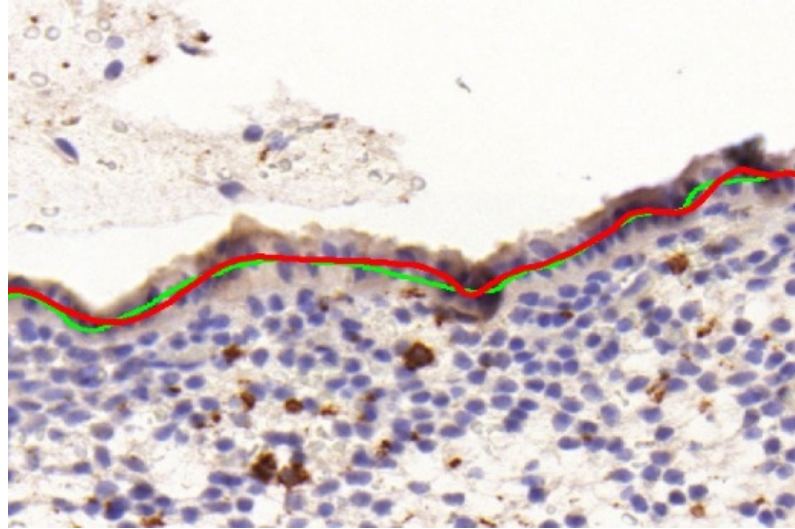
(a)
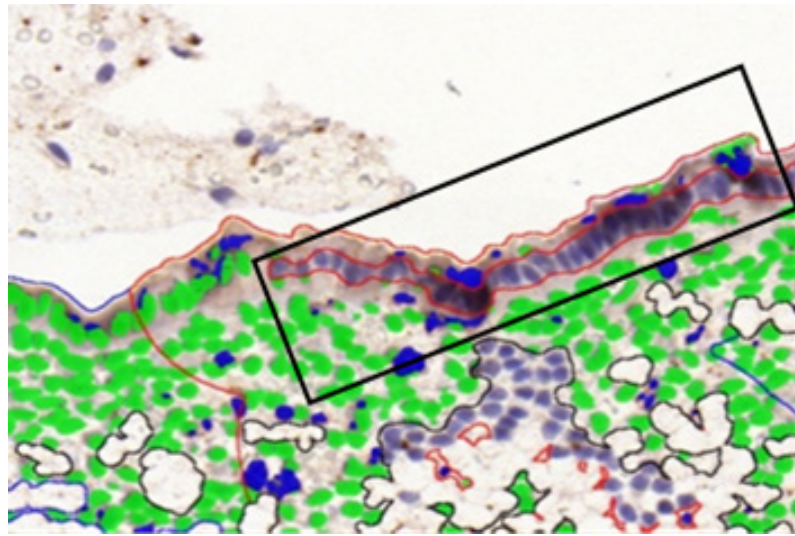
(b)

Figure 4.14: (a) shows the luminal epithelium localisation produced by the proposed method and (b) shows the luminal epithelium segmentation produced by VIS on same input images. In (a), Ground Truth of the luminal epithelium edges is depicted in green, and the luminal epithelium edge detected by the proposed method is depicted in red. In (b), the luminal epithelium segmentation produced by VIS is marked by a black bounding box.

4.6 Summary

In this chapter, we proposed a complete solution to effectively detect stromal and UNK cell nuclei and localising luminal epithelium edge in endometrial histology images. A locality sensitive model is integrated into a cell detection method called LIPSyM, which greatly improved its performance in our cases. In addition, a novel background removal method was proposed for segmenting DAB stained brown regions (indicated the UNK cell nucleus regions). We also proposed a novel luminal epithelium localisation method, which can localise the luminal epithelium edges by fitting cubic B-spline curves on the epithelial cell nucleus detections identified using an alpha-shape based method. The experimental results show that the proposed solution attains a high accuracy (F_1 score: 0.84) on processing the high resolution ($1,000 \times 1,500$ pixel) local regions from the HPFs of whole slide endometrial histology images. The results produced by the proposed solution were validated and approved by the collaborators.

Chapter 5

Segmentation of Epithelium in Endometrial Tissue

Segmentation of epithelium in histology images is a challenging task due to the appearance of epithelial cell often being similar to that of stromal cell, particularly in the endometrial tissue. In the second stage of the work regarding to counting UNK cell ratio, we are challenged by segmenting both luminal and glandular epithelium in the endometrial histology image datasets. In this chapter, we utilise the fact that neighbouring epithelial cells exhibit certain orientation patterns, in terms of their orientations, to propose a variety of novel cell orientation congruence descriptors which and attempt to statistically and quantitatively compute the orientation patterns, to simultaneously segment both luminal and glandular epithelium.

An overview of the proposed epithelial segmentation method is demonstrated in Figure 5.1. First, a pre-processing step first detects cells and segments lumen/background regions to locate the superpixels corresponding to potential epithelium. Next, the proposed descriptors for each cell located within the epithelial superpixels is computed. Then, the cells are labelled as either epithelial cells or stromal cells by using a Random Forest classification algorithm together with the proposed descriptors. Finally, the epithelial superpixels containing the classified

epithelial cells are connected to yield the epithelium segmentation.

Image acquisition and the dataset are already described in previous chapter. The reminder of this chapter is organised as follows. In Section 5.1, we discuss several state-of-the-art segmentation/classification methods for glandular structure/epithelium. Section 5.2 introduce the pre-processing steps, i.e., cell detection and lumen segmentation, pixel and cell orientation estimation, which are prerequisite for computing the proposed descriptors and epithelial cell classification. Section 5.3 present that how to compute the proposed descriptors in details, and how to use the epithelial cells classified by the proposed descriptors together with superpixels to achieve the epithelium segmentation. In Section 5.4, we evaluate the proposed epithelium segmentation method different cell orientation congruence against 5 state-of-the-art gland segmentation methods. Section 5.4.4 highlights the benefits and advantages of the proposed epithelium segmentation method compares with other related works done in this area, and extends the observations and contributions to other areas of application, e.g., cancer research. In addition, this section also discusses the issues such as full automation in pathology, practical, ethical and legal problems of adopting the automation using the proposed image analysis methods in pathology and clinical diagnosis. Finally, we conclude the work of this chapter in Section 5.5.

5.1 Related Work

To the best of our knowledge, there is rarely an existing method proposed in general for segmenting epithelium. However, the glandular epithelium can be extracted from the corresponding glandular structures in most cases, thus the state-of-the-art gland segmentation methods can be used to segment the glandular epithelium in endometrial histology. In this section, we then review several state-of-the-art gland segmentation methods to discuss their current gaps in segmenting the glandular

89
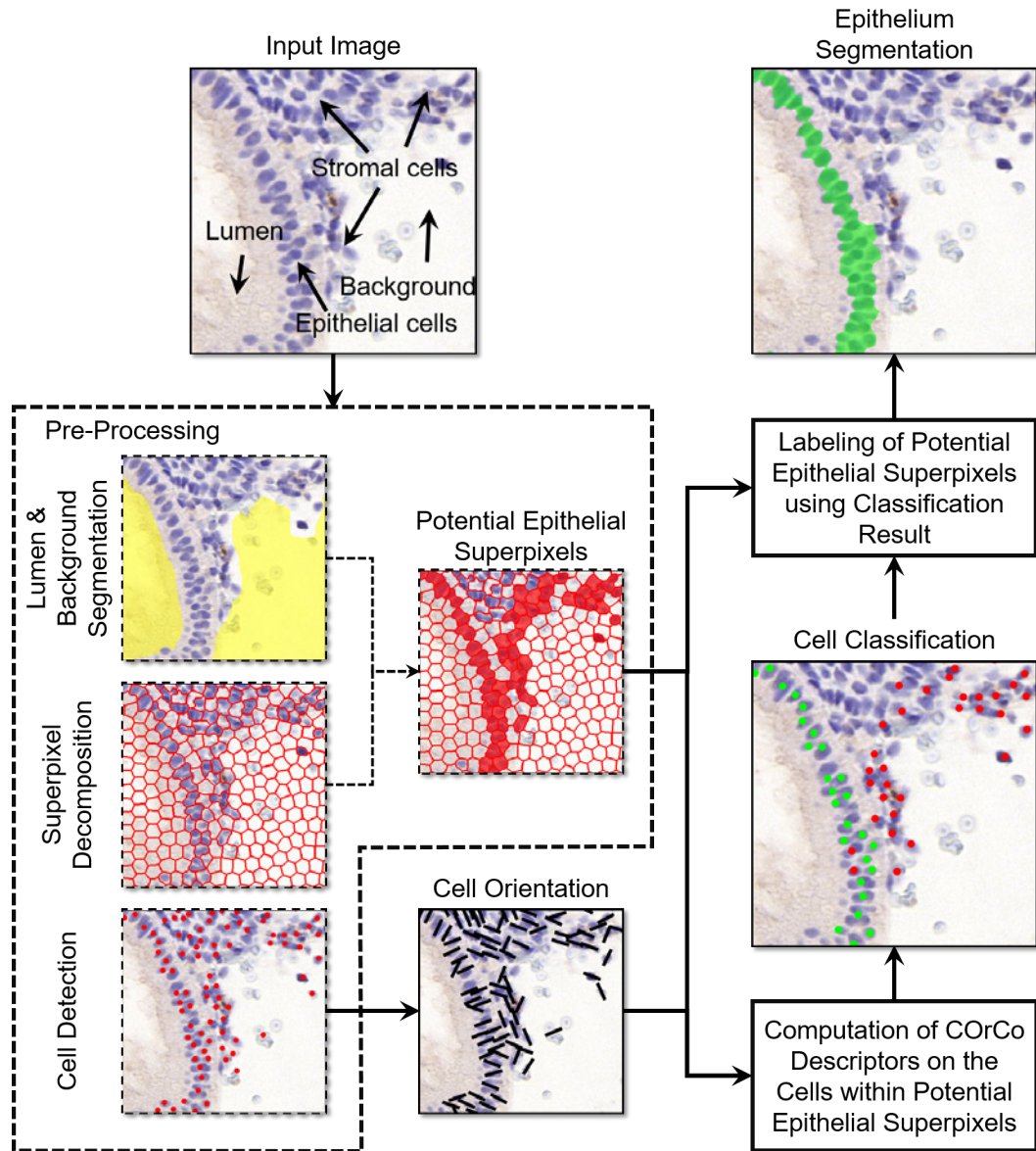
Figure 5.1: A block digram of the proposed method with intermediate result of each step. Red dots depict detected cells, black bars represent cell orientation, lumen segmentation is shown in transparent yellow, red grid marks superpixels, potential epithelial superpixels are shown in transparent red, green dots depict epithelial cells classified by the proposed descriptors, and epithelial segmentation is shown in green.

structures in endometiral histology.

Many of the state-of-the-art gland segmentation methods are generally developed for the histology images of cancers, and commonly proposed based on utilising two types of obvious feature/information regrading to the biological objects: 1) texture/shape/colour of cell nucleus, cytoplasm, lumen and background, and 2) information regarding to the structure of gland. Although glands often exhibit a varsity of largely varied irregular shapes, lumen is always the region in the centre of a gland, which can be considered as the most common component of different glands. Therefore, most of the previous work focused on detecting lumen to begin with tackling the gland segmentation problems. The previous methods assume that lumen can be identified using their colour [123] [124] or texture [125] [126]. Once the lumen areas are detected, it can be considered as the seed regions, so that the segmentation methods based on, such as region growing [127], active contour [128], level-set [129], etc., can be adopted to segment out the glandular structures.

For instance, Naik *et al.* [123] proposed a solution of automated detection and segmentation for nuclear and glandular structures in prostate and breast cancer histology. The information regarding to the histological structures is critical for classification and grading of prostate and breast cancer. The solution is developed using both colour and structural features of object of interest, which integrates image information from three different scenes: 1) low-level information regarding to colour values of pixels, 2) high-level information regarding to relationships between pixels of objects of interest, and 3) domain-specific information regarding to relationships between histological structures. First, low-level information is utilised by a Bayesian classifier to generate a likelihood maps in where the value of each pixel represents a probability of that the pixel belongs to glandular structures or other objects. Second, high-level information generated in such ways: a level-set algorithm is used to initialise and evolve active contours in the likelihood maps to identify the boundaries of glandular structures. Finally, structural constraints regrading to

glandular structures are obtained via domain-specific knowledge, i.e. three main components constitute glandular structures: lumen, cytoplasm, and nuclei, which are arranged in a specific fashion (lumen is surrounded by cytoplasm, which is then surrounded by a ring of nuclei), and then they are used together with high-level information to verify whether the detected objects do indeed belong to the glandular structures.The major problem of this solution in endometrial histology is that the Bayesian classifier cannot accurately classify between lumen and background due to their colour similarity, which will cause the level-set algorithm initialise contours using wrong seed regions. In addition, the level-set contours have difficulty in approximating the epithelial boundaries with complex shape and texture.

Nguyen *et al.* [124] proposed a gland segmentation and classification scheme applied to histology image of prostate tissue. First, nucleus, cytoplasm and lumen objects are labelled using colour space analysis. Next, it utilises the information regarding to the constitution of the glandular components, to associate each lumen object with the corresponding nucleus objects, to create a gland segment. However, the scheme uses colour feature for detecting and classifying object of interest, which is only workable in the cases of that glandular components have a distinct colour difference compared with the other objects, and unfortunately inapplicable for our cases.

Farjam *et al.* [126] proposed an image analysis approach for determining malignancy of prostate pathological samples, which is important for treatment planning of prostate cancer. A texture-based technique is used to segment the prostate glands in the image: they first proposed a Variance filter to compute the textural features of cell, lumen and background regions; then used the K-means clustering algorithm [130] on the feature spaces to identify the different regions; finally, the glandular structures can be obtained after removing all non-glandular components from the identified regions. This method can be also used to segment lumen or background regions in endometrial histology, and consequently the segmentation result assists

in locating the glandular structures. However, it is not able to differentiate between the different cell types in endometrial histology. It is due to that, in terms of the textural feature computed using the Variance filter, the same type of cell regions show no texture consistency, but epithelial cell region may exhibits the similar textures as that of stromal cell region, and also there is no obvious difference between lumen and background regions.

Demir *et al.* [131] reported a new approach for gland segmentation in histology images of colon tissue. This approach decomposes the input image into a set of primitive objects (nucleus and lumen objects), and then makes use of their organizational properties, instead of the pixel information such as their colour or texture, to identify what kind of glandular component the primitive objects belong to, respectively. Then the epithelial cell object surrounding a lumen can be used to create the boundary of a glandular structure. One common major limitation of the methods using structural information regarding to glands is that the comprehensive prior knowledge of the glandular structures are essentially demanded in these methods, but it is quite impossible to be obtained in the cases of endometrial histology.

Sirinukunwattana *et al.* [132] presented a stochastic polygons model for segmenting glandular structures in histology images of colon tissue. The proposed model uses a set of nuclei near the identified lumen regions as the polygon vertices, and then attends to fit a polygon using the vertices to approximate the boundary of a glandular structures. The main issue of this approach is the costs of geometrically increased computational complexity with the increment of polygon vertices (nuclei), this is especially fatal for endometrial histology since the boundaries of many glands are formed by a significant number of epithelial cells. In addition, large background regions can be identified as lumen region, which causes the stromal cell nuclei near those region are treated as pylon vertices.

Fu *et al.* [133] devised an algorithm of detecting glandular structures in mi-

croscopic images of human colon tissue. The algorithm first converts the local image of a single gland from the polar coordinate system to the Cartesian coordinate system, resulting in an enclosed glandular boundary being transformed into a stretched curve. The curves in the transformed image, representing glandular boundaries, are then inferred through a conditional random field model. Finally, a visual feature based support vector regressor is used to verify if an inferred cure belong to a true glandular structures. The experimental results showed that the algorithm performed well on the histology images of adenomas and moderately differentiated adenocarcinomas. The main challenge for this methods in endometrial histology is that the epithelium are often not closed boundary, especially the luminal epithelium.

In endometrial histology, both luminal and glandular epithelium are characterized with strong inhomogeneity, e.g., they are normally shown as discontinued crust and are formed by multiple layers of epithelial cells. Lee *et al.* [134] proposed a Cell Orientation Entropy (COrE) method which attempts to first qualitatively model cell/nucleus orientations by performing PCA on the cells/nuclei boundaries segmented using active contour, and then it quantifies the cell disorders by calculating the second order statistics for cell orientation from a co-occurrence matrix. This method can be potentially used for distinguishing differences between the orientations of neighbouring epithelial and stromal cells/nuclei.

The high similarities, in terms of colour and morphology, between epithelial cells and stromal cells, and also between lumen and background regions, are obviously observed in endometrial histology. Consequently, the existing methods discussed above can hardly detect/segment/classify epithelial cells, which consequently causes the subsequent gland segmentation step to produce false results. We observe that epithelial cells are normally arranged in a locally and neatly oriented manner. Therefore, we propose a variety of novel descriptors, which is used to numerically expressing the orientation congruence of a local cell neighbourhood to classify between epithelial and stromal cells. The proposed epithelium segmentation

94

method are designated to overcome the limitations of the existing methods. For instance, the proposed methods are not restricted in segmenting glandular epithelium from glands with enclosed boundaries, but also capable of accurately segmenting disconnected (broken or open) epithelium from tissue boundary and background regions. More importantly, that the proposed method is capable of simultaneously segmenting both luminal and glandular epithelium.

5.2 Pre-processing

Given an input image, it is first separated into the two underlying stain channels, Haematoxylin and DAB (CD56), using a colour deconvolution method proposed in [135]. The Haematoxylin channel is used for cell detection, lumen segmentation, and superpixel decomposition. It is important to mention that localising cell nuclei is prerequisite to the computation of cell orientation congruence descriptors, but cell segmentation is not necessary for the computation. We localise the cell nuclei in Haematoxylin channel by using the extended version of Local Isotropic Phase Symmetry Measure (LIPSyM) method, which has been proposed in Chapter 4. We then segment lumen and background in the input image using a Variance filter proposed in [126]. It is based on the observation that lumen or background are large homogeneous regions with small textural variance, whereas the textures of dense cell clusters are strongly inhomogeneous.

We denote the pixel sets that are segmented as lumen or background as Seg_{lb}, they will be used together with superpixels to locate *potential* epithelial regions. We decompose the input image into superpixels using the Simple Linear Iterative Clustering (SLIC) algorithm proposed in [136]. A superpixel is a set of pixels, which compose a small homogeneous region depicting either lumen, background or cell in our cases. The superpixels are classified into two categories: lumen and cell. We define a superpixel S as a lumen superpixel S_l if $|Seg_{lb} \cap S| \geq \frac{1}{2}|S|$, which depicts a

lumen region; otherwise it is defined as a cell superpixel S_c, which depicts either an epithelial or a stromal cell region.

The cell regions near lumen/background boundaries can be potentially labelled as epithelial cell regions. We define a cell superpixel S_c as a 1st level *potential* epithelial superpixel S_e^1 if it is immediately adjacent to any lumen superpixel S_l. The epithelium in our cases is normally formed by multiple layers of epithelial cells. Therefore, we also include the cell superpixels which are not directly adjacent but close to lumen regions as *potential* epithelial superpixels as follows: a cell superpixel S_c is defined as a 2nd level *potential* epithelial superpixel S_e^2, if it is not yet defined as a 1st level *potential* epithelial superpixel and also immediately connects to any 1st level *potential* epithelial superpixel S_e^1. We then merge all 1st and 2nd level *potential* epithelial superpixels together to yield the *potential* epithelium region segmentation.

5.2.1 Estimation of Pixel and Cell Orientations

In this step, the Haematoxylin channel is normalised to zero mean and unit variance. The normalisation is to enhance the image contrast and reduce the variations in the pixel values of cell and background regions from different images, which facilitates the subsequent image processing steps. The normalization process is defined as,

$$N(i,j) = \frac{I(i,j) - M}{V} \tag{5.1}$$

where $I(i,j)$ denotes the gray-level value at pixel $I(i,j)$ of the input image, M is the estimated mean pixel value of the input image and V is the estimated standard derivation of the pixel values of the input image, and $N(i,j)$ denotes the gray-level value at pixel (i,j) of the normalised image.

We first calculate the gradient images G_x and G_y of the normalised image in both x and y directions, and estimate the pixel orientation of the input image using

96

G_x and G_y as follows,

$$G_{xy}(i,j) = (G_x * G_y \star f)(i,j)$$

$$G_{xx}(i,j) = (G_x^2 \star f)(i,j)$$

$$G_{yy}(i,j) = (G_y^2 \star f)(i,j) \qquad (5.2)$$

$$O_p(i,j) = \frac{\pi}{2} - \arctan\left(\frac{G_{xy}(i,j)}{G_{xx}(i,j) - G_{yy}(i,j)}\right)$$

where f is a 2D Gaussian filter of window size w and standard deviation σ, $*$ denotes the image multiplication operation, $\star$ denotes the image convolution operation, and $O_p(i,j)$ denotes the pixel-level orientation at pixel (i,j) of the input image.

We next define a circular pixel neighbourhood $\mathcal{N}(c)$ of the cell c defined as,

$$\mathcal{N}(c) = \left\{p \in Mask^h | dist(c,p) \leq r\right\} \qquad (5.3)$$

where p is a pixel from the input image, $Mask^h$ is a binary mask image segmented from the Haematoxylin channel using Otsu Thresholding [115], $dist(c,p)$ is Euclidean distance between p and the centre of c, and r is a scalar in pixel value which defines the radius of $\mathcal{N}(c)$. In our cases, r is set to 7 pixels, which was empirically tuned to roughly cover a cell nucleus. Figure 5.2 shows an example of the circular pixel neighbourhood.

We then define the pixel orientation histogram $\mathcal{H}(c)$ of $\mathcal{N}(c)$ as,

$$\mathcal{H}(c) = \left\{h_1, h_2, ..., h_7\right\} \qquad (5.4)$$

where the orientations of the pixels in $\mathcal{N}(c)$ are clustered into 7 bins. The count h_k of the pixel orientations in the kth bin is calculated as follows,

$$h_k = \sum_{p=1}^{|\mathcal{N}(c)|} 1(O_p^c, k), \ k = 1, 2, ..., 7 \qquad (5.5)$$
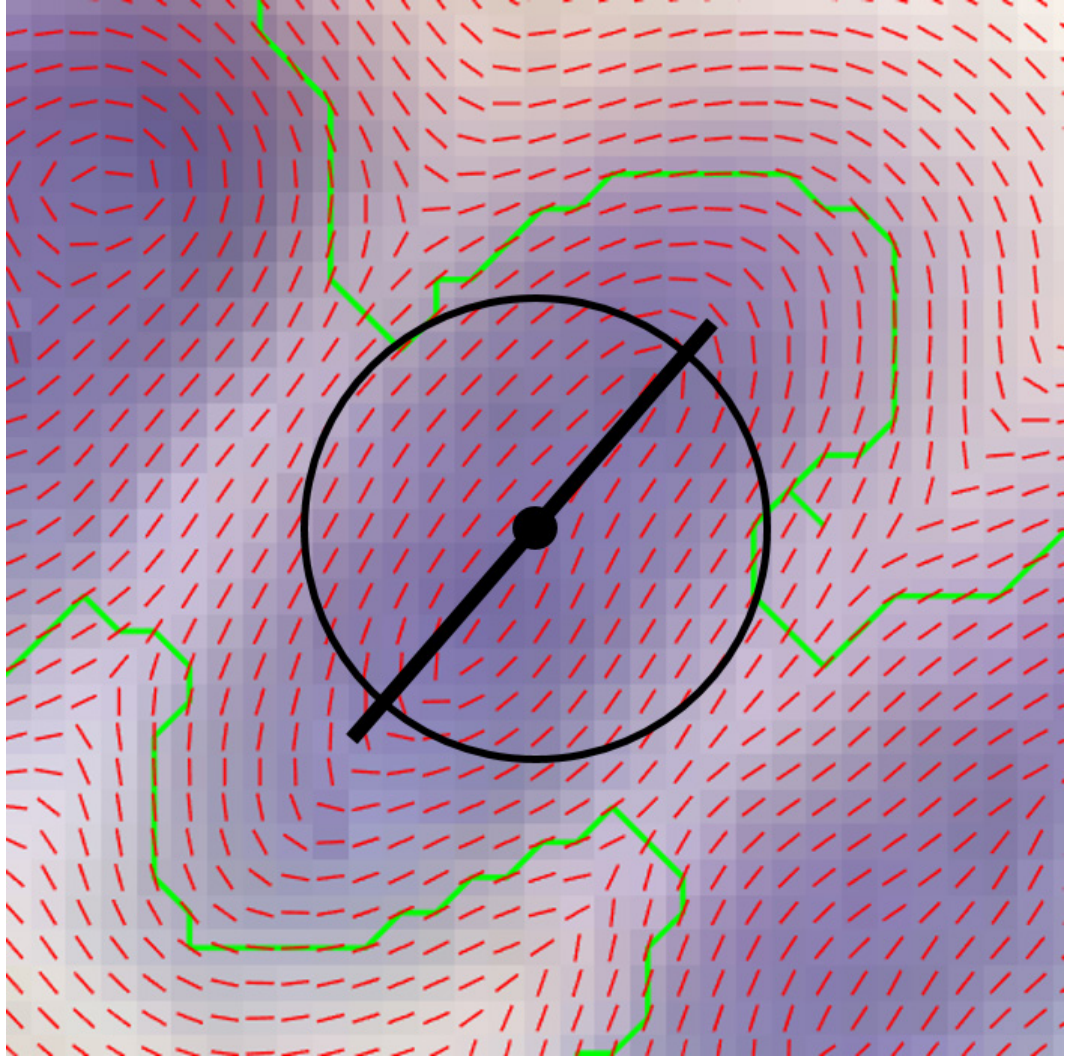
Figure 5.2: Black circle marks the circular pixel neighbourhood, cell nucleus segmentation is shown in green, red bars depict the estimated pixel orientations, black dot depicts a detected cell, and black bar depicts the estimated cell orientation.

where

$$1(O_p^c, k) = \begin{cases} 1, & if \ \frac{(k-1)\pi}{8} \leq O_p^c < \frac{(k+1)\pi}{8} \\ 0, & otherwise \end{cases}$$

In the above equations, $1(O_p^c, k)$ is an indicator function that indicates which bin the orientation O_p^c of a pixel p in $\mathcal{N}(c)$ belongs to. The cell orientation O_c of the cell c is estimated as follows based on the largest bin of $\mathcal{H}(c)$,

$$O_c = \frac{1}{h_{max}} \sum_{p=1}^{|\mathcal{N}(c)|} O_p^c \cdot 1(O_p^c, max) \tag{5.6}$$

where

$$l = \arg \max \big(\mathcal{H}(c) \big)$$

$$h_{max} = \max \big(\mathcal{H}(c) \big)$$

$$1(O_p^c, max) = \begin{cases} 1, & if \ (max-1)\frac{\pi}{8} \leq O_p^c < (max+1)\frac{\pi}{8} \\ 0, & otherwise \end{cases}$$

In the above equations, h_{max} is the largest bin in $\mathcal{H}(c)$, max is the index of a bin in $\mathcal{H}(c)$, and $1(O_p^c, max)$ is an indicator function that indicates whether the orientation O_p^c of a pixel p in $\mathcal{N}(c)$ belongs to the largest bin h_max of $\mathcal{H}(c)$. An example of cell orientation estimation is shown in Figure 5.2.

5.3 The Proposed Descriptors

5.3.1 Computation of the Cell Orientation Congruence (COrCo) Descriptor

To compute the COrCo descriptor for a cell c, we first introduce a locality sensitive model (an example is shown in Figure 5.3), which defines a circular cell neighbour-

hood $\mathcal{N}'(c)$ for a cell c as follows,

$$\mathcal{N}'(c) = \{nc|dist(c, nc) \leq d\} \tag{5.7}$$

where nc is a neighbouring cell, $dist(c, nc)$ denote Euclidean distance between the centre of c and that of nc, and d is the radius of $\mathcal{N}'(c)$.

The circular cell neighbourhood $\mathcal{N}'(c)$ is divided into a set of 16 half-overlapping angular sections with the same angular width of $\frac{\pi}{4}$. The division of angular sections starts clockwise from the y-axis (which is aligned with the orientation of the cell c). The division is illustrated in Figure 5.3.

We then calculate the cell orientation congruence CON_i of the ith angular section of $\mathcal{N}'(c)$ as follows,

$$CON_i = \sum_{nc=1}^{|\mathcal{N}'(c)|} \Omega_{nc} \cdot \cos(\Phi_{nc}) \cdot 1(\Delta_{nc}, i), \ i = 1, 2, ..., 16 \tag{5.8}$$

where

$$\Omega_{nc} = \frac{\omega_{nc}}{\frac{|\mathcal{N}'(c)|}{\sum\limits_{nc=1} \omega_{nc}}}, \quad \omega_{nc} = e^{\frac{-D_{nc}^2}{2\sigma^2}}$$

$$\Phi_{nc} = \begin{cases} \pi - |O_c - O_{nc}|, & if \ |O_c - O_{nc}| \geq \frac{\pi}{2}, \\ \\ |O_c - O_{nc}|, & otherwise \end{cases}$$

$$1(\Delta_{nc}, i) = \begin{cases} 1, & if \ \frac{(i-1)\pi}{8} \leq \Delta_{nc} < \frac{(i+1)\pi}{8}, i \neq 16 \\ \\ 1, & if \ \frac{(i-1)\pi}{8} \leq \Delta_{nc} < \frac{i\pi}{8}, i = 16 \\ \\ 1, & if \ 0 \leq \Delta_{nc} < \frac{\pi}{8}, i = 16 \\ \\ 0, & otherwise \end{cases}$$

$$\Delta_{nc} = \begin{cases} 2\pi - |\Theta_{nc} - O_c|, & if \ \Theta_{nc} - O_c \leq 0, \\ \\ \Theta_{nc} - O_c, & otherwise \end{cases}$$

$$\Theta_{nc} = \begin{cases} 2\pi - |\theta_{nc}|, & if \ \theta_{nc} < 0, \\ \\ \theta_{nc}, & otherwise \end{cases}$$

$$\theta_{nc} = \arccos \left(\frac{v_{nc} \cdot v_x}{||v_{nc} \cdot v_x||} \right)$$

In the above equations, nc denotes a neighbouring cell in $\mathcal{N}'(c)$, Ω_{nc} is the weight given to nc, which is calculated based on its Euclidean distance D_{nc} to the center of c using a standard deviation σ, Φ_{nc} is the orientation difference of nc compared with c, $1(\Delta_{nc}, i)$ is an indicator function that indicates whether nc is located in the ith angular section of $\mathcal{N}'(c)$, v_{nc} is a vector from the centre of c to that of nc, v_x is an unit vector along the x-axis, and θ_{nc} is the angle between v_{nc} and v_x. Figure 5.3 illustrates that how to localise a nc for an angular section of the COrCo descriptor and compute the cell orientation congruence of this angular section.

We express the COrCo descriptor of the cell c as a feature vector $COrCo(c)$

consisting of the cell orientation congruences of 16 angular sections as,

$$COrCo(c) = \langle CON_1, CON_2, ..., CON_{16} \rangle \qquad (5.9)$$

For example, the above COrCo descriptor calculated for the synthetic epithelial cell shown in 5.3 is likely to output relatively large values in the first and middle elements, which represents an unique orientation congruence pattern of the cell neighbourhood.

We also define a "ring-like" cell neighbourhood (an example is shown in gray colour in Figure 5.3) of the cell c as,

$$\mathcal{R}_i(c) = \big\{ nc | d_{inner} \leq dist(c, nc) \leq d_{outer} \big\} \qquad (5.10)$$

where nc is a neighbouring cell in $\mathcal{R}_i(c)$, d_{inner} and d_{outer} are inner and outer radii respectively, and $dist(c, nc)$ is the Euclidean distance between the centres of c and nc.

Given a set of COrCo descriptors computed using different sizes of "ring-like" cell neighbourhoods of the cell c, the multi-ring version of the COrCo descriptor of the cell c, which we term here as the Multi-Ring Cell Orientation Congruence (MR-COrCo) descriptor, is given as a feature vector $MRCOrCo(c)$, which concatenates the set of COrCo descriptors,

$$MRCOrCo(c) = \langle COrCo(c)_1, COrCo(c)_2, ..., COrCo(c)_{nrings} \rangle \qquad (5.11)$$

where $nrings$ denotes the number of rings and $COrCo(c)_i$ is calculated using $\mathcal{R}_i(c)$ as defined above in (5.10) instead of $\mathcal{N}'_c$ as in (5.7). The MR-COrCo descriptor can more comprehensively describe the cell orientation congruence pattern by using a diversity of "ring-like" cell neighbourhoods rather than .
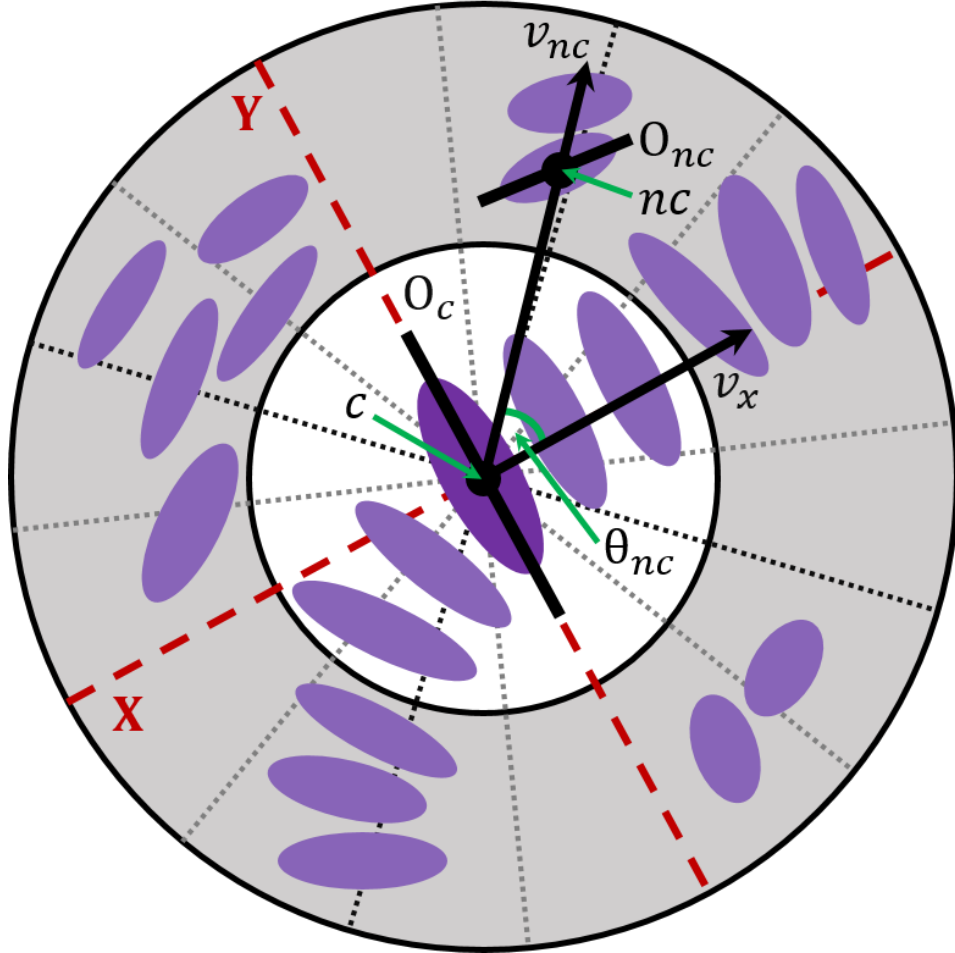
Figure 5.3: The illustration of a locality sensitive model used in the COrCo descriptor. Purple shapes depict cells, black dot depicts the position of the cell, black circles mark the cell neighbourhoods in the descriptor, black dashed lines divide the angular sections of the cell neighbourhoods (the gray regions), red dashed lines are coordinate axes, black line depicts the cell orientation and black arrow depict a vector.

5.3.2 Computation of the Local Binary Cell Orientation Congruence (LBCOrCo) Descriptor

The LBCOrCo descriptor, an the other hand, attempts to describe the cell orientation congruence, in the form of local binary pattern. Similar to computing the COrCo descriptor for a cell c, we start computing the LBCOrCo descriptor by first introducing a locality model shown in Figure 5.4(c) which defines a circular cell neighbourhood $\mathcal{N}'''(c)$ for the cell c using (5.7). $\mathcal{N}'''(c)$ is also divided into a set of 16 half-overlapping angular sections with equal radians. However, the difference here is that the division of $\mathcal{N}'''(c)$ starts clockwise from the x'-axis, which is illustrated in Figure 5.4(c). We then define a vector $CON'(c)$ which specifies the cell orientation congruence of each angular section of $\mathcal{N}'''(c)$ as,

$$CON'(c) = \langle CON'_1, CON'_2, ..., CON'_{16} \rangle \tag{5.12}$$

where CON'_i is the congruence factor of the ith angular section of $\mathcal{N}'''(c)$ and is calculated as follows,

$$CON'_i = \sum_{nc=1}^{|N''(c)|} \Omega'_{nc} \cdot \Phi'_{nc} \cdot 1(\Theta'_{nc}, i), \ \ i = 1, 2, ..., 16 \tag{5.13}$$

where

$$\Omega'_{nc} = \frac{\omega_{nc}}{\sum\limits_{nc=1}^{|N''(c)|} \omega_{nc} \cdot 1(\Theta'_{nc}, n)}, n = 1, 2, ..., 16$$

$$\omega_{nc} = e^{\frac{-D_{nc}^2}{2\sigma^2}}$$

$$\Phi'_{nc} = \begin{cases} \pi - |O_{nc} - \phi_{nc}|, & if \; |O_{nc} - \phi_{nc}| \geq \frac{\pi}{2}, \\ |O_{nc} - \phi_{nc}|, & otherwise \end{cases}$$

$$\phi_{nc} = \begin{cases} \Theta'_{nc} - \pi, & if \; \Theta'_{nc} \geq \pi, \\ \Theta'_{nc}, & otherwise \end{cases}$$

$$1(\Theta'_{nc}, i) = \begin{cases} 1, & if \; \frac{(i-1)\pi}{8} \leq \Theta'_{nc} < \frac{(i+1)\pi}{8}, i \neq 16 \\ 1, & if \; \frac{(i-1)\pi}{8} \leq \Theta'_{nc} < \frac{i\pi}{8}, i = 16 \\ 1, & if \; 0 \leq \Theta'_{nc} < \frac{\pi}{8}, i = 16 \\ 0, & otherwise \end{cases}$$

$$\Theta'_{nc} = \begin{cases} 2\pi - |\theta_{nc}|, & if \; \theta_{nc} < 0, \\ \theta_{nc}, & otherwise \end{cases}$$

$$\theta'_{nc} = \arccos\left(\frac{v_{nc} \cdot v_{x'}}{||v_{nc} \cdot v_{x'}||}\right)$$

In the above equations, nc denotes a arbitrary neighbouring cell in $\mathcal{N}''(c)$, Ω'_{nc} is the weight given to nc, which is calculated based on its Euclidean distance D_{nc} to the centre of c using a standard deviation σ (It is important to note that only the neighbouring cells located with the nth angular section of $\mathcal{N}''(c)$ used in calculating the weight for computing CON'_i. To differentiate it from the weight in Equation (5.8), it is denoted as Ω'_{nc} using a prime symbol.), Φ_{nc} is the orientation verticality of nc in the nth angular section of $\mathcal{N}''(c)$, $1(\Theta'_{nc}, i)$ is an indicator function that indicate whether the neighbouring cell nc is located in the nth angular section of $\mathcal{N}''(c)$, v_{nc} is a vector from the centre of c to that of nc, v'_x is an unit vector along the x-axis, and θ_{nc} is the included angle between v_{nc} to v'_x. A locality sensitive

model used in the LBCOrCo descriptor is illustrated in Figure 5.4.

Next, we define a priority vector $P(c)$ to specify the importance of each angular section in $\mathcal{N}''(c)$ as,

$$P(c) := \langle P_1, P_2, ..., P_{16} \rangle \tag{5.14}$$

In fact, the cell orientation congruence factor from an angular section which contains high number of neighbouring cells is more representative than the others. More importantly, re-ordering the congruence vector according to the priorities of angular sections will make the LBCOrCo descriptor rotation-invariant. Therefore, we calculate the priority P_i of the ith angular section of $\mathcal{N}''(c)$ as follows,

$$P_i = \sum_{nc=1}^{|\mathcal{N}''(c)|} \Omega''_{nc} \cdot 1(\Theta'_{nc}, i), \ n = 1, 2, ..., 16$$

$$\Omega''_{nc} = \frac{\omega_{nc}}{|NC_{nc}| \displaystyle\sum_{nc=1} \omega_{nc}}, \ \omega_{nc} = e^{\frac{-D_{nc}^2}{2\sigma^2}} \tag{5.15}$$

where Ω''_{nc} is calculated the same as the weight in (5.8) and $1(\Theta'_{nc}, i)$ is defined in Equation 5.3.2. Next, we sort $CON'(c)$ in descending order using $P(c)$ as,

$$CON''(c) := sort\big(CON'(c), \underset{descend}{\mathrm{ord}}(P(c))\big) \tag{5.16}$$

where $CON''(c)$ is a new feature vector which represents the cell orientation congruence of the cell neighbourhood $\mathcal{N}''(c)$ and is defined as,

$$CON''(c) = \{CON''_1, CON''_2, ..., CON''_{16}\} \tag{5.17}$$

Finally, the LBCOrCo descriptor for the cell c is computed, in the form of a decimal
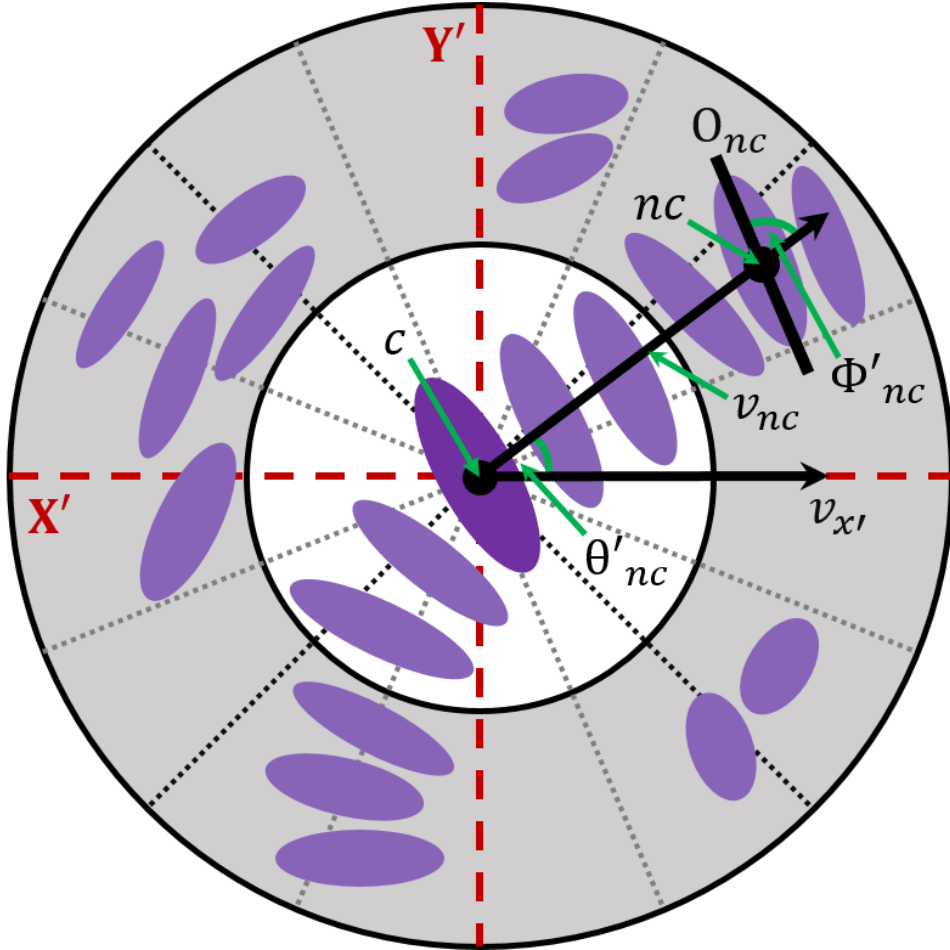
Figure 5.4: The illustration of a locality sensitive model in the LBCOrCo descriptor, black dot depicts the position of the cell, purple shapes depict cells, black circles mark the cell neighbourhoods in the descriptor, black dashed lines divide the angular sections of the cell neighbourhood (gray regions), red dashed lines are coordinate axes, black line depicts the cell orientation and black arrow depict a vector.

number LBCOrCo(c), as follows,

$$LBCOrCo(c) = \sum_{n=1}^{16} 2^{(16-i)} \cdot 1(CON_n''), \ i = 1, 2, ..., 16$$

$$1(CON_i'') = \begin{cases} 1, & if \ CON_i'' > \frac{\pi}{4}, \\ 0, & otherwise \end{cases} \qquad (5.18)$$

where $1(CON_i'')$ is an indicator function which examines whether the cell orientation congruence factor of the ith angular section is larger than $\frac{\pi}{4}$.

Given a set of LBCOrCo descriptors of the cell c, which is computed using different size of "ring-like" cell neighbourhood, its multi-ring version of the LBCOrCo descriptor , which we term here as the Multi-Ring Cell Orientation Congruence (MR-LBCOrCo) descriptor, is given as a feature vector $MRLBCOrCo(c)$ by concatenating all its LBCOrCo descriptors as,

$$MRLBCOrCo = \langle LBCOrCo(c)_1, LBCOrCo(c)_2, ..., LBCOrCo(c)_{nrings} \rangle \quad (5.19)$$

where $nrings$ denotes the number of rings. The MR-COrCo descriptor is also proposed to more comprehensively describe the cell orientation congruence pattern of a cell neighbourhood.

5.3.3 Epithelium Segmentation by Labelling Potential Epithelium Superpixels

In this step, we first compute the proposed descriptors for the cells located within potential epithelial superpixels. Second, we employ the Random Forests classifier together with the proposed descriptors to identify the epithelial cells. Next, a potential epithelial superpixel which contains any non-epithelial cell or an empty potential epithelial superpixel (containing no cells) is initially categorized as a non-epithelial superpixel, otherwise it is marked as an epithelial superpixel. However,

the non-epithelial superpixels containing epithelial cells can be mistakenly classified, thus we at last initialise a refinement process to reclassify the mistakenly classified non-epithelial superpixels as below,

1. Let us denote a non-epithelial superpixel as S_{ne} and a potential epithelial superpixel as S_{pe}. Given a S_{ne}, we defined a S_{pe} which immediately connects to S_{ne} as its level 1 neighbour which is denoted as S_i^1. A set of S_i^1 is denoted as $\{S_i^1\}$;

2. We define a S_{pe} as a level 2 neighbourhood of S_{pe} if it immediately connects to any S_i^1 and $S_{pe} \notin \{S_j^1\}$, which is denoted as S_j^2. The set of level 2 neighbours is denoted as $\{S_j^2\}$;

3. The cell are identified as epithelial cells by the random forests classifier with the proposed descriptors are defined as true epithelial cells, otherwise they are defined as false epithelial cells. The numbers of true and false epithelial cells within S_{ne} and its neighbours $\{S_i^1\}$ and $\{S_j^2\}$ are counted and denoted as N_{true} and N_{false}. respectively. S_{ne} is remarked as an epithelial superpixel if $N_{true} \geq N_{false}$, otherwise it remains as a non-epithelial superpixel.

A binary image can be achieved by connecting the epithelial superpixels all together after the refinement process, and the final epithelium is segmented by removing the small isolated connected components from the binary image, i.e., any region smaller than 500 pixels, which is empirically determined according to the observations on the hand-marked images.

5.4   Evaluation of the Proposed Descriptors

We devise three experiments for evaluating the epithelium segmentation accuracies when using the proposed descriptors. The first experiment examines the segmentation accuracy of all the proposed descriptors, i.e., COrCo, MR-COrCo, LBCOrCo,

MR-LBCOrCo on a randomly selected subset of the image dataset. The second experiment compares the top-two of the proposed descriptors with 5 state-of-the-art segmentation methods, i.e.,[126], [123], [124], [132], and [134]. Since most of the state-of-the-art segmentation methods are designated to segment glandular structures (glandular epithelium) rather than luminal epithelium, the experiment aims to evaluate the performance of the proposed descriptors against the other methods on segmenting glandular epithelium. Our image dataset contains 150 hand-marked images which are cross-validated by two experts from UHCW. We manually selected a subset (50 images) from the image dataset to guarantee that each image contains at least one glandular structure, and crop a sub-image from each of these images, which contain only glandular structure. The sub-image are used in the second experiment. In the third experiment, to highlight the advantages of the proposed descriptors, we also evaluate all the methods on the complete image dataset for both glandular and luminal epithelium segmentation, the images may contain both luminal and glandular epithelium or one of them.

We measure the segmentation accuracy using a modified version of the Dice-score proposed in [132]. The Dice-score is used to numerically quantify the similarity between a segmented region and its corresponding Ground Truth in both pixel-level and epithelium-level. The closer to 1 the Dice score of a region segmentation, the more accurate is it. The pixel-level Dice score is calculated as,

$$Dice_{pix}(Seg, Grt) = 2\left(\frac{|Seg \cap Grt|}{|Seg| + |Grt|}\right) \tag{5.20}$$

where $Dice_{pix}$ is the pixel-level Dice score, Seg is a set of pixels segmented as an epithelium and Grt is a set of pixels annotated as Ground Truth region. We consider all segmented epithelium in one image as a whole object in calculating the pixel-level Dice score.

To measure the weighted accuracy of the segmentation of each individual

epithelium, we calculate the epithelium-level Dice score based on the pixel-level Dice score as follows,

$$Dice_{epi}(Seg, Grt) =$$

$$\frac{1}{2}\left(\sum_{i=1}^{NS} w_i \cdot Dice_{pix}(Seg_i, Grt_i) + \sum_{i=1}^{NG} \dot{w}_i \cdot Dice_{pix}(\dot{Grt}_i, \dot{Seg}_i)\right)$$

$$w_i = \frac{1}{2}\left(\frac{|Seg_i|}{|Seg|} + \frac{|Grt_i|}{|Grt|}\right)$$

$$\dot{w}_i = \frac{1}{2}\left(\frac{|\dot{Grt}_i|}{|Grt|} + \frac{|\dot{Seg}_i|}{|Seg|}\right)$$

(5.21)

where $Dice_{obj}$ is the object-level Dice score, Seg_i is a set of pixels segmented as the ith epithelium region, Grt_i is a set of pixels annotated as the ith Ground Truth region which maximally overlaps with Seg_i among all Ground Truth regions, NS is the total number of the segmented epithelium regions, $\dot{Grt}_i$ is a set of pixels segmented as the ith Ground Truth region, $\dot{Seg}_i$ is a set of pixels segmented as the ith epithelium region which maximally overlaps with Seg_i among all the segmented epithelium regions, and NG is the total number of Ground Truth regions.

5.4.1 Comparison of the Proposed Descriptors on Epithelium Segmentation

The radius (in pixels) of the cell neighbourhood is a sensitive and key parameter of all the proposed descriptors, which is empirically tuned according to the observation on the image dataset. This experiment examines the performances of the proposed descriptors with different cell neighbourhood radii for both luminal and glandular epithelium segmentation on 50 images form the image dataset.

The idea of the propose descriptors is to take the advantage of orientation congruence of neighbouring cells so that the neighbourhood radii must guarantee that the descriptors can locate some cells. We set up the radius starting from 60 pixels (which enable the proposed descriptors to capture a couple of cells in the very beginning), and increasing by every 30 pixels, to 180 pixels at maximum. We
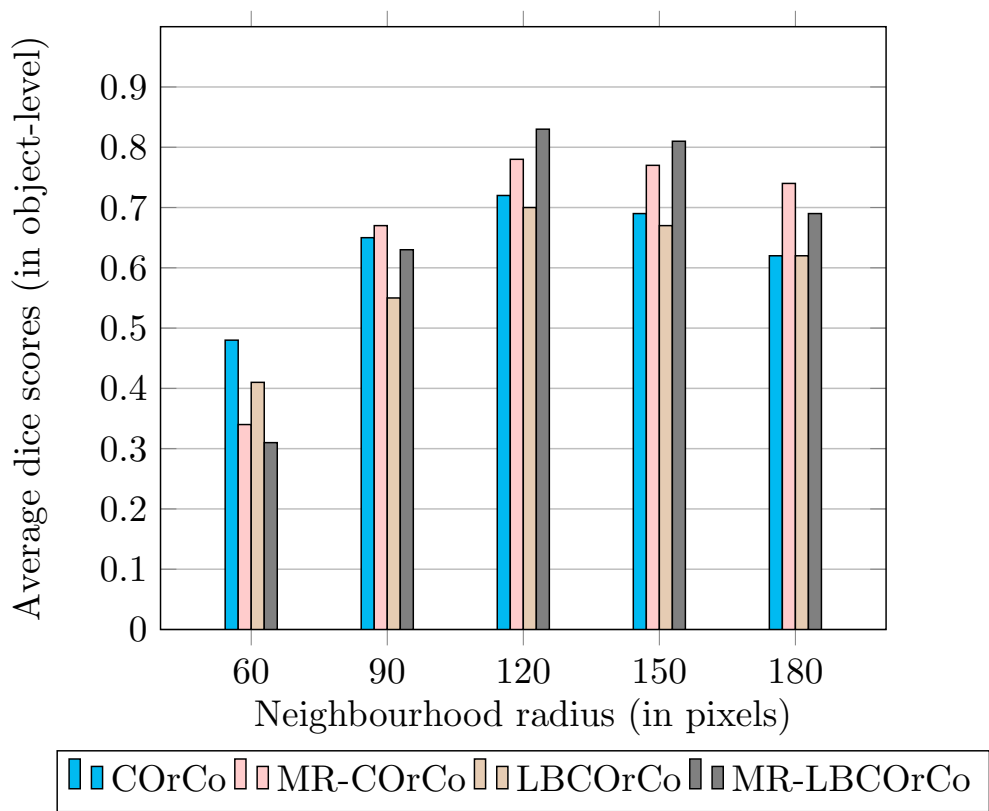
Figure 5.5: Epithelium segmentation accuracy of the proposed descriptors.
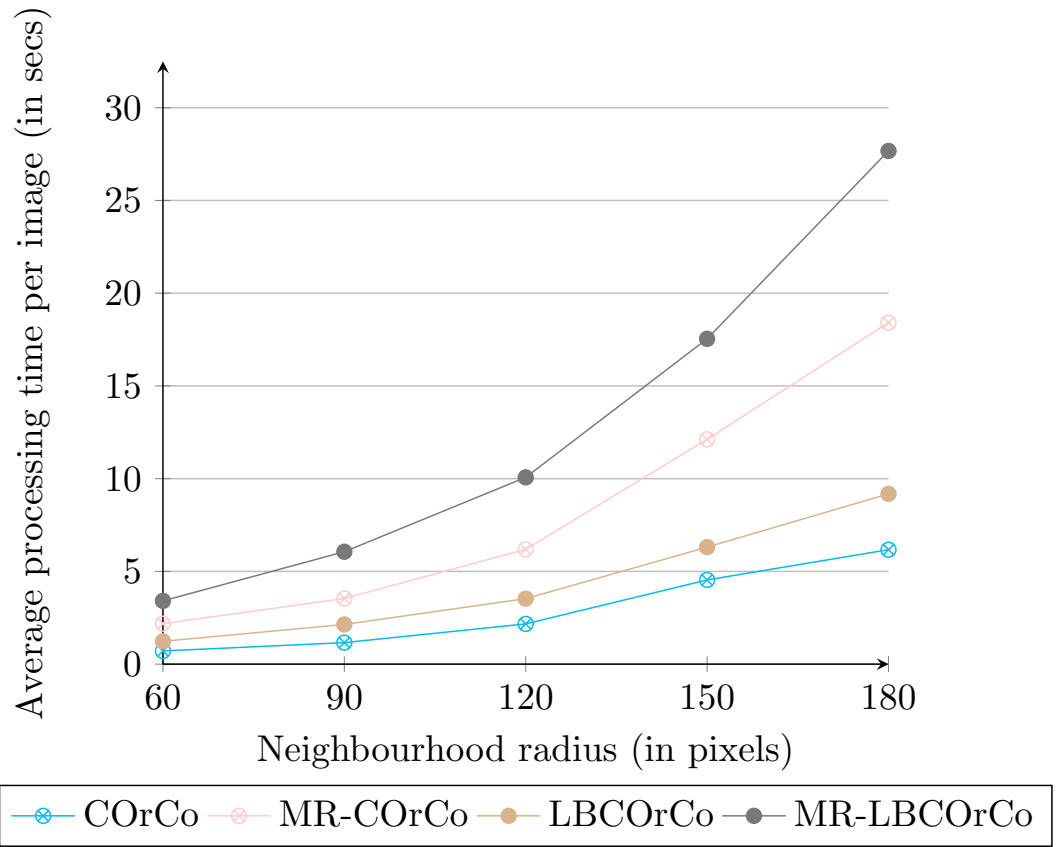
Figure 5.6: Comparison of computational speeds between different proposed descriptors.

use 3 "ring-like" neighbourhoods for each of the multi-ring versions of the proposed descriptors.

Figure 5.5 shows the segmentation accuracy of various proposed descriptors using different cell neighbourhood radii. The results show that all the proposed descriptors perform poorly in the case of using a maximum cell neighbourhood radius 30 pixels. The proposed descriptors using multi-ring cell neighbourhood have much lower accuracy compared with the descriptors using single neighbourhood in this case. It is due to that small radius having difficulty in locating enough cells to compute the orientation congruence, especially, very few of cells can be found within a ring width 20 pixels in the multi-ring versions.

The accuracy, however, is significantly improved by increased radius, but decreases slightly when the radii becomes larger than 120 pixels. The MR-LBCOrCo and MR-COrCo descriptors are the top-two in terms of the average Dice score, but the MR-LBCOrCo descriptor has the lowest accuracy when the smallest radius 60 is employed for all the descriptors. In conclusion, the multi-ring cell neighbourhood can improve the accuracy when an appropriate value of the starting radius is used. Although the MR-LBCOrCo descriptor using a radius 120 pixels outputs the most accurate segmentation, it is also very sensitive to the cell neighbourhood radius setting, i.e., inappropriately tuned radii may cause significant performance reduction, which is shown in Figure 5.5.

We also examine the computational efficiencies of the proposed descriptors, 50 images are used in the examination and each image contains 975.4 detected cells on average. The average computational speeds per image of the proposed descriptors are given in Figure 5.6. The computational costs of these descriptors increase along with expanding the neighbourhood radius, for LBCOrCo and MR-LBCOrCo, the increase is dramatic. The COrCo descriptor is the fastest descriptor and LBCOrCo is slowest. The cost of the MR-COrCo descriptor is roughly 3 times of the COrCo descriptor. This is due to the fact that 3 ring-like neighbourhoods are used for the

MR-COrCo descriptor in the experiment, which can be considered as 3 times repeat computations of the COrCo descriptor. This similar increment of the computational cost is also observed from the LBCOrCo and MR-LBCOrCo descriptors. Overall, the MR-LBCOrCo descriptor shows the best result and an acceptable computational complexity for our dataset.

5.4.2 Evaluation of the Top-Two Proposed Descriptors for Glandular Epithelium Segmentation

In this experiment, the top-two of the proposed descriptors are evaluated against 5 state-of-the-art methods: [126], [123], [124], [132], and [134], on 50 sub-images which contain only glandular structures. The algorithms in [126] [123], [124], and [132] were proposed for segmenting the complete glandular structure, and they generally connect a set of epithelial cells to generate a close boundary to mark the glandular structures. To make the comparison fair for the task of the epithelium segmentation, in their results we morphologically dilate the boundaries of glandular epithelium by an average thickness 30 pixel, and also remove the lumen regions from their segmented glandular structures. The experimental results are reported in Table 5.1, which show that the MR-COrCo and MR-LBCOrCo descriptors yields more accurate segmentation than the 5 state-of-the-art methods.

In fact, the thickness of both luminal and glandular epithelium can differ greatly between different glandular structures, and even within an individual glandular structure. Therefore, the proposed descriptors can achieve better accuracy than the state-of-the-art methods, since they try to construct a boundary line to mark the glandular structures by using a single layer of epithelial cells. An example of the glandular epithelium with greatly varied thickness is shown in Figure 5.7 (a), and the segmentation of lumen and potential epithelium regions are shown in Figures 5.8 (a) and (b), respectively, the classification of the cells located within potential epithelium regions using the MR-COrCo and MR-LBCOrCo descriptors

Table 5.1: The segmentation accuracies of the compared methods on the sub-images containing only glandular epithelium. Dice scores are reported by the averages $\pm$ standard deviations and the best results are in bold.

Methods	Dice Scores	
	Pixel-Level	Epithelium-Level
Farjam *et al.* [126]	0.76 ± 0.04	0.74 ± 0.05
Nguyen *et al.* [123]	0.61 ± 0.08	0.59 ± 0.08
Naik *et al.* [124]	0.72 ± 0.04	0.71 ± 0.05
TGPM [132]	0.75 ± 0.03	0.74 ± 0.03
COrE [134]	0.65 ± 0.08	0.62 ± 0.09
MR-COrCo	**0.79 ± 0.03**	**0.78 ± 0.03**
MR-LBCOrCo	**0.83 ± 0.02**	**0.82 ± 0.03**

are shown in 5.9 (a) and (b), respectively. The final epithelium segmentation results shown in Figures 5.10 (a) and (b), respectively, which demonstrate that the accurate segmentation of the glandular epithelium with greatly varied thickness can be achieved using the MR-COrCo and MR-LBCOrCo descriptors.

Another common problem of all the methods is that they often mistakenly segment the large blank (background) areas as lumen regions. Both Figures 5.7 (a) and 5.11 (a) show two examples of the images containing large blank (background) area. In the middle of Figure 5.7 (a), we observe that an elongated blank background region is surrounded by both a group of stromal cells on the left side and an epithelium regions on the right side. In Figure 5.11 (a), a large blank background region is observed at the centre of the image, and is enclosed by a circles of stromal cells. Figures 5.8 (a) and 5.12 (a) show the lumen segmentation of Figures 5.7 (a) and 5.11 (a), the cells surrounding the segmented lumen are first marked as the
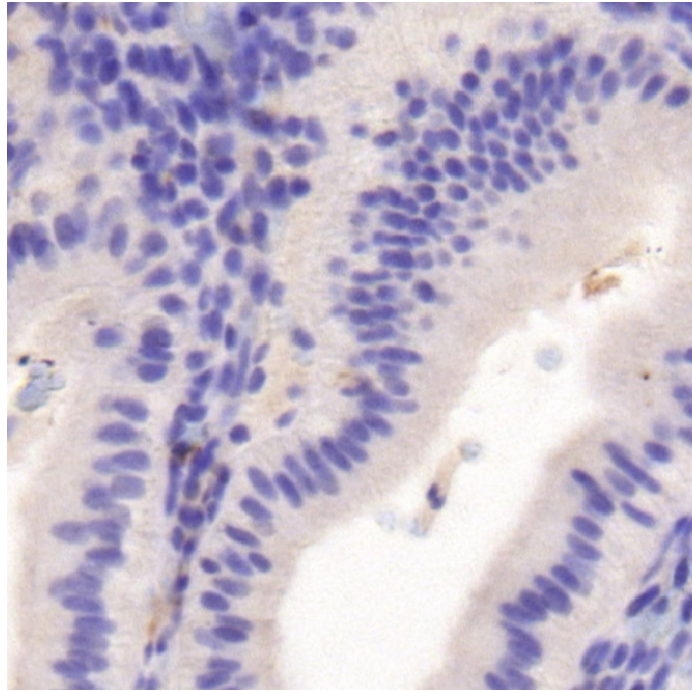
(a)
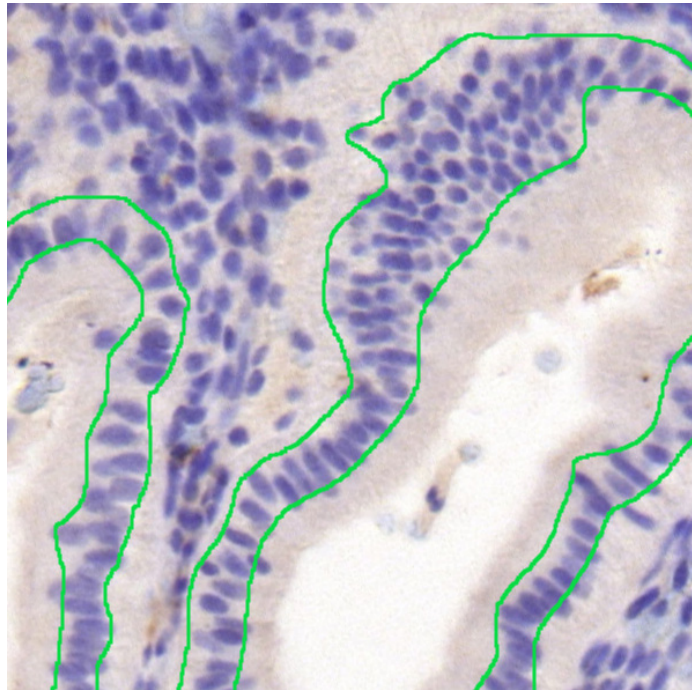
(b)

Figure 5.7: (a) is a cropped local region from an input image and (b) shows the hand-marked Ground Truth in (a) using green lines.
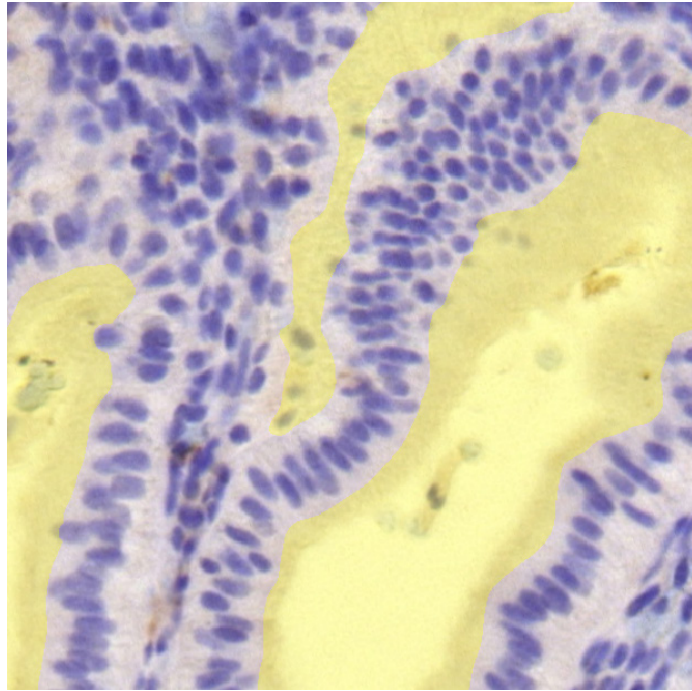
(a)
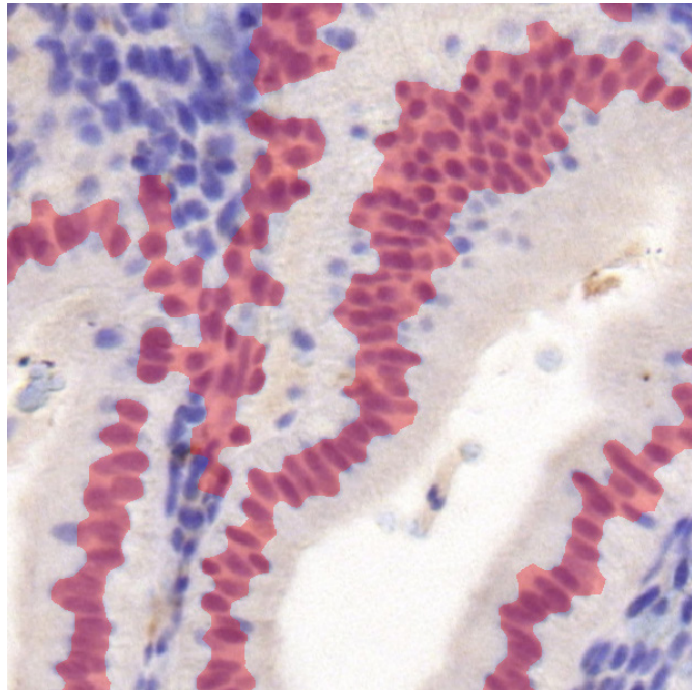
(b)

Figure 5.8: Lumen segmentation of Figure 5.7(a) is shown in transparent yellow and potential epithelium region is shown in transparent red in (b).
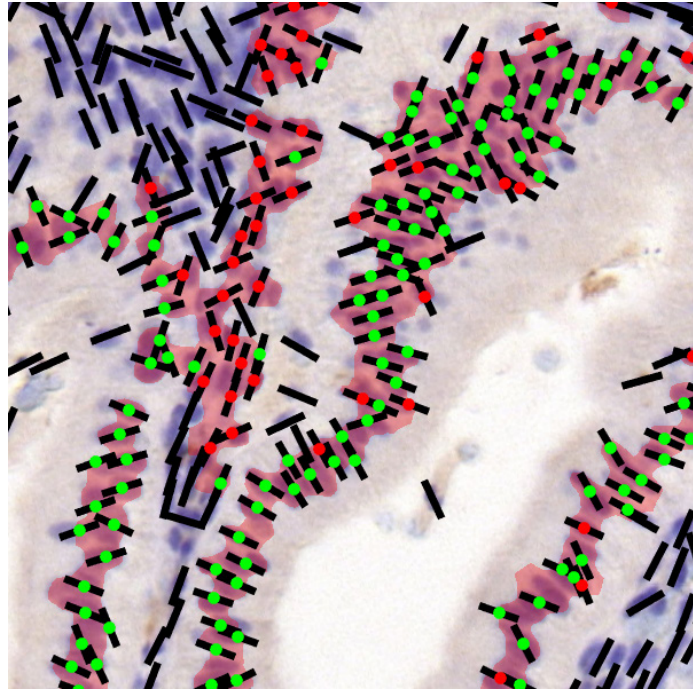
(a)
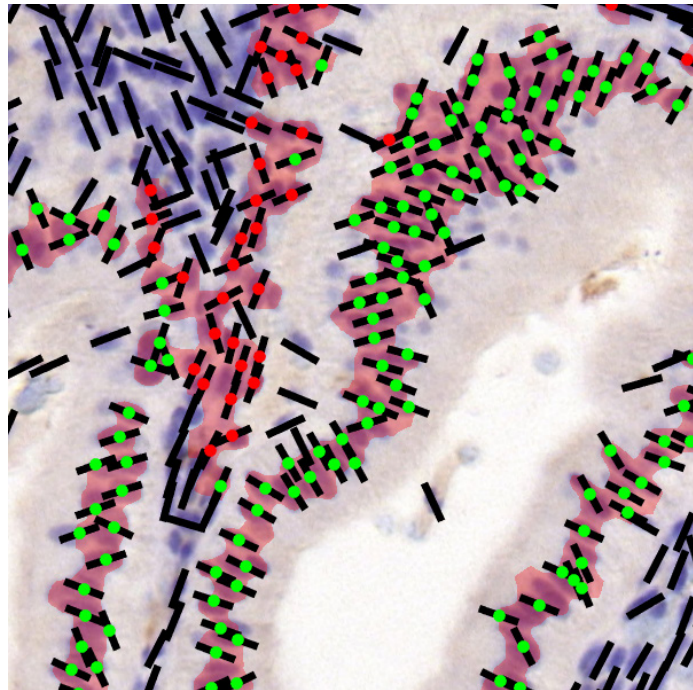
(b)

Figure 5.9: (a) and (b) show the classification results of Figure 5.7(a) using the MR-COrCo and MR-LBCOrCo descriptors, respectively. Black bars depict cell orientations, red dots depict the cells classified as non-epithelial cells, and green dots depict the cells classified as epithelial cells.

119

(a)

(b)

Figure 5.10: (a) and (b) show the segmenatation results of Figure 5.7(a) using the MR-COrCo and MR-LBCOrCo descriptors, respectively. Black bars depict cell orientations. The differences between (a) and (b) are highlighted using black arrows.

potential epithelium regions, which are shown in Figures 5.8 (b) and 5.12 (b). Figures 5.9 (a) and 5.13 (a) then show that the classification of the cells located within potential epithelium regions using the MR-COrCo and MR-LBCOrCo descriptors, respectively. In Figures 5.10 (a) and (b), it is observed that most of stromal cell regions have been removed from the segmentation result, although a few of cells are mistakenly classified as epithelial cell (as shown in Figures 5.9 (a) and (b)), most of potential epithelium regions can still be removed by the algorithm because a majority of cells within these potential epithelium regions are classified as stromal cells.

On the other hand, the state-of-the-art methods generally also segment the large blank regions shown in Figures 5.7 (a) and 5.11 (a) as lumen regions. They attempt to construct a boundary which marks these blank regions to report them as glandular structures. Moreover, the algorithms in [124] uses a colour-based pixel clustering method to distinguish between stromal and epithelial cell. This leads to that both stromal cells and epithelial cells are classified as the same type. The active contour based cell segmentation algorithm in [134] has difficulty in segmenting dense cell cluster, which often merge multiple individual cell as one single cell. Hence, their PCA based cell orientation estimation method consequently fails to output the correct classification. The methods in [124] and [134] also show their bottleneck in segmenting relatively sparsely distributed cells or densely grouped cells, which significantly affect the epithelium segmentation results. Consequently, both [124] and [134] attain low accuracy and report large standard deviations of the Dice score.

A small "Hive-like" epithelial structure marked in green circle at the bottom of Ground Truth image (shown in Figure 5.11 (b)). None of the proposed descriptors and the state-of-the-art methods is able to detect this particular structure, it is due to that there is no lumen region can be recognised by any of the methods to locate the "Hive-like" structure. Another common drawback of the proposed descriptors is that

121

(a)
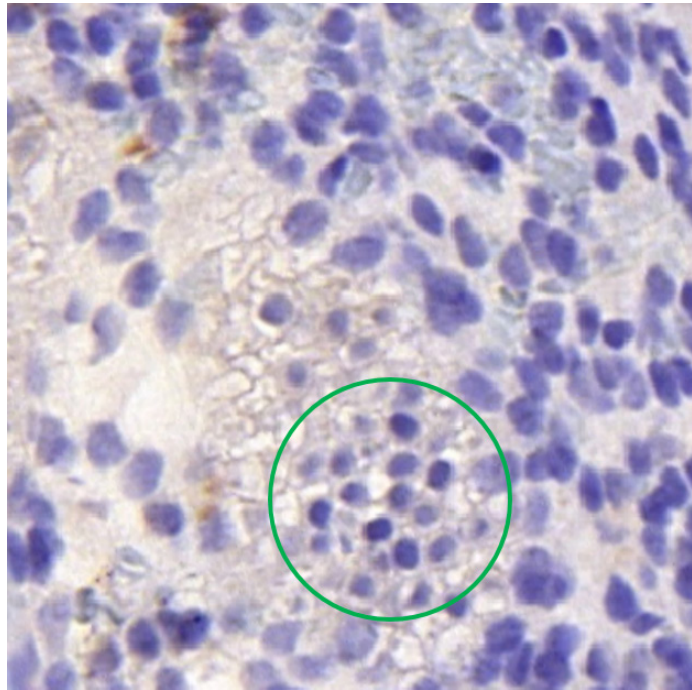
(b)

Figure 5.11: (a) is a cropped local region from an input image and (b) shows the hand-marked Ground Truth in (a) using green lines.
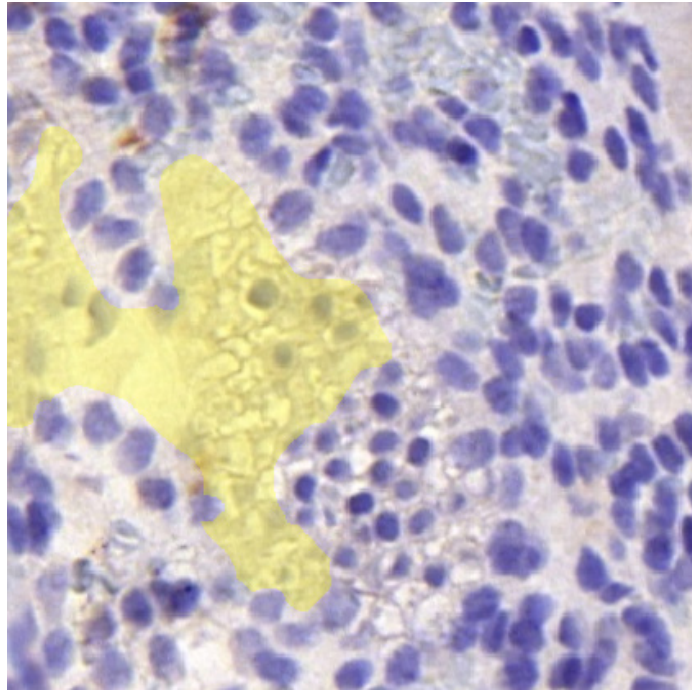
(a)
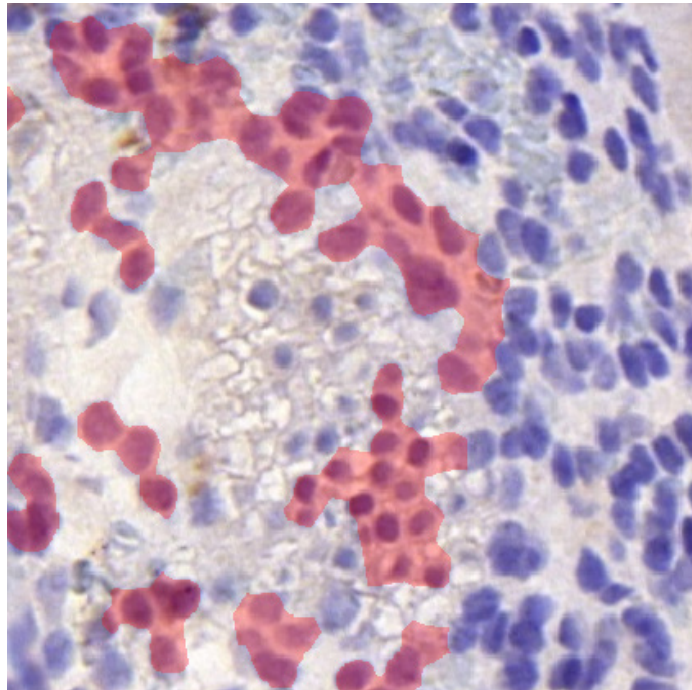

(b)

Figure 5.12: Lumen segmentation of Figure 5.11 (a) is shown in transparent yellow in (a) and potential epithelium region is shown in transparent red in (b).
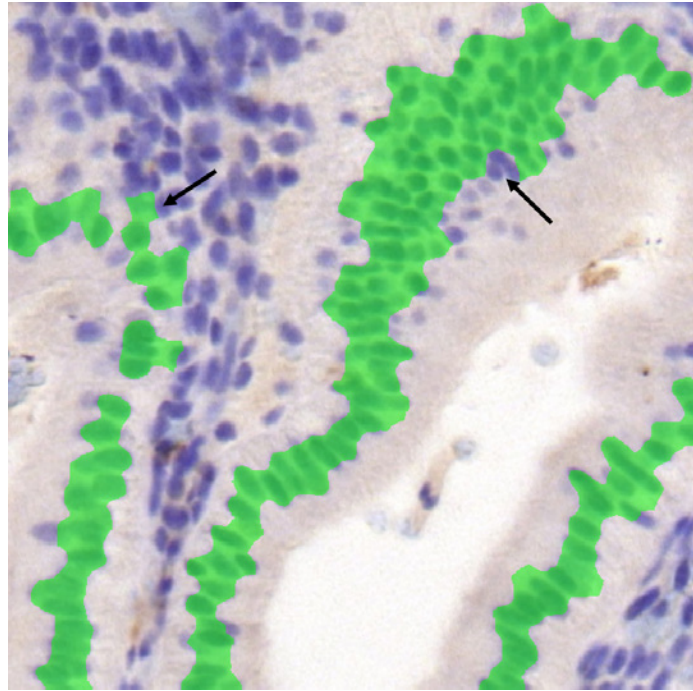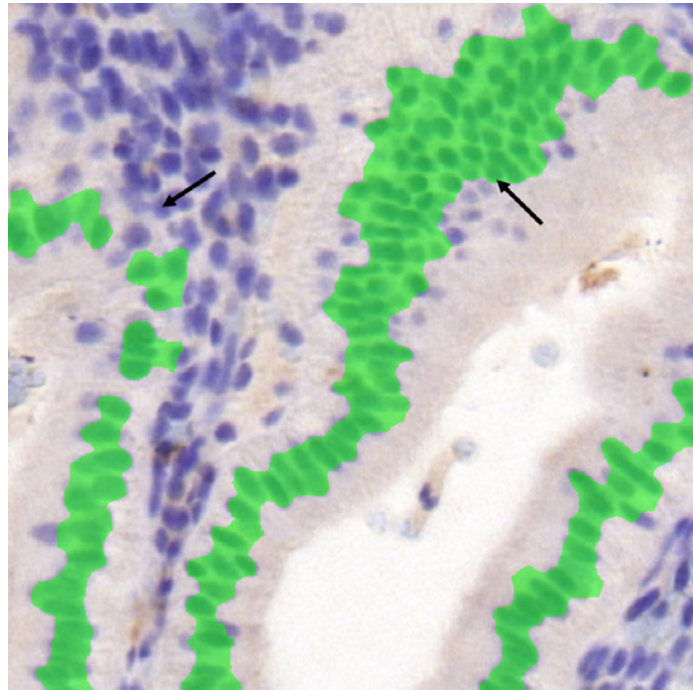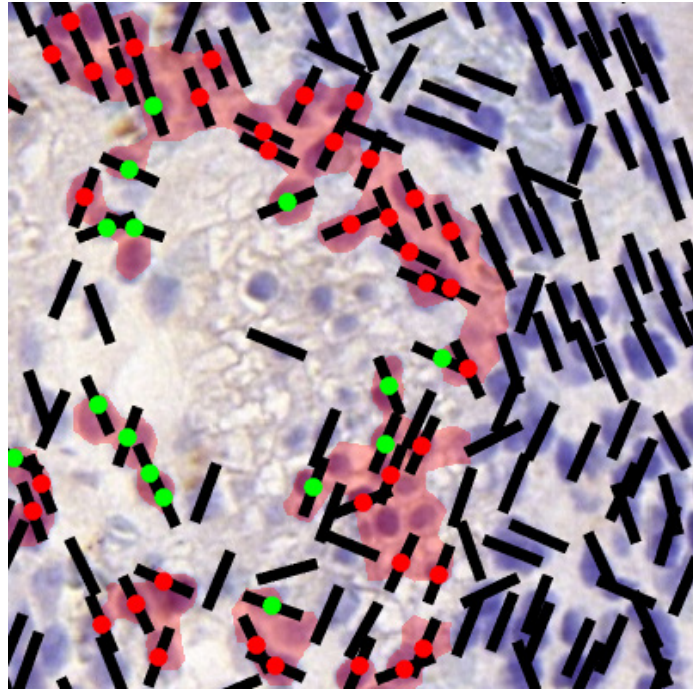
(a)
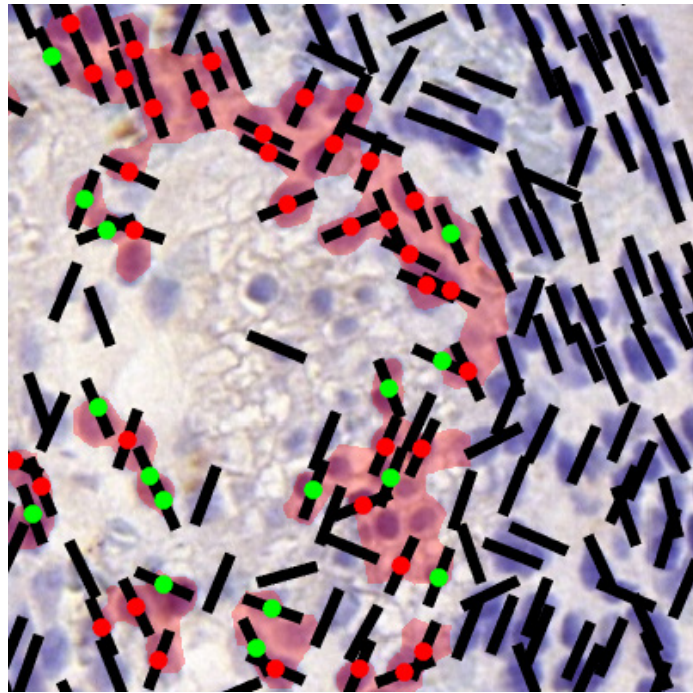
(b)

Figure 5.13: (a) and (b) show the classification results of Figure 5.11 (a) using the MR-COrCo and MR-LBCOrCo descriptors, respectively. Black bars depict cell orientations, red dots depict the cells classified as non-epithelial cells, and green dots depict the cells classified as epithelial cells.
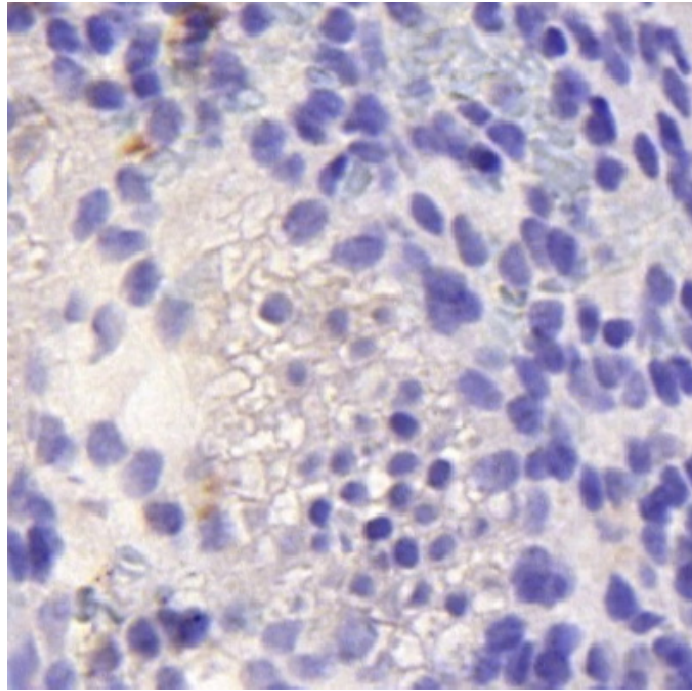
(a)

(b)

Figure 5.14: (a) and (b) show the segmenatation results of Figure 5.11 (a) using the MR-COrCo and MR-LBCOrCo descriptors, respectively. Black bars depict cell orientations

computing cell orientation congruence on the small and circular cells from the'Hive-like" epithelial structure is not entirely reliable. Moreover, their cell orientation congruence are very similar to the stromal cells. Hence, the 'Hive-like" epithelial structures is the main challenge which prevents the proposed method to generate highly accurate segmentation results. However, the"Hive-like" epithelial structures exhibit an very unique textural appearance compared with other epithelial regions or stromal cell regions. For example, the cells from the"Hive-like" epithelial structures exhibit as evenly spaced circular spots, whereas the cells from other epithelium or stromal cells are normally elongated and either homogeneously spread or densely grouped. Therefore, it is possible to develop a machine learning based method which utilises this unique textural feature to classify the image regions of "Hive-like" epithelial structures.

5.4.3 Evaluation of the Top-Two Proposed Descriptors for Simultaneous Segmentation of Glandular and Luminal Epithelium

Table 5.2 indicates that the state-of-the-art methods perform with lower accuracies compared with the proposed method in this experiment. Both the MR-COrCo and MR-LBCOrCo descriptors slightly drop their accuracies by 0.02 to 0.03, respectively, which shows that they are also able to accurately segment luminal epithelium. The MR-COrCo and MR-LBCOrCo descriptors show a slightly reduced accuracy. It is due to that the cell regions at luminal epithelium Boundary are a mixture of stromal and epithelial cells, which leads to inaccurate cell orientation congruence estimation for these regions.

On the other hand, [126], [123], [124], and [132] produce lower accuracy than in the above experiment, because the lumen segmentation algorithms used in these methods often segment the background regions as lumen, which consequently cause the stromal cells at the boundaries of these background regions are mistakenly classified as epithelial cells. In fact, the Ground Truth image in Figure 5.15 (b) shows

Table 5.2: The glandular and luminal epithelium segmentation accuracies of the compared methods on the complete image dataset. Dice scores are reported by the averages ± standard deviations and the best results are in bold.

Methods	Dice Scores	
	Pixel-Level	Epithelium-Level
Farjam *et al.* [126]	0.67 ± 0.05	0.66 ± 0.06
Nguyen *et al.* [123]	0.58 ± 0.09	0.56 ± 0.10
Naik *et al.* [124]	0.66 ± 0.05	0.65 ± 0.05
TGPM [132]	0.70 ± 0.04	0.68 ± 0.05
COrE [134]	0.58 ± 0.11	0.54 ± 0.12
MR-COrCo	$\mathbf{0.76 \pm 0.05}$	$\mathbf{0.76 \pm 0.05}$
MR-LBCOrCo	$\mathbf{0.82 \pm 0.03}$	$\mathbf{0.80 \pm 0.04}$

that only the cells at the top-left are from luminal epithelium and the cells from the bottom-right, despite the fact that they are located along the same tissue boundary. The state-of-the-art methods generally segment the large empty background region shown in Figure 5.15 (a) as lumen, and then attempt to generate a enclosed curve on the cells packed at the boundary of the background region to mark a glandular structure. Although the background region is also classified as lumen by the proposed method (as shown in Figure 5.16 (a)), the it is used for locating potential epithelial regions rather than directly reporting an existence of a glandular structure. Figures 5.17 (a) and 5.17 (b) show the cell classification results using the MR-COrCo and MR-LBCOrCo descriptors, respectively.

The MR-COrCo descriptor has difficulty in correctly classifying the cell located at the bottom-right of Figure 5.15 (a), which consequently cause that a few stromal cell regions located at the bottom-right of Figure 5.15 (a) are also included
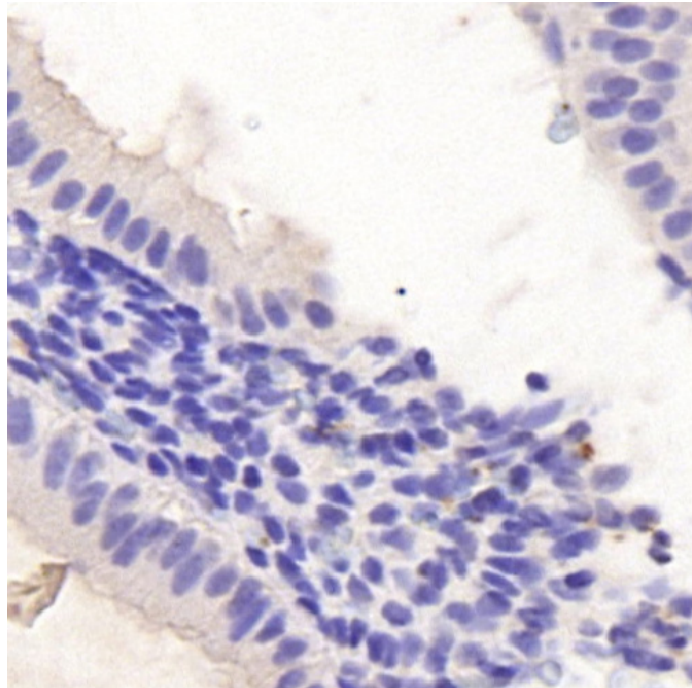
(a)
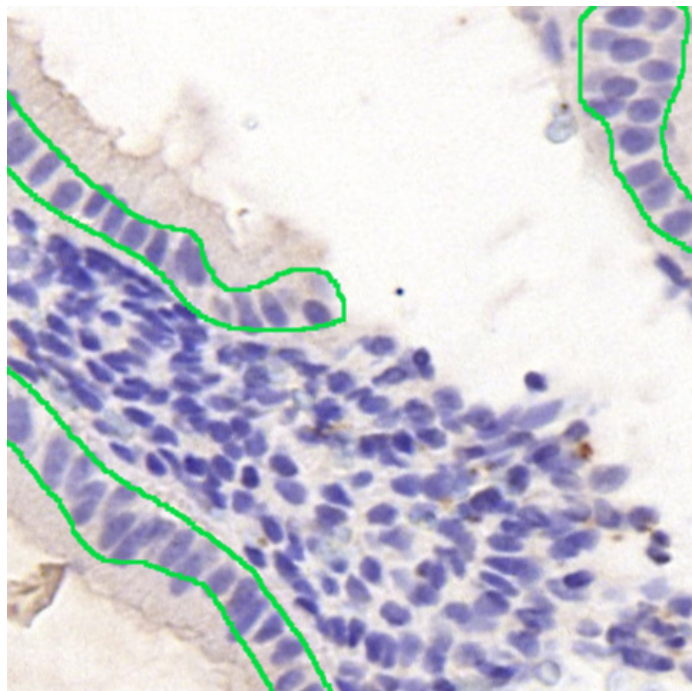
(b)

Figure 5.15: (a) is a cropped local region from an input image and (b) shows the hand-marked Ground Truth in (a) using green lines.
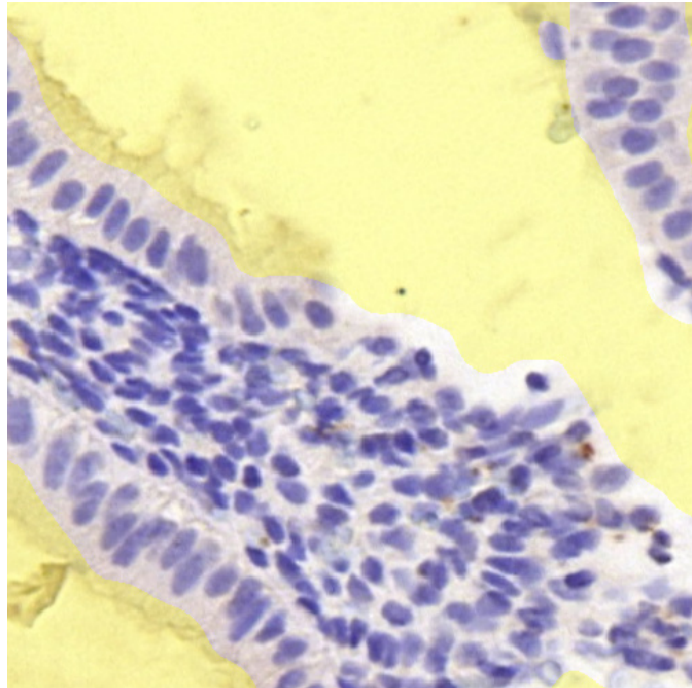
(a)
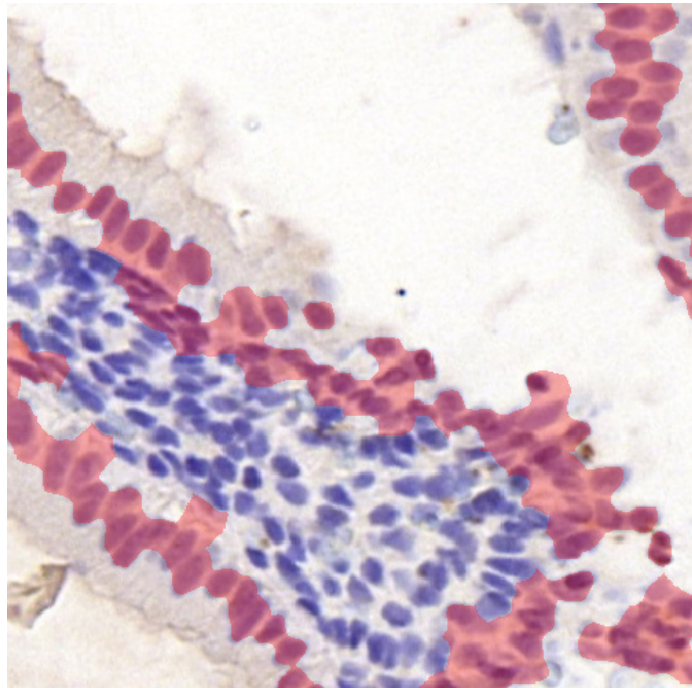
(b)

Figure 5.16: Lumen segmentation of Figure 5.15(a) is shown in transparent yellow in (a) and potential epithelium region is shown in transparent red in (b).
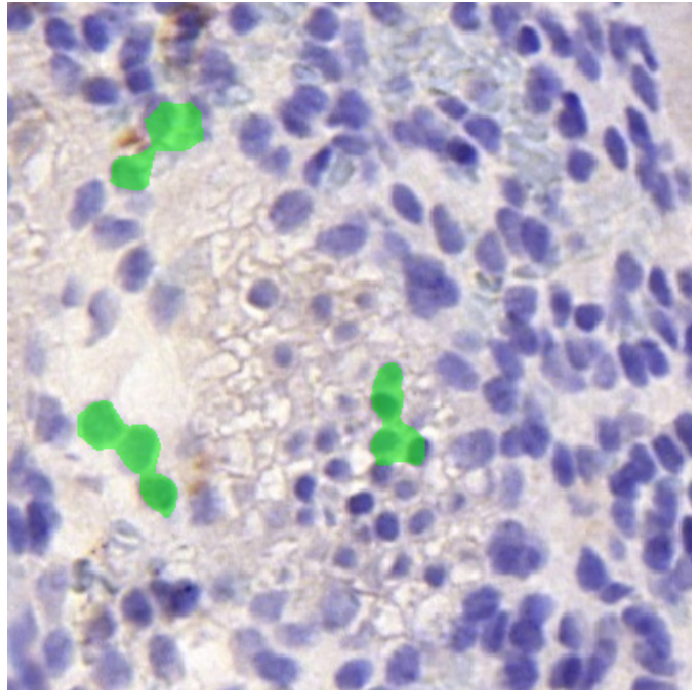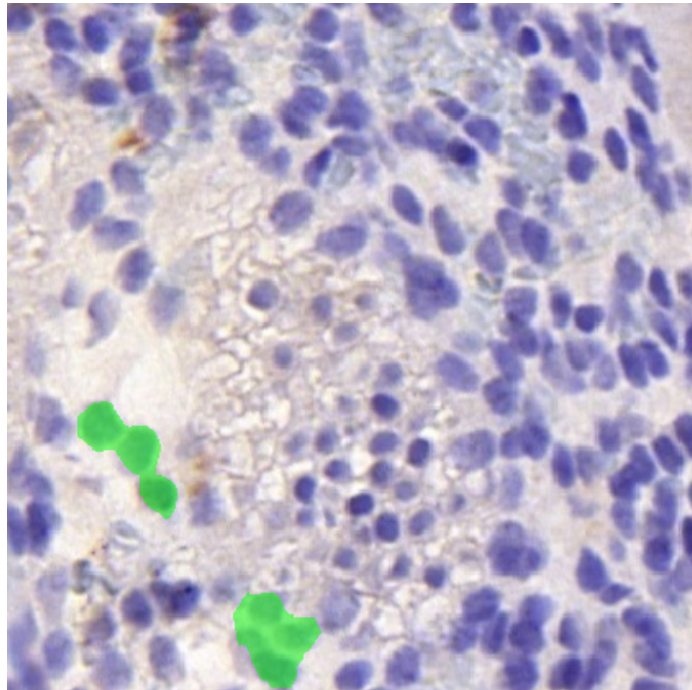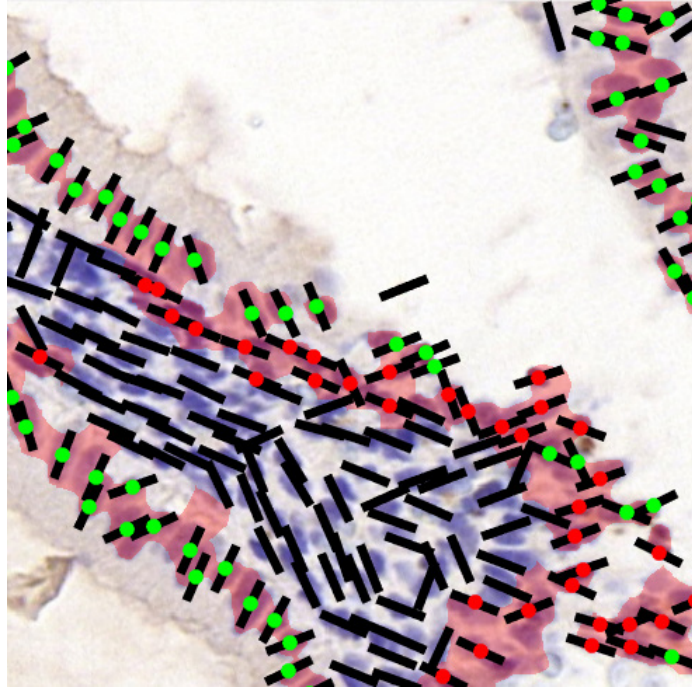
(a)
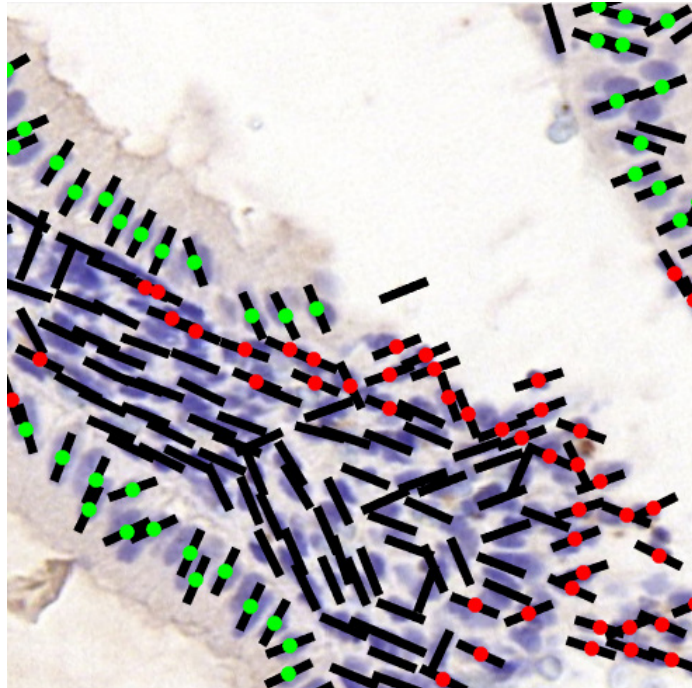
(b)

Figure 5.17: (a) and (b) show the classification results of Figure 5.15(a) using the MR-COrCo and MR-LBCOrCo descriptors, respectively. Black bars depict cell orientations, red dots depict the cells classified as non-epithelial cells, and green dots depict the cells classified as epithelial cells.
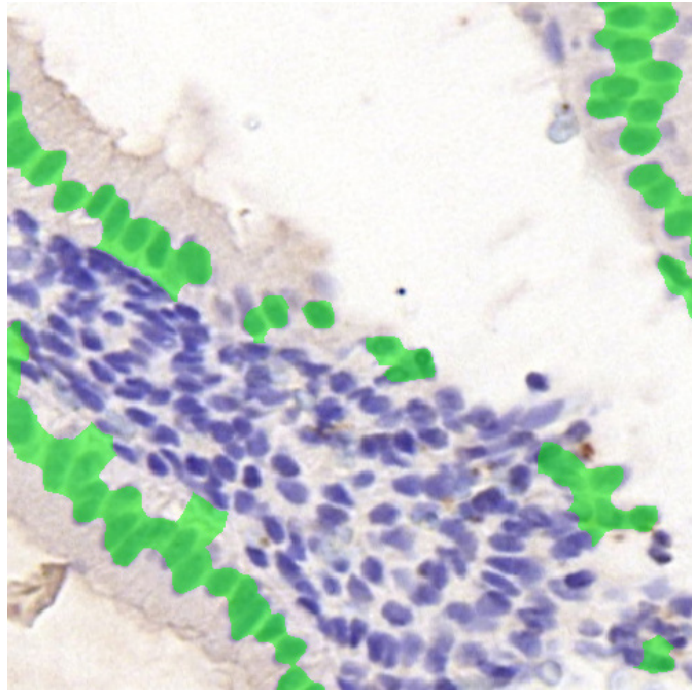
(a)
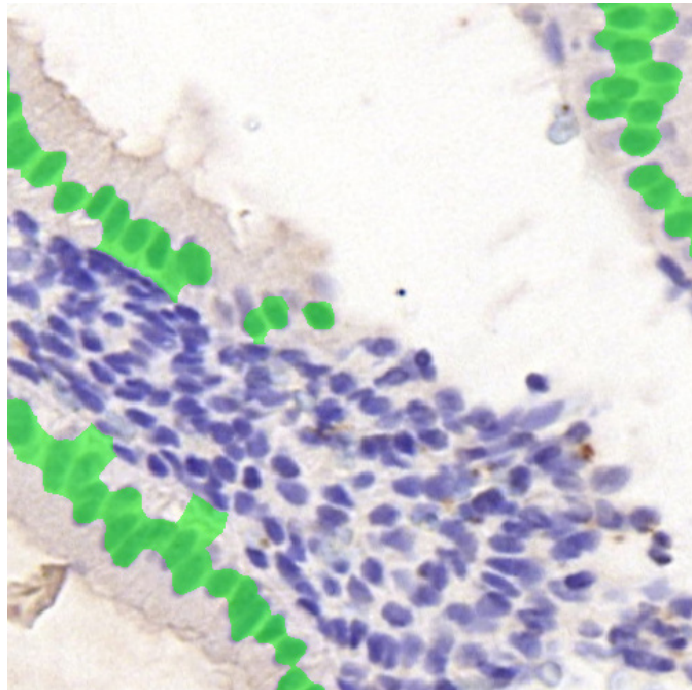
(b)

Figure 5.18: (a) and (b) show the segmentation results of Figure 5.15(a) using the MR-COrCo and MR-LBCOrCo descriptors, respectively. Black bars depict cell orientations

in the segmentation, which is shown in 5.18 (a). In the epithelium segmentation result (shown in 5.18 (b)) using the MR-LBCOrCo descriptor, we observe that most of the stromal cell regions, which are previously classified as potential epithelial, are finally remove from the segmentation.

In summary, the experimental results show that the MR-COrCo and MR-LBCOrCo descriptor performance well in the segmentation of glandular epithelium, and the MR-LBCOrCo descriptor can also accurately segment luminal epithelium , but the MR-COrCo descriptor starts showing slight difficulty in correctly representing cell orientation congruence of the cells from luminal epithelium. The state-of-the-art methods assume that glandular epithelium has an enclosed boundary, but luminal epithelium is normally curves/lines and not part of a glandular structure, as shown in Figure 5.15 (a). Therefore, all the state-of-the-art methods performance poorly on segmenting luminal epithelium.

5.4.4 Discussion

To the best of our knowledge, the proposed COC descriptor based approach is the first one for detecting epithelial cell and segmenting epithelium in endometrial tissue. Epithelium segmentation approaches are based on existing gland segmentation methods, which generally first attempt to segment glandular structure as enclosed objects and then extract from it the glandular epithelium. The existing state-of-the-art gland segmentation methods generally solve the problem by using colour/textural features of different cell region or/and structural information of glandular structures and other objects/backgrounds. However, epithelial cell region and stromal cell region in endometrial tissue have strong similarity in terms of colour/textural features. Therefore, these methods are commonly faced with the difficulty of differentiating between stromal and epithelial cells when the colour/textural features of the cells are employed in the cell classification. Moreover, both of glands and epithelium in endometrial tissue show a variety of irregular

structures/appearances.

The variance filter in [126] is proposed to generate different textural features for lumen regions and cell clusters so that different image regions can be clustered/segmented based their textural features. his method shows a strong availability of segmenting lumen, cell and background regions from the image, it is not capable of differentiating between different cell regions due to their same textural features generated by the variance filter. Although epithelial cells are packed at the boundaries of lumen or tissue regions, both glandular and luminal epithelium in endometrial tissue are constructed by one or more layers of epithelial cells with different sizes and morphologies, which are characterized by inconsistent thickness and morphology. In addition, stromal cells are also sometimes packed at the boundaries of tissue regions. Therefore, epithelium can be hardly differentiated based on their location information after the segmentation by the variance filter. The proposed solution computes a novel local orientation congruence of cell region and it is successfully used to differentiate between different cell regions located at the boundaries of lumen or tissue in endometrial pathology images.

A Bayesian classifier proposed in [123] first locates potential luminal areas and then initialised a level set curve on the boundaries of potential luminal areas to finalise the segmentation of glandular structures. This method often identify large cytoplasm areas between stromal cells as luminal areas due to their strong similarity in terms of colour/texture. Therefore, the level set curves are also initialised on the boundaries of large cytoplasm areas, which causes that these non-luminal areas are mistakenly segmented as glandular structures and stromal cells packed at the boundaries of the large cytoplasm areas are extracted and mistakenly identified as epithelial cells. In addition, the boundaries of glandular structures in endometrial tissue are made of epithelial cell clusters which have a variety of complex morphologies and inconsistent textures, thus the level set based methods cannot accurately approximate the boundaries of glandular structures in endometrial tissue. Con-

133

sequently, the following epithelium extraction may obtain incomplete epithelium or non-epithelial regions based on the approximated boundaries of the glandular structures. Our proposed method attempts to utilise the classified epithelial cells to achieve the epithelium segmentation, which avoids a dependency on the inaccurately approximated boundaries of glandular structures.

Colour space analysis is used in [124] to label glandular components, i.e., epithelial cell nuclei, cytoplasm and lumen. The labelled glandular components are used to constitute glandular structure to achieve the segmentation. The problem of this method is similar to of the Bayesian classifier in [123], colour feature can neither differentiate between epithelial and stromal cell nuclei, nor between lumen and large cytoplasm/background. In comparison, the proposed cell orientation congruence feature shows better performance on classifying epithelial cells. It is also worthy mentioning that our proposed epithelial cell classification method can be integrated with the gland segmentation methods based on organisational information of the glandular structures, which may solve the segmentation problem for these images which look similar to endometrial pathology images.

The gland segmentation method proposed in [131] decomposed an endometrial pathology image into set of circular objects, which either depict nuclei or lumen/cytoplasm regions. Glands are segmented making use of the organizational properties of the circular objects, which are quantified with the definition of object-graphs constructed by these objects. This approach employs the structural information, instead of using the pixel-based information alone for the gland segmentation. It overcomes the problem of incorrect gland segmentation due to that cells, cytoplasm, or/and lumen regions in endometrial tissue, are often misclassified by [126], [123] and [124]. However, only one organizational model is used in [131] for glands and it is pre-defined. But the glands in endometrial tissue have a variety of different structures so that their structural information cannot be comprehensively described by singular and pre-defined organizational model. Therefore, the method proposed

in [131] occasionally miss initialise segmentation at some of the glands. In addition, the organization of the circular object depicting large cytoplasm or background regions and their nearby circular objects depicting nuclei may also exhibit like a glandular structure, which causes this method also attempt to initialise gland segmentation at these large cytoplasm/background regions. In contrast, our proposed approach employs the local cell orientation information to classify the epithelial cells, which potentially avoids the above cell classification problem in [131].

Random Polygons Model (RPM) proposed in [132] is also an unique gland segmentation method in terms of methodology. The RPM approximates the boundary of glandular structure by fitting polygon made of a random number of vertices which represents the location of epithelial cell nuclei. One evident advantage of the RPM is that neither morphological information nor textural feature of the epithelial cells are employed in term of the methodology, i.e., it can cope with morphological and textural irregularity of the boundaries of glandular structures in endometrial tissue, compared with the level set curve in [123]. However, the disadvantage of RPM is also obvious, i.e., polygon fitting is relatively high computational complexity and the cost increases dramatically for the polygons (glandular structures) with more number of vertices (epithelial cells). The computational cost of the RPM is especially an issue for glandular structure in endometrial tissue due their epithelial boundaries are normally made of a significant number of cells, it takes several minutes to approximate the epithelial boundary made of one individual glandular structure with hundreds of epithelial cells. In contrast, the proposed COC descriptors are much less computational complexity, which is shown in the experiment section.

In conclusion, it is difficult to accurately obtain epithelium based on the boundaries of segmented glandular structures for the above gland segmentation methods. It is due to that the epithelium are occasionally discontinued crust formed by a number of layers of epithelial cells, which are therefore characterized by strong

135

inhomogeneity, e.g., inconsistent morphology and thickness. Our proposed epithelium segmentation method attempts to classify the epithelial cells and then finalises the epithelium segmentation by the superpixel regions containing the classified epithelial cells. More importantly, the above methods are restricted in segmenting glandular epithelium only from the segmented glands, whereas removal of luminal epithelium is also necessary for the cell counting in endometrial tissue. In comparison, the cell orientation congruence based approach is capable of simultaneously segmenting both types of epithelium in general.

The methodology of Cell Orientation Entropy (COrE) in [134] are similar to that of our proposed method, which also aims to qualitatively model the cell orientation and then employ it as a feature for the cell classification. A major difference between COrE and the COC descriptors is that COrE performs Principle Component Analysis (PCA) on nucleus boundaries to compute cell orientations. It is difficult to achieve accurate boundary of individual epithelial cell nucleus in endometrial tissue since the nuclei are densely grouped together and normally overlapped. The active contour is used in COrE to generate the nucleus boundaries, which faces with the problems of accurately positioning initial contour (detecting nucleus position) and high computational cost. The COC descriptors estimate the cell orientation of a detected cell on a set of sampled pixels from its nucleus regions, which does not require cell/nucleus segmentation and are therefore accurate and also much less computational complexity.

The COC descriptors also can be extend to cancer diagnosis and grading, provide an important and reliable cell orientation measurement for the classification of disoriented cancerous cells. For example, prostate cancer is fundamentally a disease regarding to glandular disorganization. In the healthy prostate glands, the neighbouring epithelial cells align themselves with a coherent directionality toward to the lumen centre. However, the cancerous prostate gland has a disordered organization, which causes that the surrounding epithelial cells display a disoriented

arrangement. Therefore, the breakdown in cancerous epithelial cell orientation is directly related to the grade of prostate cancer [137]. The COC descriptors can be used to yield a characterization of the cell disorientation in prostate glands for both identification of the tumour regions and measuring the degree of prostate cancer aggressiveness.

The methods proposed in Chapter 4 and 5 comprise are specially designated for the endometrial pathology images which are cropped by our collaborators from the marginal regions (edges) of endometrial tissue in whole slide images. Therefore, although these methods comprise an automatic cell counting solution for endometrial pathology images, it is strongly advisable for users to manually select the input images in practice., rather than automatically cropping random image regions from the whole slide images or even use the entire whole slide image as the input image.

It is also important to deal with legal and ethical issues of applying the proposed automatic pathology image analysis solution in clinic diagnosis.The patients must be informed that the diagnosis will be partially relied on the assistance of an automatic pathology image analysis system, and they can ask a comparison between the results respectively produced by the automatic system and the pathology experts. More importantly, although the pathology experts can explain to the patients that the automatic system is more accurate and efficient than manual image analysis, the patients still have the right to decide whether the automatic system can be involved in the diagnosis. Moreover, the automatic system and its developers should not bear any legal liability if the patients are given false diagnostic result while employing the automatic system to assist the diagnosis. This is because that the automatic system are only used to produce the information required by the diagnosis, and the final diagnostic decision are made by the pathology experts rather than the automatic system.

5.5 Summary

In this chapter, We presented a variety of cell orientation congruence descriptors for solving the problem of simultaneously segmenting both luminal and glandular epithelium in endometrial histology images. The proposed descriptors is designated to discriminate between epithelial and stromal cells based on the observation of that the epithelial cells in the normal endometrium are packed such that their orientation is more or less similar to their neighbouring cells along certain directions, whereas neighbouring stromal cells are packed in entirely different pattern. We proposed two novel locality sensitive models for the descriptors for the computation of the cell orientation pattern of local cell neighbourhood. We examined the performance of the proposed descriptors and concluded that the MR-COrCo and MR-LBCOrCo descriptors yielded the best results with relatively low computational cost. In addition, the MR-COrCo and MR-LBCOrCo descriptors were compared with 5 state-of-the-art methods in two different experiments. The experimental results show that the MR-LBCOrCo descriptors attains a superior epithelium segmentation accuracy, particularly on simultaneously segmenting both luminal and glandular epithelium.

Chapter 6

Conclusions and Future Directions

In recent years, biomedical imaging has been widely applied as a primary analysis tool for cell biology, pathology research and clinical diagnosis, thanks to the rapid improvements in digital imaging facilities and computational power. Biomedical imaging techniques brings the scientists gigantic image data regarding to the biomedical information, e.g.,s molecular events in living or cell conditions in tissue biopsy on a daily basis. In the meanwhile, computer science community has proposed a large number of powerful image processing algorithms to cope with the problems raised in the automatic analysis of digital biomedical images. The work was motivated by several unsolved unique challenges in the automatic tracking of Myosin VI spots in TIRFM sequences and the cell counting in endometrial histology images. In this thesis, we presented several image anasyis algorithms based on novel locality sensitive modelling, which can serve as fundamental building units to develop the computer-aided automatic systems for quantitatively processing large scale datasets of TIRFM sequences and endometrial histology. This chapter concludes the achievements presented in this thesis, and also discusses several possible future research directions.

6.1 Chapter Summaries

In Chapter 1, we introduced the importance of biomedical imaging as it is a powerful visualisation toolbox for studying cell biology, pathology research and clinical diagnosis, and mentioned the solutions for automatic biomedical image analysing are pressing demands from the researchers. We also discussed the common tasks in biomedical image processing, e.g., detection, tracking and segmentation of biological structures. We also discussed some particular challenges of object analysis, and indicated that temporal and spatial relationships between neighbouring objects in local regions can be modelled as a sort of relational features using locality sensitive modelling, which offers a crucial clue to confront these challenges. We also briefly summarised the main contributions of the work in Chapter 1.

Chapter 2 introduced the basic workflow of the proposed multi-target tracking framework for Myosin VI spots in TIRFM sequences, which consists of 3 stages: (1) pre-processing, (2) spot detection, and (3) spot tracking. In Chapter 2, we focused on presenting the stages (1) and (2), and the algorithms regrading to the stage (3) was presented in Chapter 3. We first briefly reviewed several pre-processing techniques, e.g., image enhancement and image denoising method, and discussed several popular methods of detecting spots in fluorescence microscopy. We then proposed a pre-processing stage including a 3D wavelet based image denoising method to reduce the background noise, and a Kalman filter followed a Difference of Gaussian (DoG) filter to enhance the visibility of fluorescent spots. In the spot detection stage, bright objects that resemble dome-like structures were first detected by H-dome transform and then classified as either noises or fluorescent spots using a spot appearance modelling approach. We also presented a method of generating synthetic TIRFM sequences of Myosin VI proteins moving along Actin filaments: the appearances (intensities) of spots were modelled using a 2D Gaussian models, Actin filaments was generated as a strip of connected curve segments approximated using

cubic B-Spline curve fitting. We evaluated the proposed spot detection method on both real and synthetic TIRFM sequences and the experimental results shown that the proposed method attained high precision and recall values, which can provide accurate spot locations for the spot tracking.

Chapter 3 first reviewed several state-of-art methods for tracking fluorescent spots in microscopy sequences and then presented a multi-target spot tracking framework for analysing the dynamics of Myosin VI proteins in TIRFM sequences. Two synergistic components were proposed in the algorithm: an extended Hungarian algorithm and an IMM filter with two motion models. The Hungarian algorithm was extended by a locality sensitive model, which helped to solve the data association (measurement-to-target and estimation-to-target assignment) problems, commonly encountered when tracking multiple targets, and an IMM filter which was installed with two motion models to approximate the non-linear dynamics of Myosin VI proteins. The locality sensitive model was introduced together with imaginary spots in the Hungarian algorithm, which forced the spots to be associated within a spatio-temporal local neighbourhood to prevent possible assignment between two distant spots even under the global association manner of the Hungarian Algorithm. The imaginary spots not only overcame the limitation of bijective mapping of the Hungarian algorithm, but also helped the proposed spot tracking method to preserve spot trajectories when no corresponding spot matching/measurement on next frame due to spot overlapping or temporal disappearing.

We quantitatively evaluated the prospered spot tracking framework against three publicly available state-of-the-art methods using an OSPA error metric on real one-channel and two-channel TIRFM sequences, and also the synthetically generated one-channel TIRFM sequences. The experimental results shown that the accuracy of the proposed spot tracking framework is higher than that of the state-of-the-art methods on both synthetic and real TIRFM sequences of Myosin VI protein. We discovered that an hypothesis can be made on the movements of Myosin VI proteins

on Actin filament, i.e., their motion is a composite of unbound, freely diffusing and weakly bound diffusive motion trapped by a fixed structure (Actin filament), base on the MSD of expert manually marked ground truth. MSD is commonly used in analysing the biophysics of particles to determine motion modes of the fluorescent spots over a period of time. Therefore, we employed a MSD based evaluation method to quantify the similarities between hand-marked tracks and those produced by all the evaluated methods. The results shown that the spot tracks captured by the proposed tracking framework exhibited the similar motion pattern as the Ground Truth. We finally concluded that the can more accurately capture the movements of Myosin VI proteins on Actin filament than the other three methods, which can therefore help the researchers to better understand the role of Myosin VI proteins in intracellular transportation.

In Chapter 4, we first discussed several popular techniques of cell detection in histology images. Then we proposed a complete solution to effectively detect stromal and UNK cells in H&DAB stained endometrial histology images, including a localisation method which marks luminal epithelium to removing irrelevant cell detections. The cells in endometrial histology can be considered as symmetric elliptical blobs where a peak of isotropic symmetry is shown near to the blob centre. We improved a feature detection method called LIPSyM which is based on detecting isotropic symmetry peaks to detect the cell nuclei in endometrial histology images. LIPSyM often detects multiple peaks resulting in redundant detections at the overlapping or elongated cells, therefore we presented a locality sensitive model acted as a probe to search redundant detections. UNK cells are those covered by the DAB stained brown areas, we proposed a h-maxima transform to suppress high intensity areas on the DAB channel, while keeping the lower intensity areas corresponding to the DAB stained brown areas (UNK cell nucleus regions). We also presented an alpha shapes method which was used to classify those cell detection corresponding to epithelial cells, and also a localisation method which approximates cubic B-Spline

142

curve on the classified epithelial cell detection to mark luminal epithelium. We evaluated the proposed cell detection, luminal epithelium localisation methods, and the cell counting module designed for the endometrial histology of a commercial cloud application, called VIS which is developed by Visiopharm, on high resolution (around 1000×1500 pixel) image regions captured from the HPFs of whole slide images. The evaluation result proven that the proposed methods attained accurate cell detection and luminal epithelium localisation than VIS. The localisation method is also an essential and preliminary approach or automatic cropping image region near tissue edges from the whole slide images, since the cell counting is preferably perform on the regions near tissue edges.

In Chapter 5, we briefly reviewed several state-of-art methods for segmenting glandular structures in digital histology images, which can be also used for segmenting glandular epithelium in endometrial histology images. Next, we proposed a variety of scale-rotational invariant descriptors which can discriminate between epithelial and stromal cells for simultaneously segmenting both luminal and glandular epithelium in endometrial histology images. The descriptors were proposed based on the observation of that the neighbouring epithelial cells in normal endometrium are densely packed in parallel (their orientations are more or less similar) at the boundaries of glandular structures and tissue regions, whereas stromal cells are loosely distributed and exhibit inconsistent orientations in a local region. We proposed two different locality sensitive models for the descriptors to compute the orientation congruence of neighbouring cells. One of the models was used in the COrCo and MR-COrCo descriptors, which has the strength of expressing an average of the orientation difference between cells and each of their neighbours, and the other used in the LBCOrCo and MR-LBCOrCo descriptors is adept in emphasising the similarity between the average orientation of the neighbouring cells packed along the different directional regions. We evaluated the top-two of the proposed descriptors against five state-of-the-art segmentation methods in two different experiment, the experi-

mental results shown that the proposed descriptors attained higher accuracy than other state-of-the-art methods, especially MR-LBCOrCo descriptor performed superiorly in segmenting luminal epithelium in where other methods commonly failed.

6.2   Future Directions

The algorithms proposed in this thesis still remains in the experimental stage, but it ultimately aims at serving as the core modules of the automatic image analysis systems, which can be used in practice and on a daily basis. Although the experiments showed that the proposed algorithms yielded satisfactory results, several limitations were observed and must be overcame before deploying them in practice. We will discuss the current limitations and several possible direction to improve the proposed algorithms in the following.

For the real two-channel TIRFM sequences, we observed that Myosin VI spots on the Actin filaments tend to move smoothly with an average velocity of 2.6μm/s (0.8 pixel/frame). Therefore, one of the primary task in the future work, is to take into account of the velocity difference between real Myosin VI and noisy spots, to remove the spots with abnormal velocities from the tracking. This work can be very useful for preventing a spot on an Actin filament matching with a noisy spot with much lower/higher velocity that moves close to, but not on, the same Actin filament. In this work, we had a quite few resources regarding to the TIRFM sequences of Myosin VI proteins on Actin filaments, which caused the comprehensive observation and understanding of the motion pattern of Myosin VI protein on Actin filaments very difficult. Consequently, the motion models used in IMM filter and the parameters tuned in the proposed locality sensitive model were suboptimal, therefore examining more motion models on a large dataset is also one of the primary task in the future work.

In endometrial histology, although the improved LIPSyM can remove most

redundant cell detection, it is an unsupervised method relying on the symmetric feature, which showed a strong weakness on detecting the cells with faint, blurred, broken or less symmetric shapes/appearances. The supervised methods, e.g., Convolutional Neural Networks (CNNs)[138] [139], have recently became the most popular and powerful approach for detecting and classifying the objects with a variety of complex shapes/appearances. Several CNNs based cell detection methods [140] [141] [142] showed that CNNs performed excellently for many different types of digital pathology images. CNNs were inspired by the biological processes of human brain [143], which normally consist of multilayer perceptrons (neurons) which are responsible for detecting the cells located in the corresponding small image portions [144]. However, CNNs report redundant detections when a cell appears multiple times in different small image portions, thus the proposed locality sensitive model used for improving LIPSyM can also be used to remove the redundant detections reported by CNNs.

The proposed descriptors can fail when stromal cells exhibit similar orientation congruence as epithelial cells. A more reliable solution is to classify between stromal and epithelial cell regions using the cell orientation congruences together with the textural features. This solution is feasible due to that the epithelial cells are densely packed with similar orientation to each other as a strip along the lumen/tissue boundaries, whereas it is hard to conclude certain arrangement and feature patterns for stromal cell clusters, since the stromal cells are more loosely distributed with random orientations. The proposed descriptors can hardly obtain the segmentation of the "Hive-like" epithelial structures, which has already been addressed in Chapter 5. Therefore, another important task in the future work is to develop a solution for segmenting the "Hive-like" epithelial structures using machine learning techniques, e.g., CNNs, which show many particular advantages due to the characteristics of bionics, on capturing and learning the complex structural and textural appearances of the "Hive-like" epithelial structure.

We intend to further validate the proposed descriptors on variety of large datasets of cancer and non-cancer histology images. We also attempt to extend the present work in those cancer diagnosis relied on epithelial cell analysis (abnormal cells are likely to be disoriented in cancer tissues). In addition, an optional work in the future is to efficiently parallelise the computation of the proposed descriptors.

Bibliography

[1] User and reference manual 4.4 - 2d alpha shapes. `http://doc.cgal.org/latest/Alpha_shapes_2/index.html`. Accessed: 2014-09-30.

[2] Franklyn G Prendergast and Kenneth G Mann. Chemical and physical properties of aequorin and the green fluorescent protein isolated from aequorea forskalea. *Biochemistry*, 17(17):3448–3453, 1978.

[3] Roger Y Tsien. The green fluorescent protein. *Annual Review of Biochemistry*, 67(1):509–544, 1998.

[4] Jennifer Lippincott-Schwartz and George H Patterson. Development and use of fluorescent protein markers in living cells. *Science*, 300(5616):87–91, 2003.

[5] Atsushi Miyawaki, Asako Sawano, and Takako Kogure. Lighting up cells: labelling proteins with fluorophores. *Nat Cell Biol*, 2003.

[6] Nathan C Shaner, Paul A Steinbach, and Roger Y Tsien. A guide to choosing fluorescent proteins. *Nature Methods*, 2(12):905–909, 2005.

[7] James A Spudich and Susan Watt. The regulation of rabbit skeletal muscle contraction i. biochemical studies of the interaction of the tropomyosin-troponin complex with actin and the proteolytic fragments of myosin. *Journal of Biological Chemistry*, 246(15):4866–4871, 1971.

[8] Ivan Rayment, Hazel M Holden, Michael Whittaker, Christopher B Yohn,

147

Michael Lorenz, Kenneth C Holmes, and Ronald A Milligan. Structure of the actin-myosin complex and its implications for muscle contraction. *Science*, 261(5117):58–65, 1993.

[9] Margaret Clarke and James A Spudich. Nonmuscle contractile proteins: the role of actin and myosin in cell motility and shape determination. *Annual Review of Biochemistry*, 46(1):797–822, 1977.

[10] Ronald S Rock, Sarah E Rice, Amber L Wells, Thomas J Purcell, James A Spudich, and H Lee Sweeney. Myosin vi is a processive motor with a large step size. *Proceedings of the National Academy of Sciences*, 98(24):13655–13659, 2001.

[11] Amber L Wells, Abel W Lin, Li-Qiong Chen, Daniel Safer, Shane M Cain, Tama Hasson, Bridget O Carragher, Ronald A Milligan, and H Lee Sweeney. Myosin vi is an actin-based motor that moves backwards. *Nature*, 401(6752): 505–508, 1999.

[12] Folma Buss, Giulietta Spudich, and John Kendrick-Jones. Myosin vi: cellular functions and motor properties. *Annu. Rev. Cell Dev. Biol.*, 20:649–676, 2004.

[13] Antoni Buades, Bartomeu Coll, and Jean-Michel Morel. A review of image denoising algorithms, with a new one. *Multiscale Modeling & Simulation*, 4 (2):490–530, 2005.

[14] Stefan W Hell and Jan Wichmann. Breaking the diffraction resolution limit by stimulated emission: stimulated-emission-depletion fluorescence microscopy. *Optics Letters*, 19(11):780–782, 1994.

[15] X Rong Li and Yaakov Bar-Shalom. Tracking in clutter with nearest neighbor filters: analysis and performance. *Aerospace and Electronic Systems, IEEE Transactions on*, 32(3):995–1010, 1996.

[16] Lngemar J Cox and Sunita L Hingorani. An efficient implementation of reid's multiple hypothesis tracking algorithm and its evaluation for the purpose of visual tracking. *Pattern Analysis and Machine Intelligence, IEEE Transactions on*, 18(2):138–150, 1996.

[17] Tat-Jen Cham and James M Rehg. A multiple hypothesis approach to figure tracking. In *Computer Vision and Pattern Recognition, 1999. IEEE Computer Society Conference on.*, volume 2. IEEE, 1999.

[18] Samuel S Blackman. Multiple hypothesis tracking for multiple target tracking. *Aerospace and Electronic Systems Magazine, IEEE*, 19(1):5–18, 2004.

[19] Thomas E Fortmann, Yaakov Bar-Shalom, and Molly Scheffe. Sonar tracking of multiple targets using joint probabilistic data association. *Oceanic Engineering, IEEE Journal of*, 8(3):173–184, 1983.

[20] Kuo-Chu Chang and Yaakov Bar-Shalom. Joint probabilistic data association for multitarget tracking with possibly unresolved measurements and maneuvers. *Automatic Control, IEEE Transactions on*, 29(7):585–594, 1984.

[21] Christopher Rasmussen and Gregory D Hager. Probabilistic data association methods for tracking complex visual objects. *Pattern Analysis and Machine Intelligence, IEEE Transactions on*, 23(6):560–576, 2001.

[22] Dirk Schulz, Wolfram Burgard, Dieter Fox, and Armin B Cremers. People tracking with mobile robots using sample-based joint probabilistic data association filters. *The International Journal of Robotics Research*, 22(2):99–116, 2003.

[23] Cor J Veenman, Marcel JT Reinders, and Eric Backer. Resolving motion correspondence for densely moving points. *Pattern Analysis and Machine Intelligence, IEEE Transactions on*, 23(1):54–72, 2001.

[24] Khuloud Jaqaman, Dinah Loerke, Marcel Mettlen, Hirotaka Kuwata, Sergio Grinstein, Sandra L Schmid, and Gaudenz Danuser. Robust single-particle tracking in live-cell time-lapse sequences. *Nature Methods*, 5(8):695–702, 2008.

[25] Chang Huang, Bo Wu, and Ramakant Nevatia. Robust object tracking by hierarchical association of detection responses. In *Computer Vision–ECCV 2008*, pages 788–801. Springer, 2008.

[26] Joao F Henriques, Rui Caseiro, and Jorge Batista. Globally optimal solution to multi-object tracking with merged measurements. In *Computer Vision (ICCV), 2011 IEEE International Conference on*, pages 2470–2477. IEEE, 2011.

[27] Zhen Qin and Christian R Shelton. Improving multi-target tracking via social grouping. In *Computer Vision and Pattern Recognition (CVPR), 2012 IEEE Conference on*, pages 1972–1978. IEEE, 2012.

[28] Rudolph Emil Kalman. A new approach to linear filtering and prediction problems. *Journal of Fluids Engineering*, 82(1):35–45, 1960.

[29] Simon J Julier and Jeffrey K Uhlmann. New extension of the kalman filter to nonlinear systems. In *AeroSense'97*, pages 182–193. International Society for Optics and Photonics, 1997.

[30] Eric Wan and Ronell Van Der Merwe. The unscented kalman filter for nonlinear estimation. In *Adaptive Systems for Signal Processing, Communications, and Control Symposium 2000. AS-SPCC. The IEEE 2000*, pages 153–158. IEEE, 2000.

[31] M Sanjeev Arulampalam, Simon Maskell, Neil Gordon, and Tim Clapp. A tutorial on particle filters for online nonlinear/non-gaussian bayesian tracking. *Signal Processing, IEEE Transactions on*, 50(2):174–188, 2002.

[32] Henk AP Blom and Yaakov Bar-Shalom. The interacting multiple model algorithm for systems with markovian switching coefficients. *Automatic Control, IEEE Transactions on*, 33(8):780–783, 1988.

[33] Metin N Gurcan, Laura E Boucheron, Ali Can, Anant Madabhushi, Nasir M Rajpoot, and Bulent Yener. Histopathological image analysis: A review. *Biomedical Engineering, IEEE Reviews in*, 2:147–171, 2009.

[34] David RJ Snead, Yee-Wah Tsang, Aisha Meskiri, Peter K Kimani, Richard Crossman, Nasir M Rajpoot, Elaine Blessing, Klaus Chen, Kishore Gopalakrishnan, Paul Matthews, et al. Validation of digital pathology imaging for primary histopathological diagnosis. *Histopathology*, 2015.

[35] Siobhan Quenby, Helena Nik, Barbara Innes, Gendie Lash, Mark Turner, Jo Drury, and Judith Bulmer. Uterine natural killer cells and angiogenesis in recurrent reproductive failure. *Human Reproduction*, 24(1):45–54, 2009.

[36] Keiji Kuroda, Radha Venkatakrishnan, Sean James, Sandra Šućurović, Biserka Mulac-Jericevic, Emma S Lucas, Satoru Takeda, Anatoly Shmygol, Jan J Brosens, and Siobhan Quenby. Elevated periimplantation uterine natural killer cell density in human endometrium is associated with impaired corticosteroid signaling in decidualizing stromal cells. *The Journal of Clinical Endocrinology & Metabolism*, 98(11):4429–4437, 2013.

[37] Ai-Wei Tang, Zarko Alfirevic, Mark A Turner, Jo A Drury, Rachel Small, and Siobhan Quenby. A feasibility trial of screening women with idiopathic recurrent miscarriage for high uterine natural killer cell density and randomizing to prednisolone or placebo when pregnant. *Human Reproduction*, 28(7): 1743–1752, 2013.

[38] Jung-Chi Liao, Mary Williard Elting, Scott L Delp, James A Spudich, and Zev Bryant. Engineered myosin vi motors reveal minimal structural determinants

of directionality and processivity. *Journal of Molecular Biology*, 392(4):862–867, 2009.

[39] Tariq Butt, Tabish Mufti, Ahmad Humayun, Peter B Rosenthal, Sohaib Khan, Shahid Khan, and Justin E Molloy. Myosin motors drive long range alignment of actin filaments. *Journal of Biological Chemistry*, 285(7):4964–4974, 2010.

[40] Riccardo AG Cinelli, Aldo Ferrari, Vittorio Pellegrini, Mudit Tyagi, Mauro Giacca, and Fabio Beltram. The enhanced green fluorescent protein as a tool for the analysis of protein dynamics and localization: Local fluorescence study at the single-molecule level. *Photochemistry and Photobiology*, 71(6):771–776, 2000.

[41] Daniel Axelrod. Total internal reflection fluorescence microscopy. *Methods Cell Biol*, 30:245–270, 1989.

[42] Herbert Schneckenburger. Total internal reflection fluorescence microscopy: technical innovations and novel applications. *Current Opinion in Biotechnology*, 16(1):13–18, 2005.

[43] Jonathan A Hern, Asma H Baig, Gregory I Mashanov, Berry Birdsall, John ET Corrie, Sebastian Lazareno, Justin E Molloy, and Nigel JM Birdsall. Formation and dissociation of m1 muscarinic receptor dimers seen by total internal reflection fluorescence imaging of single molecules. *Proceedings of the National Academy of Sciences*, 107(6):2693–2698, 2010.

[44] GI Mashanov and JE Molloy. Automatic detection of single fluorophores in live cells. *Biophysical Journal*, 92(6):2199–2211, 2007.

[45] Jonas F Dorn, Gaudenz Danuser, and Ge Yang. Computational processing and analysis of dynamic fluorescence image data. *Methods in Cell Biology*, 85: 497–538, 2008.

[46] Daniel Gerlich and Jan Ellenberg. 4d imaging to assay complex dynamics in live specimens. *Nature Cell Biology*, pages S14–9, 2003.

[47] Erik Meijering, Ihor Smal, and Gaudenz Danuser. Tracking in molecular bioimaging. *Signal Processing Magazine, IEEE*, 23(3):46–53, 2006.

[48] Yuval Garini, Bart J Vermolen, and Ian T Young. From micro to nano: recent advances in high-resolution microscopy. *Current Opinion in Biotechnology*, 16 (1):3–12, 2005.

[49] Jean-Christophe Olivo-Marin. Extraction of spots in biological images using multiscale products. *Pattern Recognition*, 35(9):1989–1996, 2002.

[50] Auguste Genovesio, Tim Liedl, Valentina Emiliani, Wolfgang J Parak, Maité Coppey-Moisan, and Jean-Christophe Olivo-Marin. Multiple particle tracking in 3-d+ t microscopy: method and application to the tracking of endocytosed quantum dots. *Image Processing, IEEE Transactions on*, 15(5):1062–1070, 2006.

[51] Bo Zhang, MJ Fadili, Jean-Luc Starck, and J-C Olivo-Marin. Multiscale variance-stabilizing transform for mixed-poisson-gaussian processes and its applications in bioimaging. In *Image Processing, 2007. ICIP 2007. IEEE International Conference on*, volume 6, pages VI–233. IEEE, 2007.

[52] Qiang Wu, Fatima Merchant, and Kenneth Castleman. *Microscope image processing*. Academic press, 2010.

[53] Ihor Smal, Katharina Draegestein, Niels Galjart, Wiro Niessen, and Erik Meijering. Rao-blackwellized marginal particle filtering for multiple object tracking in molecular bioimaging. In *Information Processing in Medical Imaging*, pages 110–121. Springer, 2007.

[54] Ihor Smal, Erik Meijering, Katharina Draegestein, Niels Galjart, Ilya Grigoriev, Anna Akhmanova, ME Van Royen, Adriaan B Houtsmuller, and Wiro Niessen. Multiple object tracking in molecular bioimaging by rao-blackwellized marginal particle filtering. *Medical Image Analysis*, 12(6):764–777, 2008.

[55] Ihor Smal, Katharina Draegestein, Niels Galjart, Wiro Niessen, and Erik Meijering. Particle filtering for multiple object tracking in dynamic fluorescence microscopy images: Application to microtubule growth analysis. *Medical Imaging, IEEE Transactions on*, 27(6):789–804, 2008.

[56] Derya Birant and Alp Kut. St-dbscan: An algorithm for clustering spatial–temporal data. *Data & Knowledge Engineering*, 60(1):208–221, 2007.

[57] EJ Breen, GH Joss, and KL Williams. Locating objects of interest within biological images: The top hat box filter. *J Comput-Assist Microsc*, 3:97–102, 1991.

[58] D Thomann, DR Rines, PK Sorger, and G Danuser. Automatic fluorescent tag detection in 3d with super-resolution: application to the analysis of chromosome movement. *Journal of Microscopy*, 208(1):49–64, 2002.

[59] Daniel Sage, Franck R Neumann, Florence Hediger, Susan M Gasser, and Michael Unser. Automatic tracking of individual fluorescence particles: application to the study of chromosome dynamics. *Image Processing, IEEE Transactions on*, 14(9):1372–1383, 2005.

[60] Shan Jiang, Xiaobo Zhou, Tom Kirchhausen, and Stephen TC Wong. Detection of molecular particles in live cells via machine learning. *Cytometry Part A*, 71(8):563–575, 2007.

[61] Yoav Freund and Robert Schapire. Experiments with a new boosting algorithm. In *ICML*, volume 96, pages 148–156, 1996.

154

[62] Paul Viola and Michael Jones. Rapid object detection using a boosted cascade of simple features. In *Computer Vision and Pattern Recognition, 2001. CVPR 2001. Proceedings of the 2001 IEEE Computer Society Conference on*, volume 1, pages I–511. IEEE, 2001.

[63] Ihor Smal, Marco Loog, Wiro Niessen, and Erik Meijering. Quantitative comparison of spot detection methods in fluorescence microscopy. *Medical Imaging, IEEE Transactions on*, 29(2):282–301, 2010.

[64] Nasir Rajpoot, Zhen Yao, and Roland Wilson. Adaptive wavelet restoration of noisy video sequences. In *Image Processing, 2004. ICIP'04. 2004 International Conference on*, volume 2, pages 957–960. IEEE, 2004.

[65] Luc Vincent. Morphological grayscale reconstruction in image analysis: applications and efficient algorithms. *Image Processing, IEEE Transactions on*, 2(2):176–201, 1993.

[66] Dorin Comaniciu and Peter Meer. Mean shift: A robust approach toward feature space analysis. *Pattern Analysis and Machine Intelligence, IEEE Transactions on*, 24(5):603–619, 2002.

[67] Herve Isambert, Pascal Venier, Anthony C Maggs, Abdelatif Fattoum, Ridha Kassab, Dominique Pantaloni, and Marie-France Carlier. Flexibility of actin filaments derived from thermal fluctuations. effect of bound nucleotide, phalloidin, and muscle regulatory proteins. *Journal of Biological Chemistry*, 270 (19):11437–11444, 1995.

[68] John C Beatty and Brian A Barsky. *An introduction to splines for use in computer graphics and geometric modeling*. Morgan Kaufmann, 1995.

[69] Thiagalingam Kirubarajan, Yaakov Bar-Shalom, and Krishna R Pattipati. Multiassignment for tracking a large number of overlapping objects [and ap-

plication to fibroblast cells]. *Aerospace and Electronic Systems, IEEE Transactions on*, 37(1):2–21, 2001.

[70] James A Roecker. A class of near optimal jpda algorithms. *Aerospace and Electronic Systems, IEEE Transactions on*, 30(2):504–510, 1994.

[71] Bing Chen and Jitendra K Tugnait. Tracking of multiple maneuvering targets in clutter using imm/jpda filtering and fixed-lag smoothing. *Automatica*, 37 (2):239–249, 2001.

[72] Xiaodong Yang, Houqiang Li, and Xiaobo Zhou. Nuclei segmentation using marker-controlled watershed, tracking using mean-shift, and kalman filter in time-lapse microscopy. *Circuits and Systems I: Regular Papers, IEEE Transactions on*, 53(11):2405–2414, 2006.

[73] William J Godinez, Marko Lampe, Stefan Wörz, Barbara Müller, Roland Eils, and Karl Rohr. Deterministic and probabilistic approaches for tracking virus particles in time-lapse fluorescence microscopy image sequences. *Medical Image Analysis*, 13(2):325–342, 2009.

[74] Auguste Genovesio, Bo Zhang, and Jean-Chrisophe Olivo-Marin. Interacting multiple model based method to track moving fluorescent biological spots. In *Biomedical Imaging: Nano to Macro, 2004. IEEE International Symposium on*, pages 1239–1242. IEEE, 2004.

[75] Linqing Feng, Yingke Xu, Yi Yang, and Xiaoxiang Zheng. Multiple dense particle tracking in fluorescence microscopy images based on multidimensional assignment. *Journal of Structural Biology*, 173(2):219–228, 2011.

[76] Seyed Hamid Rezatofighi, Stephen Gould, Richard Hartley, Katarina Mele, and William E Hughes. Application of the imm-jpda filter to multiple target tracking in total internal reflection fluorescence microscopy images. In *Medical*

Image Computing and Computer-Assisted Intervention–MICCAI 2012, pages 357–364. Springer, 2012.

[77] Yaakov Bar-Shalom, X Rong Li, and Thiagalingam Kirubarajan. *Estimation with applications to tracking and navigation: theory algorithms and software.* John Wiley & Sons, 2004.

[78] Tracy Camp, Jeff Boleng, and Vanessa Davies. A survey of mobility models for ad hoc network research. *Wireless Communications and Mobile Computing*, 2 (5):483–502, 2002.

[79] Vesselin P Jilkov and Xiaorong Li. Online bayesian estimation of transition probabilities for markovian jump systems. *Signal Processing, IEEE Transactions on*, 52(6):1620–1630, 2004.

[80] Kang Li, Eric D Miller, Mei Chen, Takeo Kanade, Lee E Weiss, and Phil G Campbell. Cell population tracking and lineage construction with spatiotemporal context. *Medical Image Analysis*, 12(5):546–566, 2008.

[81] Ivo F Sbalzarini and Petros Koumoutsakos. Feature point tracking and trajectory analysis for video imaging in cell biology. *Journal of Structural Biology*, 151(2):182–195, 2005.

[82] Salman S Rogers, Thomas A Waigh, Xiubo Zhao, and Jian R Lu. Precise particle tracking against a complicated background: polynomial fitting with gaussian weight. *Physical Biology*, 4(3):220, 2007.

[83] Nadine Tarantino, Jean-Yves Tinevez, Elizabeth Faris Crowell, Bertrand Boisson, Ricardo Henriques, Musa Mhlanga, Fabrice Agou, Alain Israël, and Emmanuel Laplantine. Tnf and il-1 exhibit distinct ubiquitin requirements for inducing nemo–ikk supramolecular structures. *The Journal of cell biology*, 204 (2):231–245, 2014.

157

[84] 3DHISTECH Ltd. Pannoramic viewer, 2016. URL `http://www.3dhistech.com/pannoramic_viewer`.

[85] Guanglei Xiong, Xiaobo Zhou, and Liang Ji. Automated segmentation of drosophila rnai fluorescence cellular images using deformable models. *Circuits and Systems I: Regular Papers, IEEE Transactions on*, 53(11):2415–2424, 2006.

[86] Adel Hafiane, Filiz Bunyak, and Kannappan Palaniappan. Clustering initiated multiphase active contours and robust separation of nuclei groups for tissue segmentation. In *Pattern Recognition, 2008. ICPR 2008. 19th International Conference on*, pages 1–4. IEEE, 2008.

[87] Adel Hafiane, Filiz Bunyak, and Kannappan Palaniappan. Fuzzy clustering and active contours for histopathology image segmentation and nuclei detection. In *Advanced Concepts for Intelligent Vision Systems*, pages 903–914. Springer, 2008.

[88] Norberto Malpica, Carlos Ortiz de Solorzano, Juan José Vaquero, Andrés Santos, Isabel Vallcorba, José Miguel Garcia-Sagredo, and Francisco del Pozo. Applying watershed algorithms to the segmentation of clustered nuclei. 1997.

[89] J MISWAN Sharif, MF Miswan, MA Ngadi, Md Sah Hj Salam, and Muhammad Mahadi Bin Abdul Jamil. Red blood cell segmentation using masking and watershed algorithm: A preliminary study. In *Biomedical Engineering (ICoBE), 2012 International Conference on*, pages 258–262. IEEE, 2012.

[90] Kan Jiang, Qing Min Liao, and Sheng Yang Dai. A novel white blood cell segmentation scheme using scale-space filtering and watershed clustering. In *Machine Learning and Cybernetics, 2003 International Conference on*, volume 5, pages 2820–2825. IEEE, 2003.

[91] Leyza Baldo Dorini, Rodrigo Minetto, and Neucimar Jeronimo Leite. White blood cell segmentation using morphological operators and scale-space analysis. In *Computer Graphics and Image Processing, 2007. SIBGRAPI 2007. XX Brazilian Symposium on*, pages 294–304. IEEE, 2007.

[92] Dwi Anoraganingrum. Cell segmentation with median filter and mathematical morphology operation. In *Image Analysis and Processing, 1999. Proceedings. International Conference on*, pages 1043–1046. IEEE, 1999.

[93] Cecilia Di Ruberto, Andrew Dempster, Shahid Khan, and Bill Jarra. Analysis of infected blood cell images using morphological operators. *Image and vision computing*, 20(2):133–146, 2002.

[94] Frederic Leymarie and Martin D Levine. Tracking deformable objects in the plane using an active contour model. *Pattern Analysis and Machine Intelligence, IEEE Transactions on*, 15(6):617–634, 1993.

[95] Pascal Bamford and Brian Lovell. Unsupervised cell nucleus segmentation with active contours. *Signal Processing*, 71(2):203–213, 1998.

[96] Min Hu, Xijian Ping, and Yihong Ding. A new active contour model and its application on cell segmentation. In *Control, Automation, Robotics and Vision Conference, 2004. ICARCV 2004 8th*, volume 2, pages 1104–1107. IEEE, 2004.

[97] Kashif Rajpoot and Nasir Rajpoot. Svm optimization for hyperspectral colon tissue cell classification. In *Medical Image Computing and Computer-Assisted Intervention–MICCAI 2004*, pages 829–837. Springer, 2004.

[98] Johan AK Suykens and Joos Vandewalle. Least squares support vector machine classifiers. *Neural processing letters*, 9(3):293–300, 1999.

[99] Andy Liaw and Matthew Wiener. Classification and regression by randomforest. *R News*, 2(3):18–22, 2002.

[100] Tao Shi, David Seligson, Arie S Belldegrun, Aarno Palotie, and Steve Horvath. Tumor classification by tissue microarray profiling: random forest clustering applied to renal cell carcinoma. *Modern Pathology*, 18(4):547–557, 2005.

[101] Arnout C Ruifrok and Dennis A Johnston. Quantification of histochemical staining by color deconvolution. *Analytical and Quantitative Cytology and Histology/the International Academy of Cytology [and] American Society of Cytology*, 23(4):291–299, 2001.

[102] Manohar Kuse, Yi-Fang Wang, Vinay Kalasannavar, Michael Khan, and Nasir Rajpoot. Local isotropic phase symmetry measure for detection of beta cells and lymphocytes. *Journal of pathology informatics*, 2, 2011.

[103] Pete Kovesi. Symmetry and asymmetry from local phase. In *Tenth Australian Joint Conference on Artificial Intelligence*, volume 190. Citeseer, 1997.

[104] Gareth Loy and Alexander Zelinsky. Fast radial symmetry for detecting points of interest. *Pattern Analysis and Machine Intelligence, IEEE Transactions on*, 25(8):959–973, 2003.

[105] Zhitao Xiao, Zhengxin Hou, Changyun Miao, and Jianming Wang. Using phase information for symmetry detection. *Pattern Recognition Letters*, 26 (13):1985–1994, 2005.

[106] Alan V Oppenheim, Ronald W Schafer, and John R Buck. *Discrete-time signal processing*, volume 2. Prentice-hall Englewood Cliffs, 1989.

[107] Pietro Perona and Jitendra Malik. Scale-space and edge detection using anisotropic diffusion. *Pattern Analysis and Machine Intelligence, IEEE Transactions on*, 12(7):629–639, 1990.

[108] S Marčelja. Mathematical description of the responses of simple cortical cells*. *JOSA*, 70(11):1297–1300, 1980.

[109] John G Daugman. Uncertainty relation for resolution in space, spatial frequency, and orientation optimized by two-dimensional visual cortical filters. *JOSA A*, 2(7):1160–1169, 1985.

[110] David J Field. Relations between the statistics of natural images and the response properties of cortical cells. *JOSA A*, 4(12):2379–2394, 1987.

[111] Pierre Soille. *Morphological image analysis: principles and applications.* Springer Science & Business Media, 2013.

[112] Difference of gaussians edge enhancement. `http://micro.magnet.fsu.edu/primer/java/digitalimaging/processing/diffgaussians/index.html`. Accessed: 2014-09-30.

[113] Mitra Basu. Gaussian-based edge-detection methods-a survey. *IEEE Transactions on Systems, Man, and Cybernetics, Part C*, 32(3):252–260, 2002.

[114] David Marr and Ellen Hildreth. Theory of edge detection. *Proceedings of the Royal Society of London B: Biological Sciences*, 207(1167):187–217, 1980.

[115] Nobuyuki Otsu. A threshold selection method from gray-level histograms. *Automatica*, 11(285-296):23–27, 1975.

[116] John A Hartigan and Manchek A Wong. Algorithm as 136: A k-means clustering algorithm. *Applied Statistics*, pages 100–108, 1979.

[117] Petros Maragos. Tutorial on advances in morphological image processing and analysis. *Optical Engineering*, 26(7):267623–267623, 1987.

[118] Edward R Dougherty and Roberto A Lotufo. *Hands-on morphological image processing*, volume 71. SPIE Press, 2003.

[119] Martin Ester, Hans-Peter Kriegel, Jörg Sander, and Xiaowei Xu. A density-based algorithm for discovering clusters in large spatial databases with noise. In *KDD*, volume 96, pages 226–231, 1996.

[120] Herbert Edelsbrunner, David G Kirkpatrick, and Raimund Seidel. On the shape of a set of points in the plane. *Information Theory, IEEE Transactions on*, 29(4):551–559, 1983.

[121] James Geoffrey Hayes and J Halliday. The least-squares fitting of cubic spline surfaces to general data sets. *IMA Journal of Applied Mathematics*, 14(1): 89–103, 1974.

[122] Vis visiopharm. `http://web.archive.org/web/20080207010024/http://www.808multimedia.com/winnt/kernel.htm`. Accessed: 2014-09-30.

[123] Shivang Naik, Scott Doyle, Shannon Agner, Anant Madabhushi, Michael Feldman, and John Tomaszewski. Automated gland and nuclei segmentation for grading of prostate and breast cancer histopathology. In *Biomedical Imaging: From Nano to Macro, 2008. ISBI 2008. 5th IEEE International Symposium on*, pages 284–287. IEEE, 2008.

[124] Kien Nguyen, Anindya Sarkar, and Anil K Jain. Structure and context in prostatic gland segmentation and classification. In *Medical Image Computing and Computer-Assisted Intervention–MICCAI 2012*, pages 115–123. Springer, 2012.

[125] James Diamond, Neil H. Anderson, Peter H. Bartels, Rodolfo Montironi, and Peter W. Hamilton. The use of morphological characteristics and texture analysis in the identification of tissue composition in prostatic neoplasia. *Allgemeines Statistisches Archiv*, 89(1):7–20, 2005.

[126] Reza Farjam, Hamid Soltanian-Zadeh, Kourosh Jafari-Khouzani, and Reza A Zoroofi. An image analysis approach for automatic malignancy determination of prostate pathological images. *Cytometry Part B: Clinical Cytometry*, 72 (4):227–240, 2007.

[127] H. S. Wu, Rharpaz N Xu, D Burstein, and J Gil. Segmentation of intestinal gland images with iterative region growing. *Journal of Microscopy*, 220(3): 190204, 2005.

[128] Jun Xu, Rachel Sparks, Andrew Janowczyk, John E. Tomaszewski, Michael D. Feldman, and Anant Madabhushi. High-throughput prostate cancer gland detection, segmentation, and classification from digitized needle core biopsies. In *Prostate Cancer Imaging. Computer-Aided Diagnosis, Prognosis, and Intervention - International Workshop, Held in Conjunction with MICCAI 2010, Beijing, China, September 24, 2010. Proceedings*, pages 77–88, 2010.

[129] Shivang Naik, Scott Doyle, Michael Feldman, John Tomaszewski, and Anant Madabhushi. Gland segmentation and computerized gleason grading of prostate histology by integrating low-, high-level and domain specific information. *Miaab Workshop*, 2007.

[130] C H Chen. Handbook of pattern recognition and computer vision. *World Scientific*, 50(2):996, 1993.

[131] Cigdem Gunduz-Demir, Melih Kandemir, Akif Burak Tosun, and Cenk Sokmensuer. Automatic segmentation of colon glands using object-graphs. *Medical Image Analysis*, 14(1):1–12, 2010.

[132] Korsuk Sirinukunwattana, David Snead, and Nasir Rajpoot. A stochastic polygons model for glandular structures in colon histology images. *Medical Imaging, IEEE Transactions on*, 2015.

[133] Hao Fu, Guoping Qiu, Mohammad Ilyas, and Jie Shu. Glandvision: A novel polar space random field model for glandular biological structure detection. In *Proceedings of the British Machine Vision Conference*, pages 42.1–42.12. BMVA Press, 2012.

[134] George Lee, Sahirzeeshan Ali, Robert Veltri, Jonathan I Epstein, Christhunesa Christudass, and Anant Madabhushi. Cell orientation entropy (core): Predicting biochemical recurrence from prostate cancer tissue microarrays. In *Medical Image Computing and Computer-Assisted Intervention–MICCAI 2013*, pages 396–403. Springer, 2013.

[135] Adnan Mujahid Khan, Nasir Rajpoot, Darren Treanor, and Derek Magee. A non-linear mapping approach to stain normalisation in digital histopathology images using image-specific colour deconvolution. *IEEE Transactions on Biomedical Engineering*, 2014.

[136] Radhakrishna Achanta, Appu Shaji, Kevin Smith, Aurelien Lucchi, Pascal Fua, and Sabine Susstrunk. Slic superpixels compared to state-of-the-art superpixel methods. *Pattern Analysis and Machine Intelligence, IEEE Transactions on*, 34(11):2274–2282, 2012.

[137] Jonathan I Epstein. An update of the gleason grading system. *The Journal of urology*, 183(2):433–440, 2010.

[138] Steve Lawrence, C Lee Giles, Ah Chung Tsoi, and Andrew D Back. Face recognition: A convolutional neural-network approach. *Neural Networks, IEEE Transactions on*, 8(1):98–113, 1997.

[139] Patrice Y Simard, Dave Steinkraus, and John C Platt. Best practices for convolutional neural networks applied to visual document analysis. In *International Conference on Document Analysis & Recognition*, page 958. IEEE, 2003.

[140] Dan C Cireşan, Alessandro Giusti, Luca M Gambardella, and Jürgen Schmidhuber. Mitosis detection in breast cancer histology images with deep neural networks. In *Medical Image Computing and Computer-Assisted Intervention–MICCAI 2013*, pages 411–418. Springer, 2013.

[141] Y.-W. Tsang D. Snead I. Cree N.M. Rajpoot K. Sirinukunwattana, S.E.A. Raza. A novel deep learning framework for detection and classification of nuclei in colorectal cancer histology images. *IEEE Transactions on Medical Imaging*, 2015.

[142] Korsuk Sirinukunwattana, Shan E Ahmed Raza, Yee-Wah Tsang, David Snead, Ian Cree, and Nasir Rajpoot. A spatially constrained deep learning framework for detection of epithelial tumor nuclei in cancer histology images. In *Patch-Based Techniques in Medical Imaging*, pages 154–162. Springer, 2015.

[143] Masakazu Matsugu, Katsuhiko Mori, Yusuke Mitari, and Yuji Kaneda. Subject independent facial expression recognition with robust face detection using a convolutional neural network. *Neural Networks*, 16(5):555–559, 2003.

[144] Convolutional neural networks (lenet) - deeplearning 0.1 documentation. `http://http://deeplearning.net/tutorial/lenet.html`. Accessed: 2015-10-10.